Measurement of the $\beta - \nu$ Correlation in Laser Trapped ^{21}Na

by

Nicholas David Scielzo

B.A. (Harvard University) 1997
M.S. (University of California, Berkeley) 1999

A dissertation submitted in partial satisfaction of the
requirements for the degree of
Doctor of Philosophy

in

Physics

in the

GRADUATE DIVISION
of the
UNIVERSITY OF CALIFORNIA, BERKELEY

Committee in charge:
Professor Stuart J. Freedman, Chair
Professor Eugene D. Commins
Professor Heino Nitsche

Spring 2003

The dissertation of Nicholas David Scielzo is approved:

Chair Date

Date

Date

University of California, Berkeley

Spring 2003

Measurement of the $\beta - \nu$ Correlation in Laser Trapped ^{21}Na

Nicholas David Scielzo

Abstract

Measurement of the $\beta - \nu$ Correlation in Laser Trapped ^{21}Na

by

Nicholas David Scielzo

Doctor of Philosophy in Physics

University of California, Berkeley

Professor Stuart J. Freedman, Chair

Trapped radioactive atoms are an appealing source for precise measurements of the $\beta - \nu$ correlation coefficient, $a_{\beta\nu}$, since the momentum of the neutrino can be inferred from the detection of the unperturbed low-energy recoil daughter nucleus. ^{21}Na is produced on-line at the 88-Inch Cyclotron at Lawrence Berkeley National Laboratory and 800,000 atoms have been maintained in a magneto-optical trap. A static electric field draws daughter ^{21}Ne ions to a microchannel plate detector and β^+s are detected in coincidence with a plastic scintillator β-detector. The ^{21}Ne time-of-flight distribution determines $a_{\beta\nu}$. The resulting charge-state distribution is compared to a simple model based on the sudden approximation which suggests a small but important contribution from nuclear recoil-induced ionization. A larger than expected fraction of the daughters are detected in positive charge-states, but no dependence on either the β^+ or recoil nucleus energy was observed. We find $a_{\beta\nu} = 0.5243 \pm 0.0092$, which is in $3.6\,\sigma$ disagreement with the Standard Model prediction of $a_{\beta\nu} = 0.558 \pm 0.003$. Aside from a deviation from the Standard Model, a possible explanation for the discrepency is that the branching ratio to the first excited-state is in error.

Professor Stuart J. Freedman
Dissertation Committee Chair

To my parents, Charles and Caroline, and my wife, Laura, for their love and support.

Contents

List of Figures

List of Tables

Acknowledgments

I have been fortunate to work with a wonderful group of people while at UC Berkeley. I thank Stuart Freedman for his guidance and support. Oh, and helping to remove some of the "Harvard" from my writing. It has been a pleasure working day-to-day with Dr. Paul Vetter. His friendship, patience, and ability to think clearly at 4 am made cyclotron runs enjoyable (even the ones where everything seemed to need fixing). And to Dr. Brian Fujikawa, it is "Dr. Poor Man's John Travolta" to you now! I thank Jason Burke for his help with the ion source during the MCP calibration and Wes Winter for accepting my messy office habits. I would also like to thank Prof. Eugene Commins and Prof. Heino Nitsche for taking the time to get to know me and my research. Thanks to my fellow physics grad students, Ben Lintner, Andreas Birkedal, Josephine Chen, and Daniel Whiteson, and even a couple of you chem grad students (Nir Goldman and Eric Tulsky) for putting up with this Jersey boy.

I thank my parents for their encouragement and involvement in my education through all these years (even when I went all the way to California). And of course, I couldn't have made it through without the support and love of my wife, Laura.

Chapter 1

Introduction

Over the past century, β decay studies have unearthed many surprises. Unique properties of the weak interaction have repeatedly lead to a revision of our view of nature. Since the discovery of radioactivity in uranium by Becquerel in 1896, researchers have found nuclei emit alpha particles and γ-rays at energies corresponding to the energy difference, E_0, between the initial and final nuclear states. However, β particles were detected with a continuum of energies from zero to E_0, in apparent violation of energy and momentum conservation. Calorimetric tests confirmed that the average energy release was consistent with the observed β spectra, dispelling the notion that energy loss prior to detection accounts for the spread. Conservation of angular momentum also seemed violated in β decays. The electron, due to its half-integer spin, cannot carry away the integer change in angular momentum observed in decays. Of course we know today that in β-decay, a nearly massless, neutral, spin $\frac{1}{2}$ particle is emitted with the β and escapes detection due to its feeble interactions with matter. The particle was postulated by W. Pauli, given the name "neutrino" by E. Fermi, and directly detected by Cowan and Reines in 1956 [1]. This was the first surprise, but the history of β decay shows more follow in years to come.

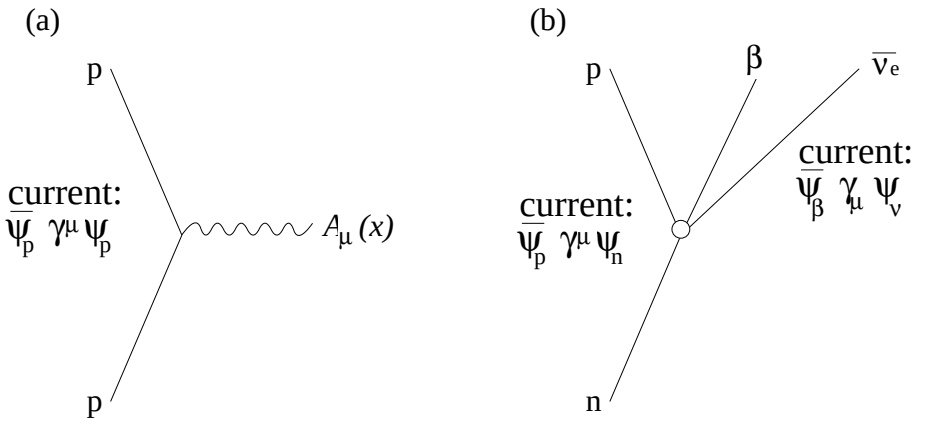

Figure 1.1: Feynman diagram for (a) proton, p, interacting with an electromagnetic field $A^\mu(x)$ and (b) Fermi's analogy for neutron β decay, including a four-fermion vertex.

1.1 Universal Fermi Interaction

Fermi described nuclear β decay in analogy to electromagnetism — through a vector-vector, local, four-fermion interaction (see Figure 1.1) with electric charge replaced by the Fermi coupling constant, $\frac{G_F}{\sqrt{2}}$. As this interaction describes many weak interaction processes with the same coupling constant, it is referred to as the "universal Fermi interaction". However, it was not understood why the strong interaction did not renormalize the interaction, causing different couplings in nuclear β decay and μ decay. It was postulated that $\bar{\psi}_B \gamma^\mu \psi_A$ and its conjugate $\bar{\psi}_A \gamma^\mu \psi_B$, together with $\bar{\psi}_A \gamma^\mu \psi_A$ from electromagnetism form an isospin triplet. Just as electric charge remains constant, so does the vector component of the weak interaction. This hypothesis is known as the conserved vector current (CVC) hypothesis. Even though this aesthetically pleasing picture was found to be incomplete, the intuition that electromagnetism and the weak interaction are closely related proved correct.

1.2 Parity Violation and the $V - A$ Interaction

An interaction is symmetric under parity (P) if it is unchanged by the coordinate transformation P:

$$\vec{x} \to -\vec{x} \qquad \text{and} \qquad t \to t. \tag{1.1}$$

P reverses linear momenta, but angular momenta and energies are unchanged. Parity had been assumed to be a perfect symmetry for all forces. Atomic and nuclear spectroscopy had shown parity mixing between states was $\lesssim 10^{-2}\%$ for the strong interaction and $\lesssim 10^{-4}\%$ for the electromagnetic interaction. Indications that parity may be violated arose when mesons named τ and θ with the same mass, lifetime, and spin, decayed to states of opposite parity. Either the only difference between these particles was their intrinsic parity or the weak interaction violated parity.

Lee and Yang did a survey of particle interactions and concluded parity had never been tested in the weak interaction [2]. Shortly thereafter, experiments conclusively demonstrated parity-violation in both nuclear β decay and weak decays of other particles. The most famous was C. S. Wu's ^{60}Co β-asymmetry measurement. Paramagnetic ^{60}Co was cooled to 10 mK to align nuclear spins. A parity-violating correlation between the nuclear spin, $\vec{J}$, and β momentum, $\vec{p}_\beta$, known as the β-asymmetry (see Figure 1.2), was discovered. The results implied maximal parity violation in nuclear β decay [3], and similar conclusions were reached in the decays $\pi^\pm \to \mu^\pm \to e^\pm$ [4, 5].

In addition, the most general interaction Hamiltonian contains five relativistically invariant interactions: vector (V), axial-vector (A), scalar (S), tensor (T), and pseudoscalar (P). The dominant interaction terms were originally determined from the correlation between $\vec{p}_\beta$ and the neutrino momentum, known as the $\beta - \nu$ correlation. The neutrino is extremely difficult to detect, so the correlation is inferred from the nuclear recoil imparted by the outgoing leptons. Typical nuclear recoils are $\sim$100 eV, making it is extremely challenging to measure the correlation with precision. After more than a decade of $\beta - \nu$ correlation measurements (summarized in the Appendix) and several contradictory results, the Lorentz

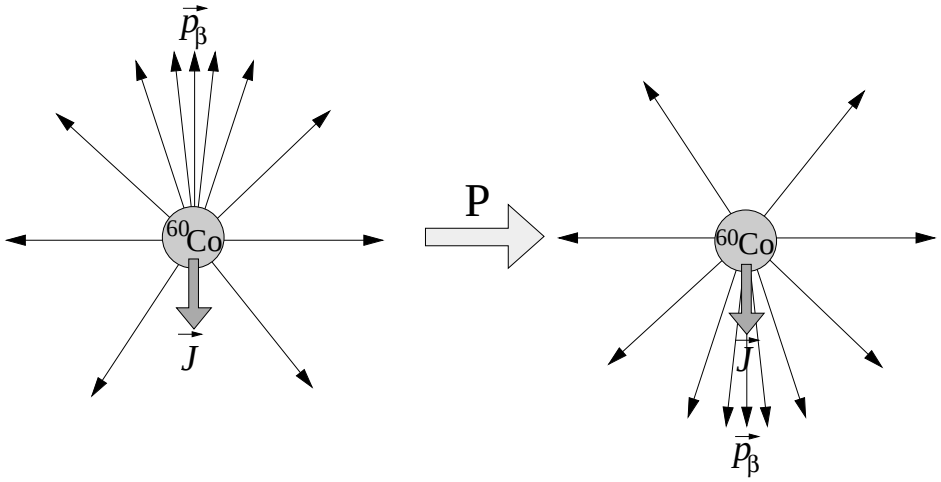

Figure 1.2: The correlation between $\vec{J}$, and $\vec{p}_\beta$ changes sign under P.

structure was found to be primarily V and A. Polarized neutron decay indicated that the interactions V and A are of opposite sign [6]. The $V - A$ structure is supported by the helicity suppression of the π^+ decay branch: $\pi^+ \to \beta^+ + \nu_e$ [7, 8].

1.3 CP Violation

Since the weak interaction seemed to only involve left-handed leptons and right-handed anti-leptons (in the limit of massless leptons), the weak interaction violated not only parity, but also charge conjugation symmetry (C). Charge conjugation exchanges particle and antiparticle, changing the sign of all additive quantum numbers such as charge and lepton/baryon number. An additional discrete symmetry, time-reversal (T), reverses only the time coordinate. While C and P are individually broken in the weak interaction, the combination CP was thought to be preserved. If we assume the validity of the CPT theorem, which proves local, Lorentz-invariant, field theories are invariant under combined operation of C, P, and T, then CP violation implies T violation.

Against expectations, CP violation was discovered in neutral kaon decays. The strangeness eigenstates K^0 and $\bar{K}^0$ created by the strong interaction decay through the weak

interaction to two CP eigenstates, 2π (CP$(2\pi) = 2\pi$) and 3π (CP$(3\pi) = -3\pi$). Choosing the phase as CP$(\bar{K}^0) = K^0$, it was expected that $K_1 = \frac{1}{\sqrt{2}}(K^0 + \bar{K}^0)$ (CP$(K_1) = K_1$) and $K_2 = \frac{1}{\sqrt{2}}(K^0 - \bar{K}^0)$ (CP$(K_2) = -K_2$) would be the eigenstates of the weak interaction. The short-lived, CP even, neutral kaon state would decay exclusively to two pions and a longer-lived, CP odd, neutral kaon would decay exclusively to three pions. However, the longer-lived state decayed to $\pi^+\pi^-$ with a branching ratio of 2×10^{-3} [9], implying CP violation. Recently, CP violation has also been observed in the $B^0 - \bar{B}^0$ system by the BaBar [10] and Belle [11] collaborations.

1.4 The Standard Model

The framework of what we now call the Standard Model began in the 1960's with the unification of the weak and electromagnetic gauge theories by Glashow, Weinberg, and Salam. They predicted the gauge transformations are

$$SU(2)_L \otimes U(1) \tag{1.2}$$

and both the $SU(2)_L$ and $U(1)$ symmetries are spontaneously broken. Electromagnetism retains an unbroken $U(1)_{EM}$ symmetry as a subgroup of $SU(2)_L \otimes U(1)$. The $W^\pm$ and Z^0 bosons that mediate the weak interaction acquire masses $M_W \approx 80\,\text{GeV}$ and $M_Z \approx 90\,\text{GeV}$, through the symmetry breaking by the scalar Higgs field. At energies much smaller than M_W, the interaction can be considered point-like because the range is limited to $\sim 10^{-3}$ fm.

Three generations of fermions have been discovered and can be grouped as follows: left-handed fermions form $SU(2)$ quark doublets:

$$Q_L^i = \left\{ \begin{pmatrix} u^i \\ d^i \end{pmatrix}_L \right\} = \left\{ \begin{pmatrix} u \\ d \end{pmatrix}_L, \begin{pmatrix} c \\ s \end{pmatrix}_L, \begin{pmatrix} t \\ b \end{pmatrix}_L \right\} \tag{1.3}$$

and lepton doublets:

$$L_L^i = \left\{ \begin{pmatrix} \nu_e \\ e \end{pmatrix}_L, \begin{pmatrix} \nu_\mu \\ \mu \end{pmatrix}_L, \begin{pmatrix} \nu_\tau \\ \tau \end{pmatrix}_L \right\}. \tag{1.4}$$

where i =1,2,3 is the generation index. Right-handed fermions form $SU(2)$ singlets:

$$u_R^i = \left\{ u_R, c_R, t_R \right\} \tag{1.5}$$

$$d_R^i = \left\{ d_R, s_R, b_R \right\} \tag{1.6}$$

$$n_R^i = \left\{ \nu_{eR}, \nu_{\mu R}, \nu_{\tau R} \right\} \tag{1.7}$$

$$l_R^i = \left\{ e_R, \mu_R, \tau_R \right\}. \tag{1.8}$$

The $W^{\pm}$ bosons couple only to the left-handed fermions, leading to the observed maximal parity violation. The anomalies in this theory cancel when contributions from all fermions are summed.

Unlike the strong or electromagnetic interactions, the charged weak interaction, J^{μ}, mixes the quark generations as follows:

$$J^{\mu} \propto \bar{u}_L^i \gamma^{\mu} V_{CKM}^{ij} d_L^j \tag{1.9}$$

where V_{CKM} is the Cabibo-Kobayashi-Maskawa (CKM) mixing matrix:

$$V_{CKM} = \begin{pmatrix} V_{ud} & V_{us} & V_{ub} \\ V_{cd} & V_{cs} & V_{cb} \\ V_{td} & V_{ts} & V_{tb} \end{pmatrix}.$$

The most general complex 3×3 matrix has 18 parameters. Assuming unitarity of V_{CKM} and choosing quark field phases reduces the number of parameters to three rotations and one complex phase. The complex phase is thought to explain the CP violation observed in K and B decays. For a unitary matrix, the sum of the squares of each column and row equals one. The first row provides the most precise test of unitarity because the largest matrix element, V_{ud}, has been precisely measured in nuclear β decay. The result

$$|V_{ud}|^2 + |V_{us}|^2 + |V_{ub}|^2 = 0.9968 \pm 0.0014 \tag{1.10}$$

differs from unitarity by $2.2\,\sigma$ [12] and much research has been done to understand this discrepency.

1.5 Future of Nuclear β Decay Studies

Although the $V-A$ (vector minus axial-vector) interaction has been extremely successful and can account for all observed interactions except for CP violation, limits on interactions beyond those included in the Standard Model can exist and even be quite large. Today, nuclear β decay is being studied to search for intrinsic (as opposed to induced) scalar (S), tensor (T), or pseudoscalar (P) contributions to the dominant $V-A$ Lorentz structure, right-handed ($V+A$) currents, and even small ($\lesssim 10^{-3}$) admixtures of massive (>MeV) neutrinos emitted in β decay. Precision tests of time-reversal-invariance and the conserved vector current hypothesis can be greatly improved.

Measurements of recoil-ion spectra (with or without coincident detection of the emitted β) from nuclear β decay are useful probes of the weak interaction and are used to address these goals. The energy spectra of ^{6}He [13, 14, 15], ^{23}Ne [13, 16], ^{19}Ne [17, 13], and ^{35}Ar [13] decays led to the discovery of the $V-A$ structure and the ^{6}He $\beta-\nu$ correlation [15] provides the best limit to a possible tensor component. The recoil spectra from the electron capture (EC) decay of ^{37}Ar [18] and β^{+} decay of ^{38m}K [19] have recently put limits on the admixture of heavy neutrinos.

Trapped radioactive atoms are appealing for the next generation of β decay experiments to test the Standard Model. Radioactive nuclei are confined to a $\approx$1 mm^3 volume, decay essentially at rest (velocities $\lesssim$1 m/s), and the recoil daughters emerge with minimal perturbation. Daughter ions can be manipulated with electric and magnetic fields. Several β decay correlation measurements are currently underway [20, 21] or nearing an interesting precision of 0.01 [22], and further improvements are expected.

Chapter 2

Nuclear β Decay

At energies of order MeV, we describe nuclear β decay in terms of a four-Fermion contact interaction. The discussion is restricted to allowed decays where effects from the strong and electromagnetic interactions can be included with a precision exceeding the 10^{-3} level. We calculate the β decay phase space for a nucleus of charge Z, mass M, and spin $\vec{J}$. Correlations between the β momentum, $\vec{p}_\beta$, the neutrino momentum, $\vec{p}_\nu$, and $\vec{J}$, are sensitive to the Lorentz structure. Measurements of these correlation coefficients are compared to Standard Model predictions and used to put limits on physics beyond the Standard Model. The correlation between $\vec{p}_\beta$ and $\vec{p}_\nu$, known as the $\beta - \nu$ correlation is discussed in detail.

2.1 General Effective Weak Decay Hamiltonian

In the nuclear β decay, $A \to B + \beta + \nu_e$, the four-momentum $|q|$ exchanged is always much less than the mass M_W of the $W^\pm$ bosons that mediate the decay. This allows a simplification of the W propagator in the limit $M_W \to \infty$ (see Figure 2.1):

$$\frac{-i(g_{\mu\nu} - \frac{q_\mu q_\nu}{M_W^2})}{q^2 - M_W^2} \to \frac{i g_{\mu\nu}}{M_W^2} \tag{2.1}$$

and the interaction can be written as an effective four-fermion vertex as Fermi had envisioned it. Nuclear β decay can be described without knowledge of physics at $\sim$80 GeV,

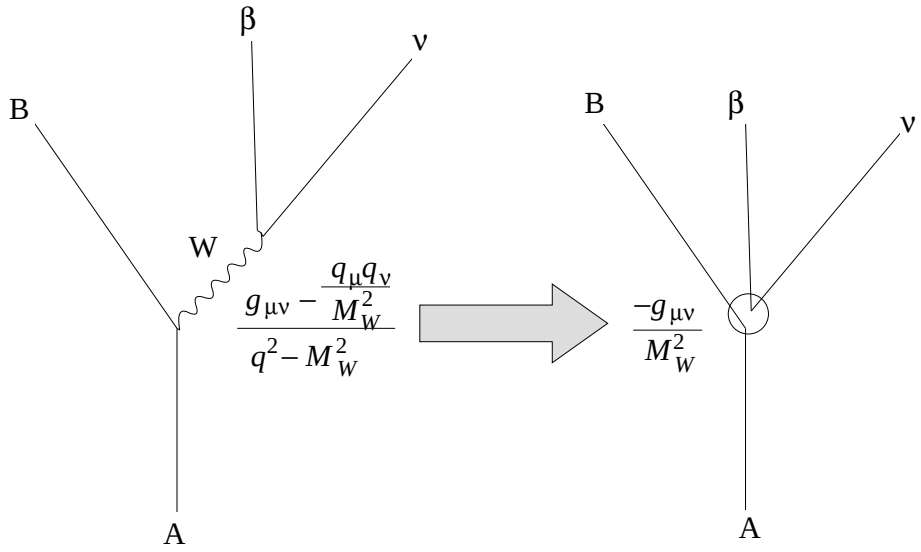

Figure 2.1: In the limit $M_W \to \infty$, the details of the W boson propagator become unimportant (except that the coupling constant is proportional to M_W^{-2}) and the interaction is expressed as a four-Fermion interaction.

using an interaction strength $\frac{G_\beta}{\sqrt{2}} \propto M_W^{-2}$. A number of books [23, 24, 25] cover the physics of nuclear β decay clearly and are applicable to research today, even though most were written before the discovery of the $W^\pm$ and Z^0 bosons or even the conception of the Standard Model.

In the limit of a four-Fermion contact interaction, the most general interaction Hamiltonian density that is invariant under proper Lorentz transformations, linear in the fields ψ_A, ψ_B, ψ_β, and ψ_ν, and without derivatives is [2]

$$\begin{aligned} H_{int} \quad \propto \quad & (\bar{\psi}_B \psi_A)(C_S \bar{\psi}_\beta \psi_\nu + C'_S \bar{\psi}_\beta \gamma_5 \psi_\nu) \\ & + (\bar{\psi}_B \gamma^\mu \psi_A)(C_V \bar{\psi}_\beta \gamma_\mu \psi_\nu + C'_V \bar{\psi}_\beta \gamma_\mu \gamma_5 \psi_\nu) \\ & + \frac{1}{2}(\bar{\psi}_B \sigma^{\mu\alpha} \psi_A)(C_T \bar{\psi}_\beta \sigma_{\mu\alpha} \psi_\nu + C'_T \bar{\psi}_\beta \sigma_{\mu\alpha} \gamma_5 \psi_\nu) \\ & - (\bar{\psi}_B \gamma^\mu \gamma^5 \psi_A)(C_A \bar{\psi}_\beta \gamma_\mu \gamma_5 \psi_\nu + C'_A \bar{\psi}_\beta \gamma_\mu \psi_\nu) \\ & + (\bar{\psi}_B \gamma_5 \psi_A)(C_P \bar{\psi}_\beta \gamma_5 \psi_\nu + C'_P \bar{\psi}_\beta \psi_\nu) + \text{h.c.} \end{aligned} \tag{2.2}$$

where C and C' represent the coupling constants for potential scalar (S), vector (V), ten-

sor (T), axial-vector (A), and pseudoscalar (P) interactions. The presence of the parity-violating, primed coefficients was motivated by the observation of parity-violation by C. S. Wu in 1957 [3]. Inclusion of the hermitian conjugate (h.c.) allows for both β^- and β^+ decays and makes the Hamiltonian hermitian. Each wavefunction has a spatial distribution localized at the nuclear position (taken as the coordinate system origin) and is expressed as $\psi_i(x^\mu) = \psi_i(\vec{x})e^{iE_i t}$ for $i = A$, B, β, and ν_e. With complex coupling constants there are 19 degrees of freedom (the overall phase is arbitrary). Time-reversal invariance reduces the number of constants to 10. Nuclear β decay is sensitive to 8 of these because at low momentum transfers, the pseudoscalar couplings do not appreciably contribute. However, this does not imply there is no pseudoscalar component in the weak interaction (or even that the coupling constant is small). Clearly, a large number of measurements are needed to constrain the structure of the interaction, and current bounds on the coupling constants are not very restrictive.

2.2 Induced Weak Currents

We first assume the $V-A$ structure of the Weak Interaction to calculate the Standard Model predictions to be tested by experiment. In nuclear β decay, essentially all predictions of the Standard Model have been experimentally verified within the experimental uncertainty. In the absence of the strong interaction, the Standard Model predicts

$$C_V = -C'_V = -C_A = C'_A \tag{2.3}$$

and all other coupling constants are zero. This gives

$$H_{int} \propto C_V(\bar{\psi}_B\gamma^\mu\psi_A - \bar{\psi}_B\gamma^\mu\gamma_5\psi_A)(\bar{\psi}_\beta\gamma_\mu\psi_\nu - \bar{\psi}_\beta\gamma_\mu\gamma_5\psi_\nu). \tag{2.4}$$

However, since A and B have structure, the intrinsic $V-A$ current becomes

$$\begin{aligned} \bar{\psi}_B\gamma^\mu\psi_A &\rightarrow \bar{\psi}_B\Big(f_1(q^2)\gamma^\mu + if_2(q^2)\sigma^{\mu\alpha}q_\alpha + f_3(q^2)q^\mu\Big)\psi_A \\ -\bar{\psi}_B\gamma^\mu\gamma_5\psi_A &\rightarrow \bar{\psi}_B\Big(g_1(q^2)\gamma^\mu\gamma^5 - ig_2(q^2)\sigma^{\mu\alpha}\gamma_5 q_\alpha + g_3(q^2)\gamma_5 q^\mu\Big)\psi_A \end{aligned} \tag{2.5}$$

where $f_i(q^2)$ and $g_i(q^2)$ are form factors. We evaluate these form factors at $q^2 = 0$, and drop the q^2 dependence to simplify notation. We view the nuclei as "elementary particles" that can be described by three properties: net spin, parity, and four-momentum. The nuclear structure dependence of the matrix elements is encapsulated in the form factors. The transition matrix element for each of the A_N nucleons in the nucleus is

$$\begin{aligned} M_{AB} &= \frac{G_\beta}{\sqrt{2}} \int \bar{\psi}_B(x) e^{iE_B t} \Big(f_1 \gamma^\mu j_\mu(x) + f_2 \sigma^{\mu\alpha} \partial_\alpha j_\mu(x) - i f_3 \partial^\mu j_\mu(x) \\ &\quad + g_1 \gamma^\mu \gamma^5 j_\mu(x) - g_2 \sigma^{\mu\alpha} \gamma^5 \partial_\alpha j_\mu(x) - i g_3 \gamma_5 \partial^\mu j_\mu(x) \Big) \psi_A e^{-iE_A t} d^4x \end{aligned} \tag{2.6}$$

where $j_\mu(x) = \bar{\psi}_\beta \gamma_\mu (1 - \gamma_5) \psi_\nu$ is the lepton current.

The form factors are constrained by several symmetries. The G-parity transformation, $G = Ce^{i\pi I_2}$, is the product of charge conjugation and a 180° rotation in isospin space. Since the strong interaction is invariant under these transformations, the induced terms are expected to have the same G-parity as their leading-order counterparts. The differing charge of the neutron and proton breaks G-parity to a small degree. Induced terms are referred to as first-class (second-class) if they have the same (opposite) G-parity of their leading-order counterparts. Second-class currents (SCC), such as $g_2(q^2)$ and $f_3(q^2)$, are essentially forbidden [26, 27, 28] because of this symmetry. Their absence has been validated by a variety of nuclear and particle physics experiments, many of which are summarized in Ref. [29]. The magnitude of SCCs is limited by differences in the ft values of mirror β^+ and β^- unstable nuclei, the energy dependence in the $\beta - \alpha$ correlation in ^{8}Li and ^{8}B decays, and the measured $\beta - \nu$ correlation in ^{6}He are at the level of $g_2 \lesssim f_2/5$ [30, 31, 29].

The conserved vector current (CVC) hypothesis states that the vector current of the interaction, together with the isovector current of electromagnetism form a triplet of conserved currents. This implies the vector component, f_1, remains unchanged by the presence of the strong interaction, and is equal in nuclear β decay and muon decay. We set $f_1 = 1$, so that the strength of the weak interaction is described by the Fermi coupling constant, $\frac{G_\beta}{\sqrt{2}} = 1.136 \times 10^{-5}\,\mathrm{GeV}^{-2}$. The coupling constant determined from μ decay, G_μ, is 2.6% larger than G_β because of the V_{ud} CKM quark mixing matrix element involved in

β decay. Measurements of the neutron lifetime [32] and β-asymmetry [33] have shown that $\frac{g_1(0)}{f_1(0)} = -\frac{C_A}{C_V} \cong 1.2739 \pm 0.0019$ [34]. The induced f_2 arises in an analogous manner to the magnetic moment and is referred to as the "weak magnetism" term. It is deduced from electromagnetic properties of the nuclei. Like G-parity symmetry, CVC implies $f_3(q^2) = 0$.

The leptons must be treated relativistically. The nucleons are non-relativistic and their wavefunctions reduce to

$$\psi_i = \begin{pmatrix} \chi_i \\ \frac{\vec{\sigma}\cdot\vec{p}_i}{2}\chi_i \end{pmatrix} \tag{2.7}$$

where χ_i are the two-component spinors for $i = A, B$ normalized such that $\chi_i^\dagger \chi_j = \delta_{ij}$ and $\vec{\sigma}$ are the Pauli spin matrices. This allows us to rewrite Equation 2.6 as

$$\begin{aligned} M_{AB} \;=\; & 2\pi\delta(E_0 - E_\beta - E_\nu)\frac{G_\beta}{\sqrt{2}}\int \chi_B^\dagger \Bigg\{ f_1\left(j_0 + \frac{i}{2}(\vec{\sigma}\cdot\vec{\nabla}\vec{\sigma}\cdot\vec{j} + \vec{\sigma}\cdot\vec{j}\vec{\sigma}\cdot\vec{\nabla})\right) \\ & - f_2\vec{\sigma}\cdot(\vec{\nabla}\times\vec{j}) + \frac{i}{2}f_3\left((E_\beta + E_\nu)(\vec{\sigma}\cdot\vec{\nabla}j_0 + j_0\vec{\sigma}\cdot\vec{\nabla}) + \vec{\sigma}\cdot\vec{\nabla}\vec{\nabla}\cdot\vec{j} + \vec{\nabla}\cdot\vec{j}\vec{\sigma}\cdot\vec{\nabla}\right) \\ & + g_1\left(\vec{\sigma}\cdot\vec{j} + \frac{i}{2}\vec{\sigma}\cdot\vec{\nabla}j_0 + j_0\vec{\sigma}\cdot\vec{\nabla}\right) + g_2\left(i\vec{\sigma}\cdot\vec{\nabla}j_0 - (E_\beta + E_\nu)\vec{\sigma}\cdot\vec{j}\right) \\ & - \frac{i}{2}g_3\left((E_\beta + E_\nu)(\vec{\sigma}\cdot\vec{\nabla}j_0 - j_0\vec{\sigma}\cdot\vec{\nabla}) + \vec{\sigma}\cdot\vec{\nabla}\vec{\nabla}\cdot\vec{j} - \vec{\nabla}\cdot\vec{j}\vec{\sigma}\cdot\vec{\nabla}\right)\Bigg\}\chi_A d^3x \end{aligned} \tag{2.8}$$

having integrated over the time coordinate. Thankfully, for fundamental tests of the Standard Model, we usually study decays where only one or two terms in Equation 2.8 dominate.

2.3 The Allowed Approximation

The nuclear dimensions ($\approx 1.2 \times A_N^{\frac{1}{3}}$ fm) are small enough that the lepton wavefunctions (deBroglie wavelength $\sim 4 \times 10^2$ fm at 1 MeV) are essentially constant on that scale. The allowed approximation neglects terms in Equation 2.8 involving derivatives or lepton energies and evaluates the lepton wavefunctions at the origin. Neglecting these terms is equivalent to requiring that the leptons carry off no orbital angular momentum.

The remaining terms are (now summing the contributions from the nucleons)

$$\begin{aligned} M_{AB} &= \frac{G_\beta}{\sqrt{2}} \sum_{i=1}^{A_N} \left(f_1(0) \int \chi'^\dagger \tau_i^\dagger \chi d^3x j_0(0) + g_1(0) \int \chi'^\dagger \vec{\sigma_i} \tau_i^\dagger \chi d^3x \vec{j}(0) \right) \\ &= \frac{G_\beta}{\sqrt{2}} (C_V M_F - C_A M_{GT}) \end{aligned} \tag{2.9}$$

where the typical notation used to simplify the expression is

$$\begin{aligned} C_V &= f_1(0) \\ C_A &= -g_1(0) \\ M_F &= \sum_{i=1}^{A} \int \chi'^\dagger \tau_i^\dagger \chi j_0(0) d^3x \\ M_{GT} &= \sum_{i=1}^{A} \int \chi'^\dagger \vec{\sigma_i} \tau_i^\dagger \chi \vec{j}(0) d^3x. \end{aligned} \tag{2.10}$$

The neglected terms have non-zero lepton orbital angular momentum and are dominant for forbidden decays where both M_F and M_{GT} are zero. For allowed decays, they are $\sim$1% corrections to the matrix element above. These terms, known as recoil order corrections, will be discussed later this chapter.

2.4 β Decay Correlations

To calculate the β decay observables, we evaluate the differential decay rate. We first use the allowed approximation, but make no assumption about the coupling constants defined in Equation 2.2. Corrections are then added as required to achieve the desired precision. The largest and most obvious correction is the electromagnetic interaction between the outgoing β and the nucleus. This scales the decay rate by an additional factor of $\frac{F(Z,p_\beta)}{2E_\beta 2E_\nu}$, where $F(Z, p_\beta)$ is the ratio

$$F(Z, p_\beta) = \frac{|\psi_\beta(0)|^2_Z}{|\psi_\beta(0)|^2_{Z=0}} \tag{2.11}$$

of the β wavefunction at the origin with and without the Coulombic potential. In practice, ψ_β is numerically evaluated by solving the Dirac equation for a β in the presence of a nucleus

of charge Z distributed over a volume determined by a "nuclear radius" R. Orbital electron screening is included for the highest precision. We evaluate the differential decay rate

$$d\Gamma = \frac{1}{(2\pi)^5}\frac{\delta(E_\beta + E_\nu - E_0)}{4E_\beta E_\nu}F(Z,p_\beta)|M|^2 d^3p_\beta d^3p_\nu \tag{2.12}$$

where the neutrino mass is ignored. The nucleus is assumed to be infinitely heavy, and capable of carrying away momentum but not energy. In reality, nuclei have recoil-energies of $\sim$100 eV. This is typically dwarfed by the uncertainty (often $\sim$1 keV) in E_0. The effect on the phase space of including a finite mass for the nucleus is discussed in Ref. [35]. Since it is $\lesssim$0.02% for most decays including ^{21}Na, it will not be considered further. Jackson, Treiman, and Wyld found [36] that for a nucleus with spin $\vec{J}$, unit vector $\hat{j}$ along $\langle\vec{J}\rangle$, and tensor alignment $\frac{J(J+1)-3\langle(\vec{J}\cdot\hat{j})^2\rangle}{J(2J-1)}$,

$$\begin{aligned}\frac{d\Gamma}{dE_\beta d\Omega_\beta d\Omega_\nu} &= \frac{1}{(2\pi)^5}p_\beta E_\beta (E_0-E_\beta)^2\xi\Bigg(F_1(E_\beta) + a_{\beta\nu}(E_\beta)\frac{\vec{p}_\beta\cdot\vec{p}_\nu}{E_\beta E_\nu} + b_{Fierz}(E_\beta)\frac{\Gamma m_e}{E_\beta} \\ &\quad + A_\beta(E_\beta)\frac{\langle\vec{J}\rangle\cdot\vec{p}_\beta}{E_\beta} + B_\nu(E_\beta)\frac{\langle\vec{J}\rangle\cdot\vec{p}_\nu}{E_\nu} + D_{TRV}(E_\beta)\frac{\langle\vec{J}\rangle\cdot(\vec{p}_\beta\times\vec{p}_\nu)}{E_\beta E_\nu} \\ &\quad + c_{align}(E_\beta)\Big(\frac{J(J+1)-3\langle(\vec{J}\cdot\hat{j})^2\rangle}{J(2J-1)}\Big)\Big(\frac{\vec{p}_\beta\cdot\vec{p}_\nu}{3E_\beta E_\nu} - \frac{(\vec{p}_\beta\cdot\hat{j})(\vec{p}_\nu\cdot\hat{j})}{E_\beta E_\nu}\Big)\Bigg)\end{aligned} \tag{2.13}$$

after summing over final spin states. The rate is proportional to

$$\xi = |M_F|^2\Big(|C_V|^2+|C_V'|^2+|C_S|^2+|C_S'|^2\Big) + |M_{GT}|^2\Big(|C_A|^2+|C_A'|^2+|C_T|^2+|C_T'|^2\Big) \tag{2.14}$$

and F_1, $a_{\beta\nu}$, b_{Fierz}, A_β, B_ν, D_{TRV}, and c_{align} depend on the fundamental weak coupling constants and nuclear matrix elements. In the allowed approximation, each is independent of E_β and given in Ref. [36].

2.5 The $\beta-\nu$ Correlation

With no net nuclear polarization or tensor alignment, the differential decay rate in Equation 2.13 reduces to

$$\frac{d\Gamma}{dE_\beta d\Omega_\beta d\Omega_\nu} = \frac{1}{(2\pi)^5}p_\beta E_\beta (E_0-E_\beta)^2\xi\Bigg(F_1(E_\beta)+a_{\beta\nu}(E_\beta)\frac{\vec{p}_\beta\cdot\vec{p}_\nu}{E_\beta E_\nu}+b_{Fierz}(E_\beta)\frac{\Gamma m_e}{E_\beta}\Bigg) \tag{2.15}$$

In the allowed approximation, $F_1(E_\beta) = 1$ and the $\beta - \nu$ correlation coefficient, $a_{\beta\nu}$, and Fierz interference coefficient, b_{Fierz}, are

$$a_{\beta\nu} = \left(|M_F|^2(|C_V|^2 + |C_V'|^2 - |C_S|^2 - |C_S'|^2) - \frac{1}{3}|M_{GT}|^2(|C_A|^2 + |C_A'|^2 - |C_T|^2 - |C_T'|^2) \right) \xi^{-1} \tag{2.16}$$

and

$$b_{Fierz} = \left(- \mathrm{Re}\Big(|M_F|^2(C_S C_V^* + C_S' C_V'^*) + |M_{GT}|^2(C_T C_A^* + C_T' C_A'^*) \Big) \right) \xi^{-1}. \tag{2.17}$$

In the absence of nuclear spin, the remaining terms are symmetric under parity. The sign of $a_{\beta\nu}$ for pure Fermi and pure Gamow-Teller transitions can be understood from angular momentum conservation. In a pure Fermi decay, the nuclear spin remains zero, so no net angular momentum is carried off by the leptons. Since the leptons are emitted with opposite handedness, they must also have momenta in the same direction and therefore $a_{\beta\nu} > 1$. A similar argument shows $a_{\beta\nu} < 0$ in pure Gamow-Teller decays.

When the lepton momenta are aligned, the nuclear recoil is largest. A signature of $a_{\beta\nu} > 0$ is a recoil energy spectrum with many high energy events and few low-energy events. By measuring this spectrum, the $\beta - \nu$ correlation can be deduced without detecting either β or neutrino!

2.6 ^{21}Na β Decay

The decay of ^{21}Na is shown in Figure 2.2. The 22.48 s halflife necessitates simultaneous production and trapping of ^{21}Na atoms. Two states in are accessible by allowed decays, but the majority proceed to the ^{21}Ne ground-state because of greater phase space and contribution from both Fermi and Gamow-Teller matrix elements. Electron capture has a branching ratio $\Gamma_{EC} = 0.087\%$ [37]. Experiments conducted in the early 1960's using NaI detectors to detect the 350 keV and 511 keV γ-rays concluded the excited-state branching ratio, $\mathcal{B}_{ES}$, was 2.2±0.3% [38] and 2.3±0.2% [39]. Depending on the experiment, either one or both annihilation γ-rays were detected in coincidence with the 350 keV γ-ray. The

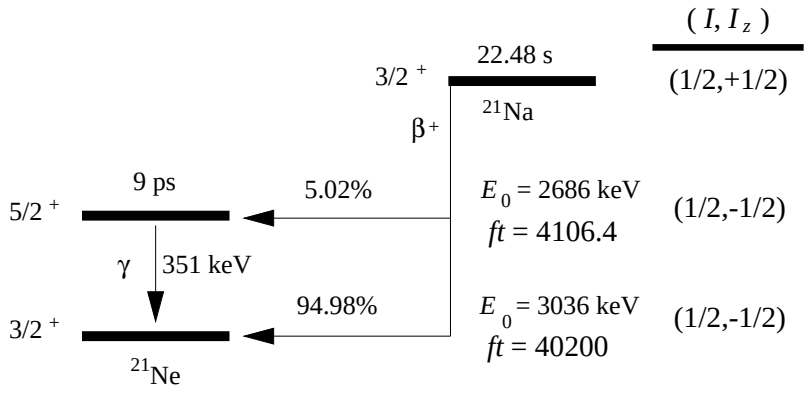

Figure 2.2: β^+ decay of ^{21}Na with isospin (I, I_z) assignments and ft values for each branch. Not shown are 0.087% of decays that proceed by electron capture.

NaI detector used to detect the 350 keV γ-ray was placed 90° from the axis between the source and the other NaI detector or pair of detectors. These experiments suffered from low statistics and poor signal-to-noise. The full-width-half-maximum (FWHM) of the NaI detector at 350 keV was 50 keV. The γ-ray peak overlapped the 341 keV Compton edge of the 511 keV γ-rays. Also, little mention was made of the possible presence of any contaminant β^+ emitters, which would lower the observed branching ratio.

Interest in ^{21}Na resurfaced in the 1970's when a nuclear wavefunction calculation by Wilkinson predicted $\mathcal{B}_{ES}$=5±1% [40]. The branching ratio was remeasured with a single Ge(Li) detector. Corrections were applied for the detection efficiency difference between 350 and 511 keV, the extended distribution of the 511 keV source due to the penetrating ability of the β^+s, and the γ-ray attenuation due to absorber material between source and detector. Contaminant activity was searched for but not found. The result, $\mathcal{B}_{ES} = 5.1\pm0.2\%$ [40], agreed with Wilkinson's calculation, but was in $10\,\sigma$ disagreement with previous measurements.

Since then, there have been two more precise measurements of the excited-state branching ratio. Again using a lone Ge(Li) gamma detector, Azuelos, Kitching, and Ramavataram measured $\mathcal{B}_{ES} = 4.2\pm0.2\%$ [41] and Wilson, Kavanagh, and Mann measured $\mathcal{B}_{ES} = 4.97 \pm 0.16\%$ [42]. Even though the measurements are in poor agreement (see Ta-

ble 2.1), the accepted value in the literature is $\mathcal{B}_{ES} = 5.02 \pm 0.13\%$, obtained by taking the weighted average of the two recent measurements that agree.

A precise value for this branching ratio is crucial for a measurement of the $\beta - \nu$ correlation. The recoil spectra for ^{21}Na decays to the ground and excited-states are shown in Figure 2.3. The maximum recoil energy is 229 eV. For a summary of measurements of ^{21}Na β decay properties, see Table 2.1. The excited-state recoil spectrum differs from ground-state decays for several reasons. The β decay endpoint is smaller, leading to a smaller maximum recoil from lepton emission. The $\beta - \nu$ correlation is different. The subsequent, nearly isotropic, emission of the 350 keV γ-ray gives the nucleus additional recoil (the excited-state lifetime and $\beta - \gamma$ correlation are negligible). The inclusion of these decays amounts to a correction of $+0.0838 \pm 0.0033$ to the ground-state $\beta - \nu$ correlation. The majority of the uncertainty is from the magnitude of the branching ratio. However, any error in the branching ratio effects the ft value of the main decay branch which alters the Standard Model prediction for the $\beta - \nu$ correlation. The effect on the measured value is of opposite sign, casting a larger uncertainty on the comparison to the Standard Model.

The excited-state recoil spectrum differs from ground-state decays for several reasons. The β decay endpoint is smaller, leading to a smaller maximum recoil from lepton emission. The $\beta - \nu$ correlation is different. The subsequent, nearly isotropic, emission of the 350 keV γ-ray gives the nucleus additional recoil. The inclusion of these decays amounts to a correction of $+0.0838 \pm 0.0033$ to the ground-state $\beta - \nu$ correlation. The majority of the uncertainty is from the magnitude of the branching ratio. However, any error in the branching ratio affects the ft value of the main decay branch which alters the Standard Model prediction for the $\beta - \nu$ correlation. The effect is opposite on the Standard Model prediction and measured value, and casts a larger uncertainty on their comparison.

2.7 Determination of Nuclear Matrix Elements

For pure Fermi or pure Gamow-Teller decays, the correlation coefficients are easily calculated because the matrix element dependence in the correlation coefficients divides out.

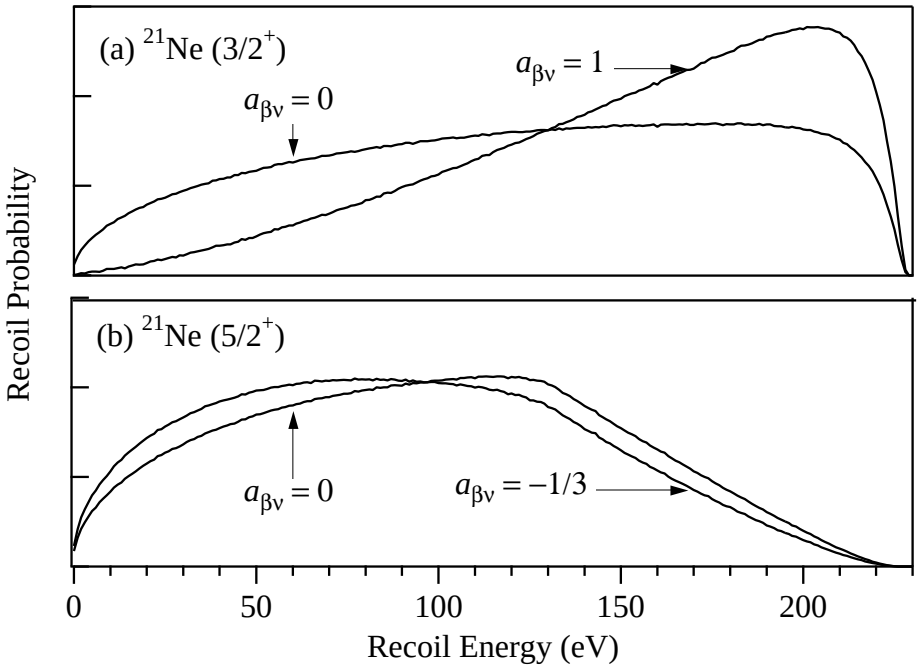

Figure 2.3: Recoil energy spectrum of ^{21}Ne following β^+ decay to (a) the ground-state with $a_{\beta\nu} = 0$ and $a_{\beta\nu} = 1$ and (b) the excited-state with $a_{\beta\nu} = -1/3$ and $a_{\beta\nu} = 0$. Recoil order, order-α radiative and bremsstrahlung effects have been included.

Property	Value	Reference
E_0	2510±20 keV	[43]
E_0	2525.4±0.7 keV	[44]
$\mathcal{B}_{ES}$	2.2±0.3%	[38]
$\mathcal{B}_{ES}$	2.3±0.2%	[39]
$\mathcal{B}_{ES}$	5.1±0.2%	[40]
$\mathcal{B}_{ES}$	4.2±0.2%	[41]
$\mathcal{B}_{ES}$	4.97±0.16%	[42]
Γ_{EC}	0.087%	[37]
$t_{1/2}$	23.0±0.2 s	[45]
$t_{1/2}$	22.55±0.10 s	[40]
$t_{1/2}$	22.48±0.04 s	[41]
E_γ	350.725±0.008 keV	[46]
t_{ES}	10.23±0.20 ps	[47]
Γ_{M1}	$(6.44 \pm 0.13) \times 10^{-5}$ eV	

Table 2.1: Properties of ^{21}Na β decay.

For the ^{21}Na β decay to the ground-state, both matrix elements contribute. The initial and final nuclear states are members of an isodoublet, so $|M_F|^2 = 1$, in the absence of isospin-breaking corrections. These corrections are difficult to calculate reliably and vary from nucleus to nucleus, but are ≈0.4% for the $(0^+ \rightarrow 0^+)$ superallowed Fermi decays [48, 49]. We expect them to be the same size in ^{21}Na.

The Gamow-Teller matrix element, M_{GT}, is not constrained by any symmetry. It is determined by comparing the decay ft value to that of the superallowed Fermi decays. The ft value is the product of the phase space factor:

$$f = \int_{m_e}^{E_0} F(Z, E_\beta) p_\beta E_\beta (E_0 - E_\beta)^2 dE_\beta F_1(E_\beta) \tag{2.18}$$

and the partial halflife $t = t_{1/2}/\mathcal{B}_{ES}$ where $t_{1/2}$ is the total decay halflife. Integrating Equation 2.13 over β and ν energies and momenta gives

$$\Gamma = \frac{G_\beta^2}{2\pi^3} \xi f. \tag{2.19}$$

Since

$$t = \frac{\ln 2}{\Gamma}, \tag{2.20}$$

the combination ft depends only on G_β and the particular nuclear matrix elements through the relationship

$$ft = \frac{2\pi^3 \ln 2}{G_\beta^2 \xi}. \tag{2.21}$$

For the superallowed Fermi decays, the transitions are within an isotriplet so $M_F = \sqrt{2}$ (in the absence of isospin breaking corrections), and with $C_V = 1$, we find $\xi = 2$. Measurements of the ft values of the superallowed Fermi decays are a precise way to determine V_{ud}, and currently the CKM matrix is $2.2\,\sigma$ below the unitarity condition [50]. Recoil order and radiative corrections are applied to F_1 to calculate ft to a precision of 0.1%. For the transition $^{21}\mathrm{Na}(3/2^+) \rightarrow ^{21}\mathrm{Ne}(3/2^+)$, the properties E_0, $t_{1/2}$, and $\mathcal{B}_{ES}$ necessary to determine the ft value have been measured with a precision of ≈0.1% and are summarized in Table 2.1.

The ft values for both the superallowed Fermi decays and ^{21}Na decays to the ground-state are calculated in Ref. [51] with similar corrections. Taking the ratio gives

$$\frac{ft(0^+ \rightarrow 0^+)}{ft(^{21}\mathrm{Na}(3/2^+) \rightarrow ^{21}\ \mathrm{Ne}(3/2^+))} = \frac{1 + |C_A|^2 |M_{GT}|^2}{2} \tag{2.22}$$

and with $ft(0^+ \rightarrow 0^+) = 3070.6 \pm 1.6\,\mathrm{s}$ and $ft(^{21}\mathrm{Na}(3/2^+) \rightarrow ^{21}\mathrm{Ne}(3/2^+)) = 4106.4 \pm 11.6\,\mathrm{s}$, we find $C_A M_{GT} = \pm(0.704 \pm 0.003)$. Ref. [51] indicates the sign is negative. The sign only effects recoil order corrections. We calculate $ft(^{21}\mathrm{Na}(3/2^+) \rightarrow ^{21}\mathrm{Ne}(5/2^+)) = 40200 \pm 1000\,\mathrm{s}$ for excited-state decays, and a similar analysis gives $C_A M_{GT} = \pm(0.391 \pm 0.005)$. Since this decay is pure Gamow-Teller, the matrix element is only important for recoil order corrections. The uncertainty is dominated by the 2.6% fractional uncertainty in $\mathcal{B}_{ES}$. We neglect recoil order corrections (although order-α radiative corrections have been included).

The coefficients for ground-state (GS) and excited-state (ES) decays are summarized in Table 2.2. In the absence of tensor interactions, $b_{Fierz} = 0$ for excited-state decays, and in the absence of both scalar and tensor interactions, $b_{Fierz} = 0$ for the ground-state decays. If the fundamental coupling constants have no imaginary components, $D_{TRV} = 0$

Correlation	GS value	ES value
$a_{\beta\nu}$	$+0.558 \pm 0.003$	$-\frac{1}{3}$
A_β	$+0.862 \pm 0.002$	$-\frac{3}{5}$
B_ν	$+0.5967 \pm 0.0004$	$+\frac{3}{5}$
c_{align}	$+0.265 \pm 0.002$	$-\frac{1}{5}$

Table 2.2: Standard Model predictions for the non-zero correlation coefficients defined in Equation 2.13.

for both decay branches. The interaction of the charged nucleus and emitted β (i.e. final-state effects) mimic the effect of D_{TRV}, but are $\approx 1.9 \times 10^{-4} \frac{E_\beta}{E_0} - 0.1 \times 10^{-4} \frac{E_0}{E_\beta}$ for ^{21}Na ground-state decays [52] from the size of the weak magnetism term determined below.

2.8 Beyond the Allowed Approximation

For precision β decay tests of the Standard Model, a number of corrections to the allowed approximation must be included as they can be as large, or larger than the desired experimental sensitivity. Corrections tend to be ~1% of the dominant allowed order terms and contribute energy dependence to $F_1(E_\beta)$ and the decay correlation coefficients. They alter the calculated ft value, which impacts the allowed approximation prediction for the decay correlations. Wilkinson extensively discusses relevant corrections to Equation 2.8 used to calculated ft values to the highest precision (often to a precision of $\sim 10^{-5}$) in a series of papers on the "Evaluation of Beta-Decay" [53, 35, 54, 55, 56, 57]. We have divided the corrections into "recoil order" corrections which are due to neglected term in Equation 2.8, and "radiative" corrections from photon loops or bremsstrahlung. Of course, we have already applied the largest electromagnetic correction when we included $F(Z, E_\beta)$ in Equation 2.12.

2.8.1 Recoil Order Corrections

The terms proportional to ∇ and $(E_\beta + E_\nu)$ in Equation 2.8 contribute small, energy dependent corrections to $F_1(E_\beta)$ and the decay correlation coefficients to allowed

Matrix element	Ground-state	Excited-state
a	1	0
b	82.63	21.8±0.2
c	−0.704±0.003	±(0.391 ± 0.007)
d	0	0

Table 2.3: Matrix elements for ^{21}Na ground-state and excited-state decays.

decays. These terms are proportional to the nuclear recoil and are of order $\frac{E_0}{M}$ which is $\approx 10^{-3}$ for most β decays, including ^{21}Na. Many experiments have tested recoil order corrections, with results in agreement with theory at the level of 10–20% [30].

Since the experiment measured the recoil energy spectrum, these corrections are included for both F_1 and $a_{\beta\nu}$ (we neglect them for b_{Fierz} because it expected to be zero) as

$$F_1(E_\beta) = 1 + \delta^1_{ro}(E_\beta) \qquad \text{and} \qquad a_{\beta\nu}(E_\beta) = a^0_{\beta\nu}(1 + \delta^a_{ro}(E_\beta)) \tag{2.23}$$

where 1 and $a^0_{\beta\nu}$ are the allowed order results for F_1 and $a_{\beta\nu}$, and $\delta^1_{ro}(E_\beta)$ and $\delta^a_{ro}(E_\beta)$ are their recoil order corrections. These corrections have been calculated and summarized by Holstein in Ref. [58] and here we use his results and notation. In Holstein's notation, $a = C_V M_F$, b is the weak magnetism term and can be determined by the conserved vector current hypothesis, $c = C_A M_{GT}$, and d is the induced tensor term. The ground-state and excited-state matrix elements are summarized in Table 2.3. A non-zero d in isodoublet decays would imply the existence of second-class currents [59].

The calculated recoil order corrections are

$$\delta^1_{ro}(E_\beta) = \frac{2}{3M}\frac{E_0 \mathrm{Re}(c^*(d-b)) - 2E_\beta \mathrm{Re}(c^* b)}{|a|^2 + |c|^2} - \frac{m_e^2}{M E_\beta}\frac{\mathrm{Re}(c^*(d-2b))}{|a|^2 + |c|^2} \tag{2.24}$$

and

$$\delta^a_{ro}(E_\beta) = \frac{2}{3M}\frac{E_0 \mathrm{Re}(c^*(d-b)) + 2E_\beta \mathrm{Re}(c^* b)}{|a|^2 - \frac{1}{3}|c|^2}. \tag{2.25}$$

Assuming the CVC hypothesis and the absence of SCC,

$$\langle \delta^1_{ro} \rangle \approx -0.00042 \qquad \text{and} \qquad \langle \delta^a_{ro} \rangle \approx 0.00039, \tag{2.26}$$

although we include the energy dependence in the analysis.

2.8.2 Weak Magnetism Term

In mirror decays, the CVC hypothesis relates b to the magnetic moments of the isodoublet pair by

$$b = A_N \sqrt{\frac{J+1}{J}} M_F \frac{\mu(I_3) - \mu(I_3')}{I_3 - I_3'} \tag{2.27}$$

where $\mu(I_3)$ and $\mu(I_3')$ are the nuclear magnetic moments of the parent and daughter nuclei of isospin I_3 and I_3', respectively. The ^{21}Na [60] and ^{21}Ne [61] magnetic moments have been measured with sufficient precision and we find $b = +82.63$.

For the excited-state decays, CVC relates b to the width, Γ_{M1}, and energy, E_γ, of the associated M1 decay. The result

$$\Gamma_{M1} = \frac{1}{6} \alpha E_\gamma^3 \frac{b^2}{M^2} \tag{2.28}$$

predicts the magnitude of b but not its sign. The excited-state lifetime is $t_{ES} = 10.23 \pm 0.20$ ps [47], which gives $\Gamma_{M1} = (6.44 \pm 0.13) \times 10^{-5}$ eV. We then calculate $b = \pm(21.8 \pm 0.2)$ using Equation 2.28. The uncertainty in signs leads to uncertainty in the recoil order corrections but the small size of the corrections together with the small branching ratio, make the uncertainty in measuring the ground-state $\beta - \nu$ correlation negligible.

2.8.3 Excited-State $\beta - \gamma$ Correlation

For excited-state decays, a $\beta - \gamma$ correlation exists when recoil order contributions are included. The angular distribution [58] is

$$1 + g(E_\beta) \frac{\vec{p}_\gamma \cdot \vec{p}_\beta}{E_\gamma E_\beta} \tag{2.29}$$

where

$$\begin{aligned} g(E_\beta) &= \frac{2E_0}{3M}\Big(- a^2 + \frac{c^2}{3}(1 - \frac{\lambda^j_{j'j''}}{10})\Big) - \frac{4E_\beta}{3M}\Big(a^2 + \frac{5c^2}{3}(1 - \frac{\lambda^j_{j'j''}}{100})\Big) \\ &\approx -8 \times 10^{-5} + 8 \times 10^{-5} E_\beta \end{aligned} \tag{2.30}$$

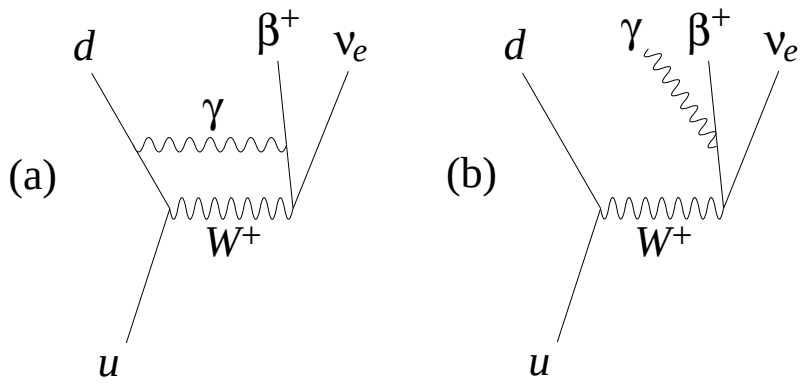

Figure 2.4: Some photon exchange terms that lead to order-α radiative corrections. In (a) the β^+ and d quark in the daughter neutron exchange a virtual photon, while in (b) the β^+ emits a hard bremsstrahlung photon.

for excited-state ^{21}Na decays where $\lambda^{j}_{j'j''} = -\frac{1}{7}$ and depends on the nuclear spin of the parent ground-state (j), daughter excited-state (j'), and daughter ground-state (j'') as defined in Ref. [62]. This effect is negligible, and the γ-ray is considered to be emitted isotropically.

2.8.4 Order-α Radiative Corrections

Higher order radiative corrections beyond the dominant Coulomb-distortion of $\psi_\beta(x^\mu)$ taken into account by the Fermi function need to be included in precision β decay work. Photon exchange diagrams, such as those shown in Figure 2.4, lead to order-α corrections that are divided into "inner" corrections and "outer" corrections. The "inner" corrections depend on the structure of the weak vertex and their effect is only to alter the vector and axial-vector coupling constants from their "bare," and incalculable, values. They are just absorbed into the calculation of $\frac{C_A}{C_V}$. The "outer" corrections, at lowest order, are independent of the weak and strong interactions and are divided into Z-dependent and Z-independent terms.

Z-Dependent Outer Radiative Corrections

The Z-dependent corrections are clearly presented in Ref. [63]. They have been calculated, assuming a uniform charge and "weak charge" density, to be

$$\delta_{em}^{1} = \frac{6\alpha ZR}{35}\left(\frac{|a|^2 - \frac{1}{3}|c|^2}{|a|^2 + |c|^2}E_0 + \frac{8|a|^2 + \frac{28}{3}|c|^2}{|a|^2 + |c|^2}E_\beta + \frac{3m_e^2}{E_\beta}\right) \tag{2.31}$$

and

$$\delta_{em}^{a} = \frac{6\alpha ZR}{35}\left(E_0 + \frac{8|a|^2 - 4|c|^2}{|a|^2 - \frac{1}{3}|c|^2}E_\beta\right) \tag{2.32}$$

where α is the fine structure constant, Z is the parent nucleus charge, and $R \approx 0.02\,\mathrm{MeV}^{-1}$ is the nuclear radius. Terms involving recoil order contributions are negligible in size. For ^{21}Na, the Z-dependent corrections give average corrections of

$$\langle\delta_{em}^{1}\rangle \approx 0.0044 \qquad \text{and} \qquad \langle\delta_{em}^{a}\rangle \approx 0.0047 \tag{2.33}$$

to F_1 and $a_{\beta\nu}$.

Z-Independent Outer Radiative Corrections

Sirlin calculated the order-α, Z-independent corrections applicable to allowed β decay [64]. He defined a universal function $g(E_\beta, E_0)$ that accounts for photon loops and emission of bremsstrahlung photons. Until recently, $g(E_\beta, E_0)$ was incorrectly applied in experiments that detect β and recoil momenta in coincidence by including its effect on the β spectrum and then inferring the neutrino momentum from $\vec{p}_\nu = \vec{p}_r - \vec{p}_\beta$. When decays involving the emission of a hard bremsstrahlung photon are included, the final state is not three-body since the undetected hard photon carries away momentum and energy. The kinematic variables are not related through $E_0 = E_\beta + E_\nu$ and $\vec{p}_r + \vec{p}_\beta + \vec{p}_\nu = 0$. Although hard bremsstrahlung emission occurs in only $\approx 1\%$ of decays, it appreciably alters the kinematics because its energy spectrum extends to E_0. General expressions are unwieldy for the four-body kinematics in which both the β and recoiling nucleus are detected. The corrections are included using a Monte Carlo sampling method outlined in Ref. [65].

Chapter 3

Measuring the $\beta - \nu$ Correlation

Measurements of $\beta - \nu$ correlations are challenging. The neutrino (ν) is difficult to detect so the correlation must be inferred from the nuclear recoil. The energy release is small compared to the nuclear mass, leading to recoil energies of zero to a few hundred eV. Daughter nuclei of these energies are difficult to detect directly and are prone to even the smallest source scattering and molecular effects. Even a single molecular bond causes systematic distortions comparable to $a_{\beta\nu}$ [66]. For most applications, solid targets, no matter how thin, cannot be used so radioactive noble gases or neutron beams are typically used.

The correlation is determined from the distribution of recoils. A positive $\beta - \nu$ correlation coefficient, $a_{\beta\nu}$, aligns the β and ν momenta, resulting in larger recoil momenta. The determination of $a_{\beta\nu}$ is sensitive to detector resolutions and efficiencies as well as any approximations made about the underlying physics. Nevertheless, a handful of precision measurements have been made over the past 40 years through clever techniques. Each of the experiments summarized in Table 3.1 relied on one of the techniques to be discussed in the following sections.

Nucleus	Year	$a_{\beta\nu}$	SM prediction	Technique
^{19}Ne	1959	0.00±0.08 [13]	mixed	recoil energy spectrum
^{6}He	1963	−0.3343±0.0030 [15]	−1/3	recoil energy spectrum
^{23}Ne	1963	−0.33±0.03 [16]	−1/3	recoil energy spectrum
n	1978	−0.1017±0.0051 [67]	mixed	recoil energy spectrum
^{18}Ne	1997	+1.06±0.10 [68]	+1	γ-ray Doppler shift
^{32}Ar	1999	+0.9989±0.0065 [69]	+1	β-delayed proton energy
^{33}Ar	1999	+0.944±0.004 [70]	mixed	β-delayed proton energy

Table 3.1: Summary of the most precise $\beta - \nu$ correlation coefficient results for each isotope. Only results with uncertainty <0.10 are included.

3.1 Past $\beta - \nu$ Correlation Measurements

3.1.1 Direct Measurement of Recoil-Ion Spectra

Electrostatic acceleration boosts the recoil-ion energies to easily detectable levels (typically several keV). This allows direct measurement of the energy spectrum either through time-of-flight techniques or from magnetic and electrostatic analyzers.

The first measurement of a $\beta - \nu$ correlation with a precision of 0.01 was made by studying the energy spectrum of the Gamow-Teller decay of ^{6}He. A magnetic spectrometer analyzed the energy of ^{6}Li ions passing through a small opening at the tip of the conical source volume. Ions of a selected energy were subsequently accelerated and detected with an electron multiplier. The spectrum was determined from the count rate at several recoil energies. The result, $a_{\beta\nu} = -0.3343 \pm 0.0030$ [15], demonstrated that Gamow-Teller decays proceed predominantly through an axial-vector interaction (which predicts $a_{\beta\nu} = -1/3$) with possible tensor contributions less than 10% of the axial-vector magnitude. The experiment was done with ^{23}Ne using the same apparatus, but imprecise knowledge of β decay branching ratios dominated the uncertainty and compromised the result [16]. A measurement of these branching ratios to 1% fractional uncertainty (they have been measured to 10% fractional uncertainty [71]) would allow the recoil-ion spectrum to test the $V - A$ structure with a precision of 0.006.

The proton recoil spectrum following neutron β decay was most precisely measured with an electrostatic spectrometer. The result, $a_{\beta\nu} = -0.1017 \pm 0.0051$, obtained by Stratowa, Dobrozemsky, and Weinzierl in 1978 is also consistent with the $V - A$ structure [67]. With a fractional uncertainty of 5%, this result does not put competitive limits on non-Standard Model couplings. There is a proposal to do an improved neutron $\beta - \nu$ correlation experiment with a magnetic spectrometer similar to those used to search for $\bar{\nu_e}$ mass in tritium decay [72]. The goal of this ambitious experiment is to reduce systematic effects to $\sim 5{\times}10^{-5}$ and obtain comparable statistical uncertainty.

3.1.2 Recoil Inference from Kinematic Shift

Another measurement technique infers the recoil momentum from the kinematic shift in subsequent radiation or particle emission from an unstable daughter nucleus. This technique avoids directly detecting the low-energy recoil. Experimenters detect γ-rays or MeV-energy protons, either of which is done easily and accurately.

The $\beta - \nu$ correlation in the superallowed $0^+ \rightarrow 0^+$ β decay of ^{32}Ar was recently measured using this approach. The daughter nucleus, ^{32}Cl, is unstable to proton emission and decays before the nuclear momentum is perturbed, even in a solid target. The broadening of the proton energy spectrum by $a_{\beta\nu} > 0$ was precisely measured using *p-i-n* diode detectors. The agreement between the result, $a_{\beta\nu} = 0.9989 \pm 0.0065$ [69], and the Standard Model prediction ($a_{\beta\nu} = 1$) improved constraints on scalar contributions.

For β decay to an excited nuclear state that subsequently decays through γ-ray emission, the $\beta - \nu$ correlation is determined from the dependence of the γ-ray Doppler shift on β energy. A positive correlation results in larger Doppler shifts, an effect that is more pronounced at lower energies. A value of $a_{\beta\nu} = 1.06 \pm 0.10$ was measured for the superallowed pure Fermi decay $^{18}\mathrm{Ne}(0^+) \rightarrow ^{18}\mathrm{F}(0^+)$, by detecting the subsequent emission of the 1040 keV γ-ray in coincidence with the β^+ [68]. However, this branch constitutes only 8% of all decays and the small solid angles subtended by β and γ-ray detectors make acquiring sufficient statistics for a precision measurement difficult. Even with 14 Si(Li)

β-detectors and 2 HPGe γ-ray detectors, the experiment is currently limited by statistics.

3.2 Trapped Radioactive Atoms

Trapped radioactive atoms are appealing for the next generation of precise β decay correlation measurements. Both β^+s and recoiling daughters emerge from the trap volume with negligible scattering or molecular interactions and subsequently propagate in an ultra-high vacuum environment to the radiation detectors. The trap collects only atoms of the desired isotope. The source is small (trap FWHM $\approx$1 mm) and the atoms decay essentially at rest, since the trap temperature is $<$1 mK. In addition, for traps like the magneto-optical trap, the spatial distribution of atoms is monitored online from the fluorescence. For these reasons, a radioactive atom trap is particularly well-suited for the direct measurement of the β and recoil nucleus in coincidence. The low energy of the recoil-ions allows 100% focusing to a 44 mm diameter detector with modest ($\approx$1 kV/cm) electric fields.

Optical pumping duty cycles or an inherently spin-polarizing trap can provide nearly 100% polarized samples. A controlled and well-characterized nuclear spin would allow measurements of other correlation coefficients such as the β-asymmetry A_β, the ν-asymmetry B_ν, the nuclear alignment term c_{align}, and the time-reversal-violating D_{TRV} coefficient. The technique used to measure the $\beta - \nu$ correlation could easily be adapted to measure these coefficients.

Several research groups have begun trapping radioactive alkali atoms for precision β decay measurements. At TRIUMF, mass-separated, radioactive ion beams from TISOL and ISAC are neutralized and the atoms cooled and loaded into a trap. ^{38m}K and ^{37}K atoms have been collected in MOTs to measure the $\beta - \nu$ correlation using the technique discussed in this dissertation [22]. Systematic uncertainties are currently being investigated. A measurement of D_{TRV} in ^{37}K is also underway, by loading the atoms from the MOT into a spin-polarizing far-off resonance trap (FORT) and using a similar detection technique. At Los Alamos, ^{82}Rb atoms are loaded into a time-orbiting-potential (TOP) trap [73]. The nuclear polarization follows a rotating bias field and A_β can be measured by detecting the

beacon of β^+s that are emitted along the polarization direction. Work continues to improve the signal-to-noise and nuclear polarization, and coincident ion detection is being considered [74]. Other radioactive atoms, such as ^{210}Fr [75, 76] and ^{221}Ra [77] are being trapped for tests of atomic parity violation, measurements of the anapole moment, or to search for an electric dipole moment.

One of the difficulties of collecting activity with an atom trap is the generally small capture efficiencies that have been achieved. For work with short-lived radioactive isotopes, atoms are generated using an accelerator beam [78]. At typical cross sections of $\sim 10^{-25}$ cm^2 and beam currents of microamps, only 10^{10} atoms/sec of the isotope of interest are created. MOT efficiency is at a premium and loss mechanisms must be minimized. After years of optimization, we estimate the capture efficiency at only 0.01%. With a 2 μA proton beam, we have at most 10^6 trapped atoms.

3.3 Production of ^{21}Na

The production and transport of ^{21}Na to a magneto-optical trap (MOT) has been extensively described elsewhere [79, 80, 81] and we will only summarize here. The ^{21}Na is produced through ^{24}Mg(p,α)^{21}Na by bombarding a powdered MgO target with 2μA of 25 MeV protons from the 88-Inch Cyclotron at Lawrence Berkeley National Laboratory. The alumina crucible containing the target is heated to $\approx$1000° C and the sodium diffuses out of the target at a rate of $\sim 3 \times 10^8$ atoms/sec. The atomic beam emerges through four narrow, alumina tubes aimed at the trapping chamber. Additional collimation 10 cm downstream from the beam nozzles is provided by two-dimensional optical molasses generated by 1 cm laser beams reflected 4 times across the atomic beam.

3.4 Trapping of ^{21}Na

The laser light at 589 nm for the transverse cooling stage and the MOT are generated by two Coherent 899 ring dye lasers using Rhodamine 6G dye. A Coherent Innova 400

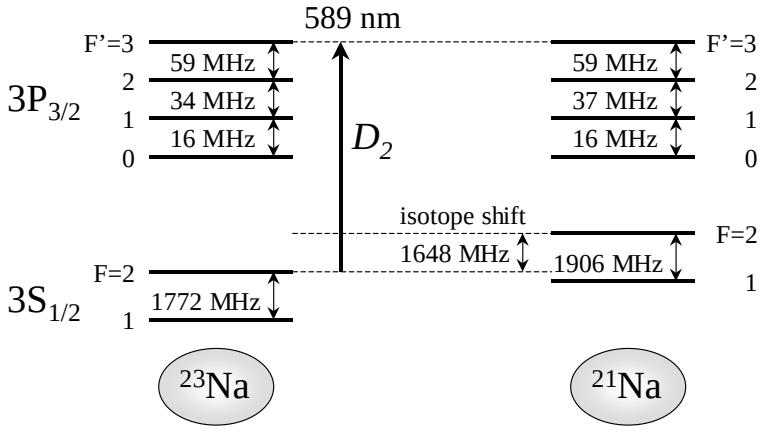

Figure 3.1: Atomic levels used in trapping ^{23}Na and ^{21}Na atoms. Energy separations are not drawn to scale.

Ar^+ laser with 6 W in the single 514 nm line pumps the MOT dye laser and a Coherent Innova 300 Ar^+ with 6 W over all the lines pumps the transverse cooling dye laser. At these pump beam powers, the dye lasers give 800 mW and 600 mW of light for the MOT and transverse cooling beams, respectively. The lasers are frequency stabilized with saturated absorption spectroscopy on the D_2 transition in ^{23}Na. The atomic hyperfine levels used to trap ^{23}Na and ^{21}Na are shown in Figure 3.1. The natural linewidth, Γ, of the D_2 transition is $\Gamma = 2\pi \times 9.89$ MHz. When trapping ^{21}Na, we account for the 1648 MHz isotope shift by passed the beam through an acousto-optic modulator. An electro-optic modulator shifts $\approx$10% of the laser power to the $3^2S_{1/2}(F = 1)$ to $3^2P_{3/2}(F = 2)$ transition frequency for the isotope of interest, avoiding optical pumping to the untrapped $3^2S_{1/2}(F = 1)$ hyperfine level.

3.4.1 Trapping Chamber

A cylindrical trapping chamber 40.64 cm long with a diameter of 14.6 cm was adequate for accommodating electrodes and radiation detectors. A smaller chamber would make it difficult to detect all recoil-ions without large electric fields (>1 kV/cm). Twelve flanges provide optical access for trapping and slowdown laser beams, and allow a CCD

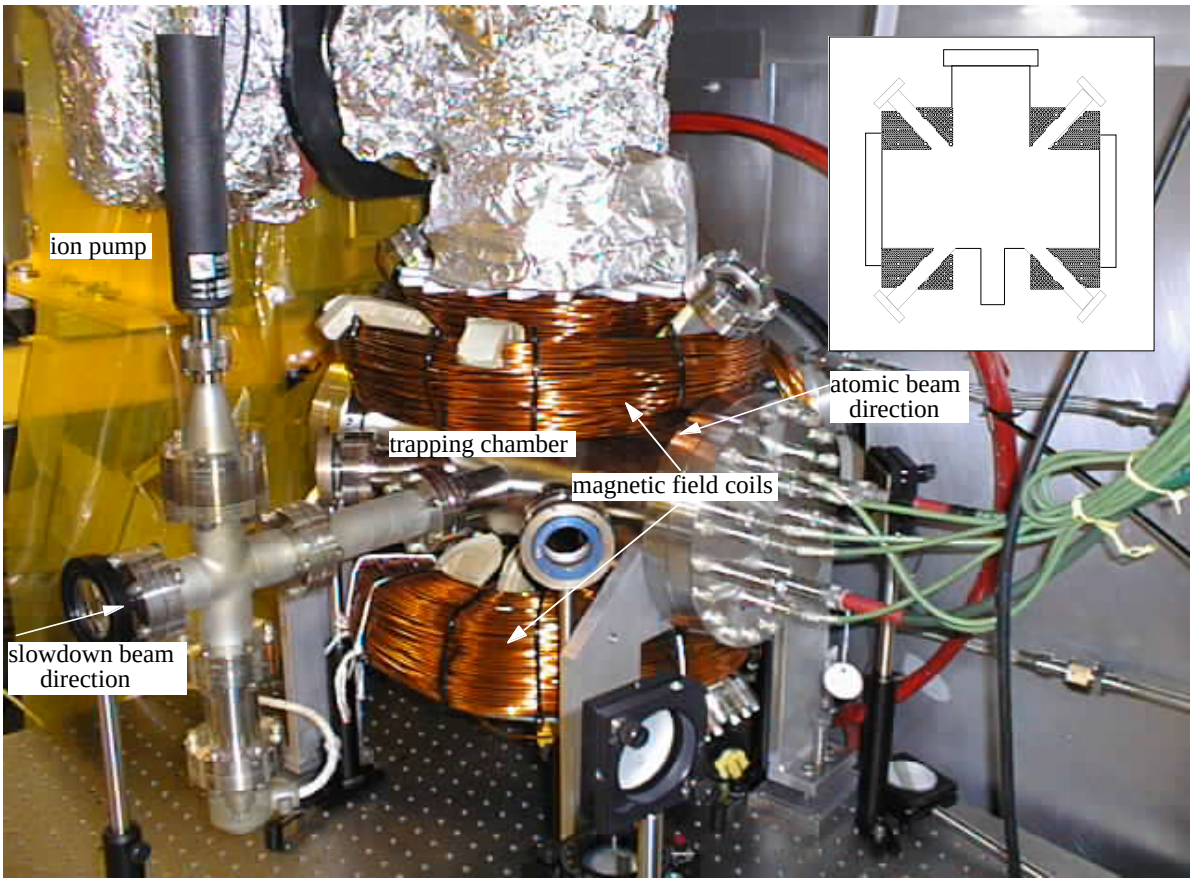

Figure 3.2: Trapping chamber photo. Inset: cross-section view of chamber and copper wire coils that generate the magnetic field.

camera and PMT to image the trap fluorescence. The PMT monitors the trap population, while the CCD camera determines the trap position and distribution. Two viewports are spare, allowing additional optical access if needed. Four coils of 373 turns of heavy-formvar insulated, 12 AWG copper wire generate the anti-Helmholtz magnetic field. The chamber and coils are shown in Figure 3.2.

The coils generate a magnetic field gradient of 20 G/cm in the axial direction and 10 G/cm in the radial direction with a current of 7.2 A. With this current, the coils dissipate 250 W of power and reach a steady state temperature of 40 °C. The 55 kg mass of the coils minimizes the resistive heating eliminated the need for water cooling. Operating the coils at 5 A to maximize the trapping efficiency, reduced the temperature to 35 °C.

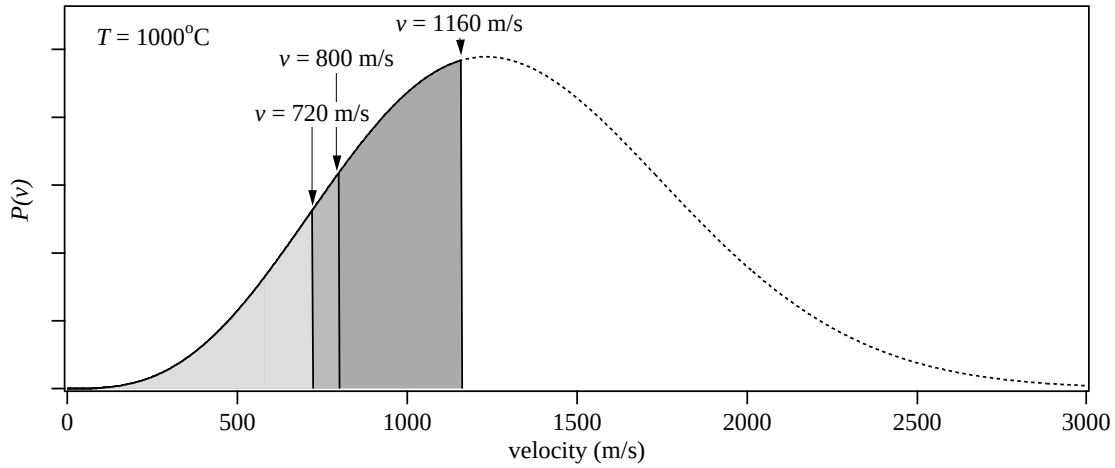

Figure 3.3: $P(v)$ for the collimated beam at 1000°C. The gray sections show the velocities slowed by the Zeeman slower settings used in Ref. [81] (<720 m/s), this work (<800 m/s), and with $s \to \infty$ (<1160 m/s).

The slow ^{21}Na atoms are captured in a six-beam MOT. The trapping laser beams are 3.5 cm in diameter, have a detuning of $\approx \Gamma$, and each have an intensity of $\approx$6 mW/cm^2. We have collected and maintained up to 8×10^5 ^{21}Na atoms in a magneto-optical trap for 30 hours. The lifetime of an atom in the trap is 12±2 s.

3.4.2 Zeeman Slower Magnetic Field

The capture velocity, v_c, of the MOT is much smaller than the average velocity of the hot ^{21}Na emerging from the oven. Figure 3.3 shows the distribution of velocities, v, of atoms emerging from the exit tubes at a typical oven temperature of $T = 1000$°C. The velocity distribution $P(v)$ is

$$P(v) = \frac{M^2}{2k^2T^2} v^3 e^{-\frac{Mv^2}{2kT}} \tag{3.1}$$

which is the Maxwellian distribution weighted by an additional factor of v. Here k is Boltzmann's constant and M is the mass of the atoms.

To slow the thermal atomic beam to velocities low enough to be captured by the MOT, a counterpropagating σ^+ circularly-polarized slowdown beam with detuning $\Delta = \nu_L - \nu_0 = -30$ MHz below the $3S_{1/2}(F = 2, m_F = 2) \to 3P_{3/2}(F = 3, m_F = 3)$ resonance

is used, where ν_L is the laser frequency and ν_0 is the atomic transition frequency (at zero magnetic field). For atomic transition of wave-vector k and Zeeman constant γ, the variation in Doppler shift, kv, is compensated for by a spatially-varying magnetic field, $B(z)$, through the Zeeman shift $\gamma B(z)$. Each position, z, within the 1.2 m long Zeeman slower will be at resonance for

$$kv = -\Delta + \gamma B(z). \tag{3.2}$$

Ideally, this condition is met at the highest possible velocity and is continuously maintained until $v < v_c$. The maximum velocity that is slowed depends on the highest $B(z)$ of the Zeeman slower. The maximum deceleration, a_{max}, the atoms can experience constrains the spatial profile of $B(z)$ if the condition in Equation 3.2 is to be satisfied over all z. A simple calculation in Ref. [82] shows that for efficient slowing (i.e. maintaining a deceleration rate smaller than a_{max}), the magnetic field gradient should be less than

$$\left.\frac{dB(z)}{dz}\right|_{max} = \frac{\Gamma\hbar\pi k^3}{\gamma M(-\Delta + \gamma B(z))}\frac{s}{s+1} \tag{3.3}$$

at all z. The saturation parameter, $s = \frac{I}{I_0}$, where $I_0 = 6.0\,\mathrm{mW}$ for sodium. Figure 3.4 shows both $B(z)$ and $\frac{dB(z)}{dz}$ for the magnetic field settings used and listed in Table 3.2 in the majority of runs. The slowdown beam had an intensity of $6\,\mathrm{mW/cm^2}$ in the D_2 line (and $1\,\mathrm{mW/cm^2}$ in the D_1 line) that was focused to an average of $\approx 24\,\mathrm{mW/cm^2}$ ($s = 4.0$) within the Zeeman slower. The field gradient is below the maximum allowable over the length of the Zeeman slower and the maximum $B(z) = 970$ Gauss corresponds to $v = 800\,\mathrm{m/s}$. At oven temperatures of 1000°C (1200°C), we estimate 13.6% (10.7%) of the beam can be slowed. This is an improvement of nearly 50% over the magnetic field configuration quoted in Ref. [81] at these temperatures [83]. If more power were available for the slowdown beam, a_{max} could be higher. For $s \to \infty$, we find $\frac{dB(z)}{dz}|_{max}$ could be increased by nearly a factor of two. This would allow a maximum $B(z) = 1400$ Gauss and 38% of the atomic beam at 1000°C could be slowed.

Efficient loading from the atomic beam requires the slowdown laser beam to pass directly through the trap. Trapped atoms experience an unbalanced radiation pressure that

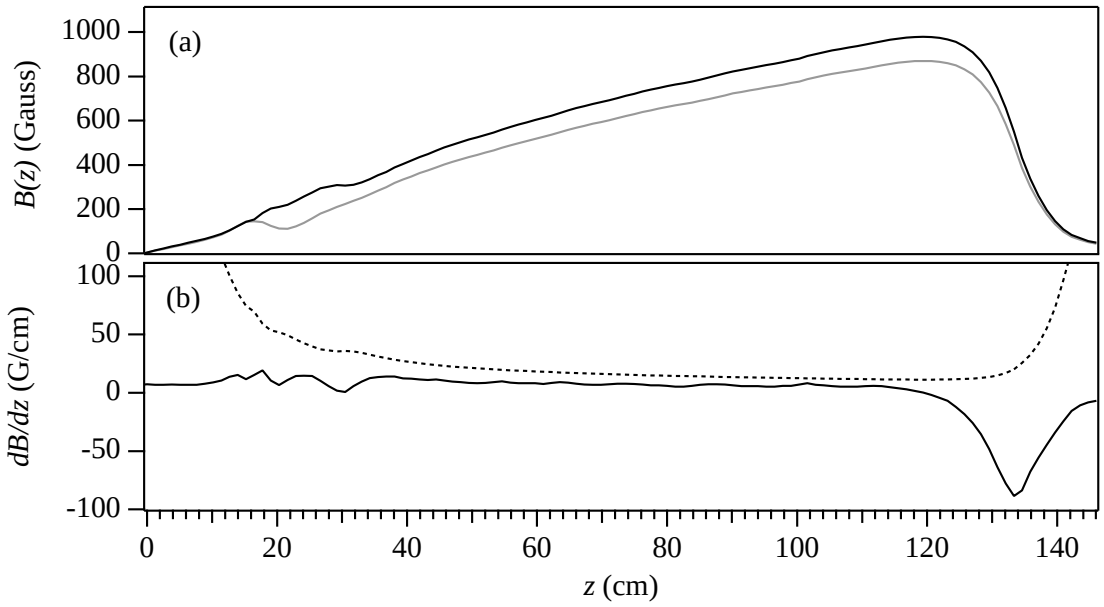

Figure 3.4: Magnetic field settings used. In (a), the black line is the magnetic field used currently and the gray line is the field from Ref. [81]. In (b), the solid line is $\frac{dB(z)}{dz}$ while the dashed line is $\frac{dB(z)}{dz}|_{max}$.

Field Number	Description	Current (Amps)
#1	tapered Zeeman slower	4.10
#2	constant Zeeman slower	2.16
#3	Trapping quadrupole	5.0
#5	Extractor (closest to trap)	4.2
#7	Extractor (furthest from trap)	2.66
#8	Unswitched Helmoltz	−0.6

Table 3.2: Summary of currents used. Notation used is identical to Ref. [81].

increases with laser intensity. This pressure can be eliminated (while keeping the beam on-axis) by either inverting the Zeeman slower field so that the slowdown beam frequency is greatly detuned from resonance at the zero magnetic field of the MOT [84], or placing a "dark spot" in the center of the slowdown beam to cast a shadow over the area of the trap [85]. Since reworking the Zeeman slower (which is embedded in a radiation shield wall) would have been difficult, we opted to sacrifice ~1% of the slowdown beam intensity by placing a 4 mm dark spot at its center. We position the dark spot by observing the trap shape and position. When the unbalanced radiation pressure is eliminated, the trap becomes nearly spherical and shifts 1 mm closer to the center of the trapping laser beams.

By implementing the changes to the slowdown beam and magnetic field profiles described here, we were able to load 5–10 times more atoms into the MOT. This is not as dramatic as the enhancement of a factor of 30 reported in Ref. [85] most likely because the slowdown laser intensity is 10 times smaller.

3.5 Trap Population Measurement

We measure the number of atoms maintained in the trap by detecting the scattered photons from the trapping laser beams. The intensity of radiated light is

$$R = \frac{\Gamma}{2}\frac{s}{1 + s + \frac{4(2\pi\delta)^2}{\Gamma^2}} \tag{3.4}$$

with detuning of laser light, $\delta = 8\,\mathrm{MHz}$. The trap consists of 6 beams with intensity $I = 5.0 \pm 1.0\,\mathrm{mW}$ each so $s = 5.0 \pm 1.0$. We expect $R = 5.6 \pm 0.3\,\mathrm{pW/atom}$ emitted isotropically. The number of atoms maintained in the trap, N, is determined from the trap fluorescence F measured in volts at the PMT viewing the trap as

$$N = \frac{F}{R\Omega_{ph}C} \tag{3.5}$$

where $\Omega_{ph} = (1.18 \pm 0.05) \times 10^{-3}$ is the fraction of trap fluorescence observed by the PMT and $C = (3.4 \pm 0.1) \times 10^{-4}\,\mathrm{V/pW}$ is the conversion between light at the PMT and its voltage output.

Chapter 4

$\beta - \nu$ Correlation Apparatus

4.1 Overview

The experimental arrangement used to obtain the most precise results is shown in Figure 4.1. The trapped atoms are suspended between a β-detector and an ion detector. The sudden change in nuclear charge leads to ^{21}Ne in a variety of charge-states through shake-off and Auger processes. A system of electrodes generates a static electric field to guide recoil-ions from the trap to the ion detector, regardless of initial momentum. Each β-detector trigger starts a 3 μs timing window to measure the ^{21}Ne time-of-flight.

The $\beta - \nu$ correlation is inferred from the time-of-flight (TOF) distribution for coincident $\beta^+ - ^{21}$Ne events. Since the β momentum is directed at the β-detector, decays with aligned lepton momenta result in large nuclear recoils towards the ion detector. This results in short TOFs. When the neutrino momentum is opposite the β momentum, the average TOF is longer since the nuclear recoil is smaller and possibly even directed away from the MCP. The Monte Carlo simulation described in Chapter 5 is used to calculate the expected TOF spectrum for different values of $a_{\beta\nu}$. The calculated TOF spectra for ground-state $^{21}Ne^+$ recoils having propagated through the electric field used in the August 2001 run are shown in Figure 4.2. We show results for hypothetical ^{21}Na decays to the ground-state with $a_{\beta\nu} = 1$ and $a_{\beta\nu} = 0$. Ultimately, comparing data to simulation, we include decays to the excited-state, scattered events, and $\gamma - ^{21}$Ne coincidences.

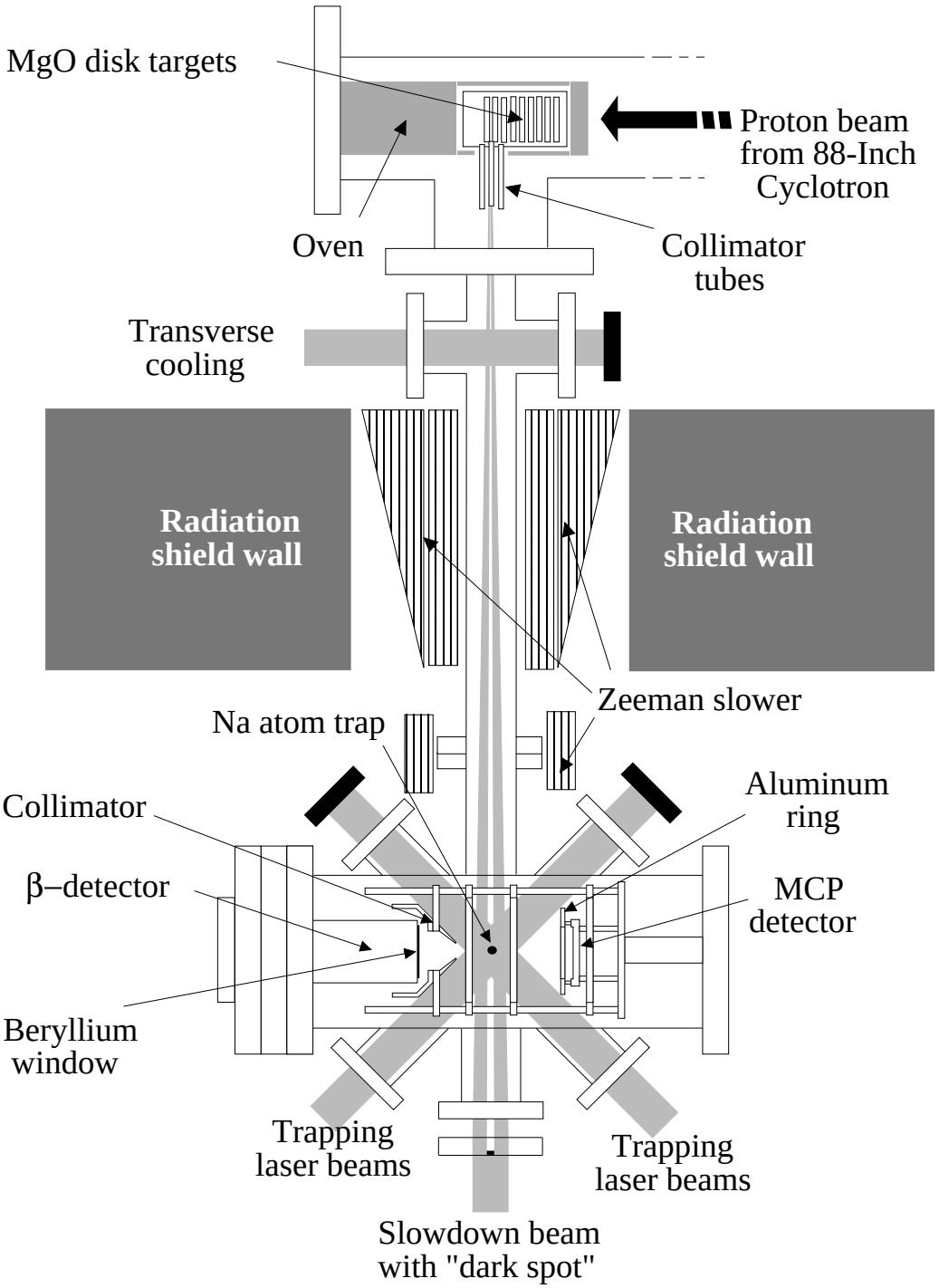

Figure 4.1: Experimental apparatus. Figure not drawn to scale.

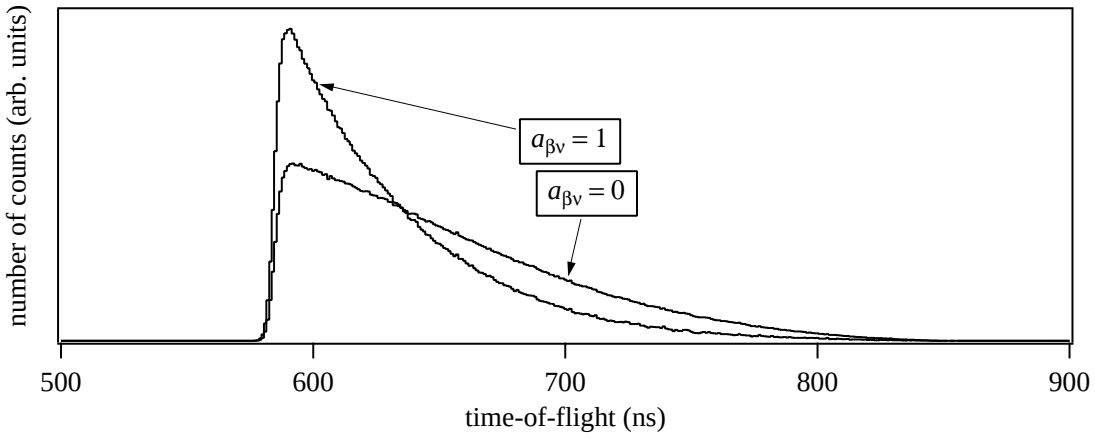

Figure 4.2: Monte Carlo simulation of the time-of-flight spectra for recoil $^{21}Ne^{+}(3/2^{+})$ given $a_{\beta\nu} = 1$ and $a_{\beta\nu} = 0$, emerging from a trap with a Gaussian density distribution with a FWHM of 0.75 mm in each dimension. Recoil order and order-α radiative corrections are included.

4.2 Early Measurement Attempts

Our early attempts at measuring the $\beta - \nu$ correlation suffered from lack of statistics and large systematic effects due to a simple detector and apparatus arrangement. The original apparatus is shown is Figure 4.3. A summary of all experimental runs and data accumulated is given in Table 4.1. These runs were crucial for uncovering and identifying backgrounds and systematic effects. The experiment was refined so that we could make a $\approx$1% measurement of $a_{\beta\nu}$. The ion and β-detector were upgraded and calibrated in detail, and the electrodes were remade so the electric field would be more reliably calculable. A collimator in front of the β-detector limited its field-of-view, suppressing the background from scattered β^{+}s. The charge-state distribution and $\beta - \nu$ correlation coefficient were determined by the recoil-ion data from the August 30, 2001 run only. In this section, we motivate the final experimental configuration by discussing the problems encountered.

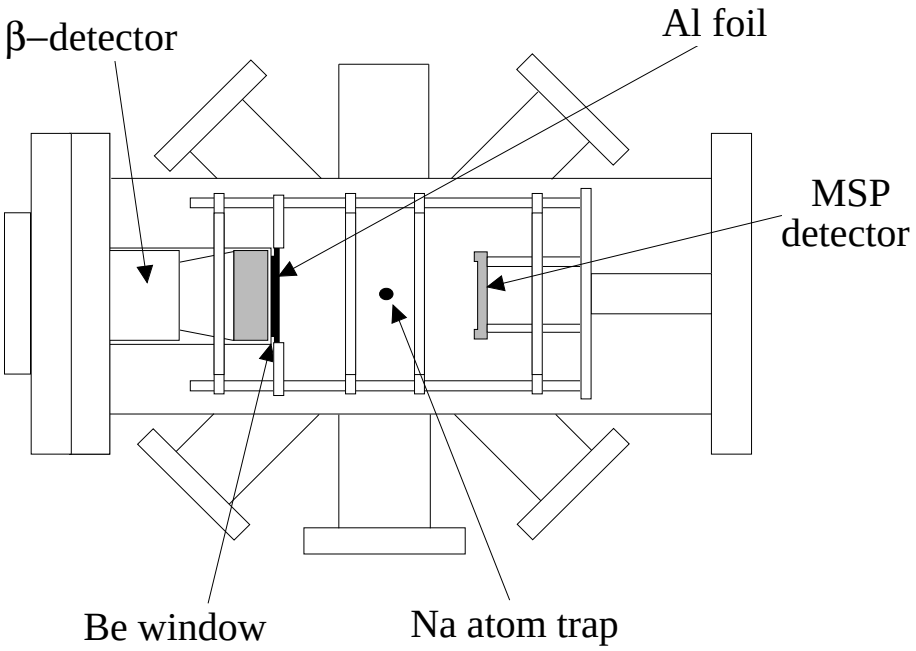

Figure 4.3: Original experimental apparatus. Figure not drawn to scale. The support rods were made of alumina. Separate voltage leads (not shown) were used for each of the electrodes. Charging of the alumina and the presence of these leads distorted the electric field.

Date	Ion detector	$\beta^+ - {}^{21}$Ne events	Description
Nov. 18, 1999	MSP	200	first run, crucible tubes misaligned
Dec. 10, 1999	MSP	2350	more statistics
Feb. 10, 2000	MSP	4575	more statistics
March 26, 2000	MSP with grid	5525	bias grid added
July 12, 2000	MSP with grid	93,100	trapping efficiency enhanced
Aug. 18, 2000	MSP, no grid	39,100	grid removed
Dec. 9, 2000	MCP, no grid	620,000	MCP installed
May 25, 2001	MCP, no grid	110,000	collimator and ΔE-E β-detector
Aug. 30, 2001	MCP, no grid	500,000	more statistics

Table 4.1: Summary of runs for $\beta - \nu$ correlation measurement.

4.2.1 Microsphere Plate Detector

The first ion detector we used was a double-thickness microsphere plate detector (MSP) on an E033 extended mount [86]. The active area diameter was 27 mm. The MSP is similar to the more common microchannel plate detector (MCP). The main difference is the electron multiplication occurs in tiny, tightly-packed, sintered glass beads rather than microchannels. The MSP was expected to have similar characteristics to a MCP, but can operate under lower vacuum conditions [87] and is structurally more rugged [88]. Unfortunately, its intrinsic detection efficiency, $\mathcal{E}_{MSP}$, is only ~24% for 10–40 keV $^{20}Ne^{+}$. $\mathcal{E}_{MSP}$ can be improved to ~42% with the use of an electron-repelling mesh in front of the MSP [89], but this smaller than the detection efficiency of an MCP operated without a mesh. Little was known about the energy or spatial dependence of $\mathcal{E}_{MSP}$. These dependences were tested during off-line tests described later this Chapter and by comparing the charge-state branching ratios of ^{21}Ne ions measured with the MSP and MCP.

The calibration of the MSP was a trial run for the off-line MCP calibration. We used a monoenergetic beam of $^{20}Ne^{+}$ with an impact area on the MSP of ~0.25 cm^2 that is described in detail later. The MSP was operated without a biasing grid at the maximal voltage of −3.5 kV across the plates, just as during the trapping runs. At this voltage, the average gain is $\sim 10^7$. We expected the gain would be uniform over the entire detector and would increase with particle impact energy. We were wrong on both accounts.

The response of different detector regions varied by a factor of two (see Figure 4.4). The gain increased away from the center (lack of range on the translation arm prevented response measurement accross the entire diameter). This output sag would be characteristic of gain reduction from extracted charge since the majority of recoil-ions from the trap impact near the MSP center. However, an effect of this magnitude would only occur after ≈0.03 C/cm^2 emerged from the MSP, requiring $>10^{10}$ ion events. This is three orders of magnitude more than observed. The energy dependence of the output was measured at the MSP center with monoenergetic $^{20}Ne^{+}$ beams between 6.2 and 11.2 keV. To our surprise, the gain was constant to ~5%. Results are shown in Figure 4.5 and compared to the MCP

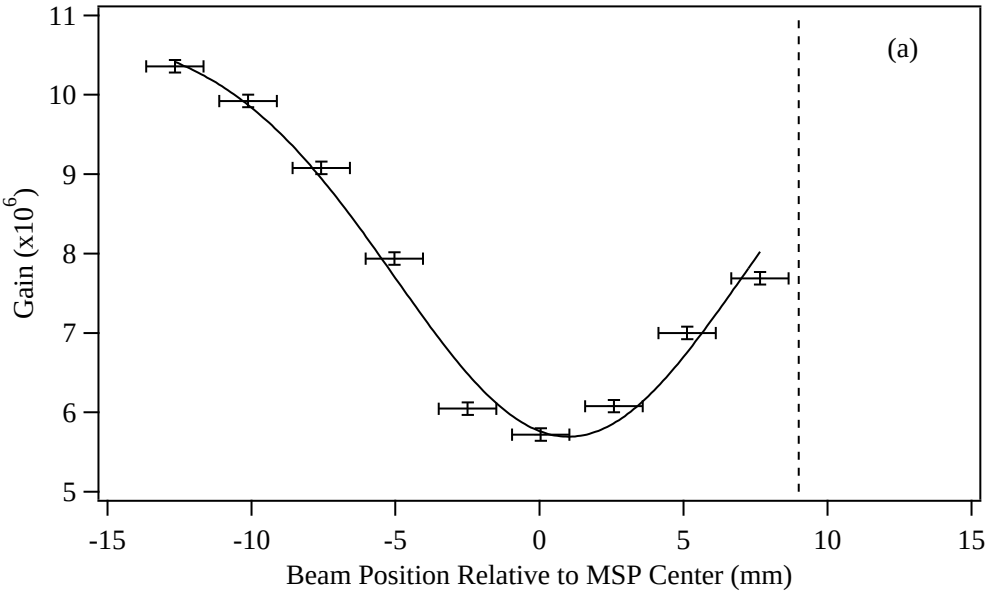

Figure 4.4: Gain of MSP along the diameter. The dashed line indicates the limit of the translation arm.

response.

It is not the absolute gain, but how that gain affects the detection efficiency that is of importance. Clearly, counts will be lost because they fall below the electronic threshold. By choosing an electronic threshold as low as permissable given the constraints of noise discrimination, this loss can be minimized, but not eliminated. However, the detection efficiency also depends on the fraction of events that give any output at all. Research has shown the maximum detection efficiency of a MCP (operated without a biasing grid) is approximately the open area ratio (OAR) of the microchannels. Since OARs are typically 60%, nearly 40% of the active area is unresponsive. In theory, the entire MSP surface could be active. This is unlikely given its detection efficiency for ions of only 24%. Although we did not independently verify the test beam intensity, we estimate it was stable to $\approx$5% for hours at a time because of the constancy of event rates. The event rate was constant to $\pm$10% across the MSP diameter, with variations possibly attributable to fluctuations in backgrounds.

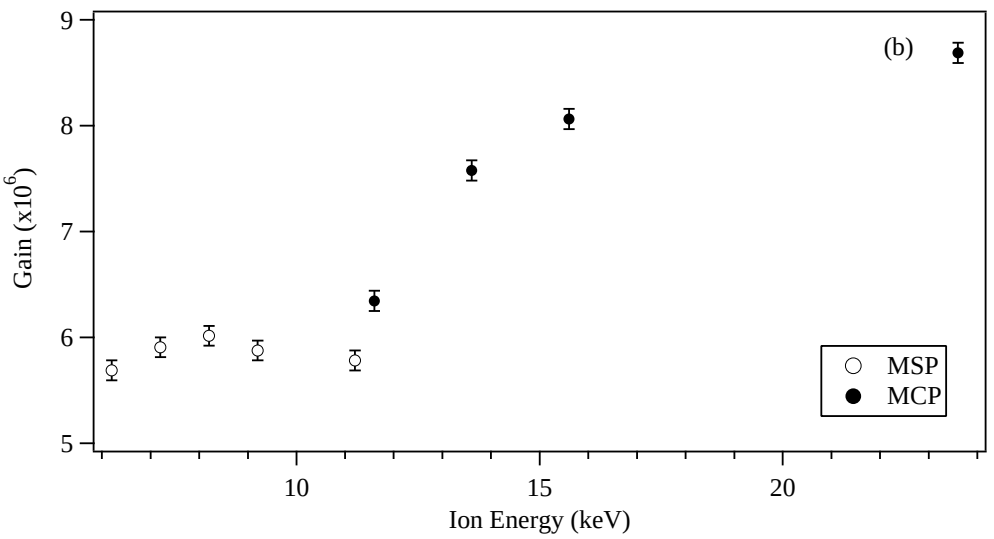

Figure 4.5: Gain at MSP center (and MCP for comparison) as a function of $^{20}Ne^{+}$ kinetic energy.

Although it is tempting to conclude that an equal gain implies an equal detection efficiency, empirical evidence suggests otherwise. By comparing the ^{21}Ne charge-state distributions measured with the MSP and MCP, we deduced the absolute detection efficiency for ions and low-energy neutrals. The MCP is known to have an absolute detection efficiency for >2 keV ions of ≈60% with energy dependence <2% (see later this chapter). Data collected in July 2000 (MSP with a bias grid) and August 2000 (MSP without a bias grid) are compared to the high precision charge-state distribution results from August 2001 (MCP without a bias grid). By comparing ratios for the different detectors, shown in Table 4.2, we find the MSP detection efficiency for ≈6 keV $^{21}Ne^{+}$ ions is smaller than for ≈12 keV $^{21}Ne^{+2}$ ions by 11±2% when operated without a grid and 24±2% when operated with a grid. The absolute MSP detection efficiency was determined by comparing the ion coincidence rate to the trap population and using the measured charge-state distribution (which assumed a MCP detection efficiency of 58±3%). The detection efficiencies are summarized in Table 4.3 for the MSP under a variety of operating conditions. When appropriate, $\mathcal{E}_{MSP}$ has been corrected for the 85% transparency of the grid and represents the detection efficiency

Detector	$^{21}Ne^{+}$	$^{21}Ne^{+2}$	$^{21}Ne^{+3}$
MCP	1	0.1673±0.001	0.0143±0.0003
MSP (without grid)	1	0.185±0.003	0.0158±0.0010
MSP (with grid)	1	0.205±0.002	0.0184±0.0007

Table 4.2: Ratio of ion charge-state counts relative to $^{21}Ne^{+}$ counts measured by the ion detectors. The MCP was operated at $-2\,kV$ and the MSP at $-3.5\,kV$. The electronic threshold is at 25 mV in each case.

MSP configuration	Voltage (kV)	0	+1	+2
With grid	−3.15	1.2±0.3%	21±4%	26±4%
With grid	−3.325	1.8±0.3%	31±5%	38±5%
With grid	−3.50	3.2±0.5%	36±5%	45±5%
With grid [89]	−3.50		∼42%	
Without grid	−3.50	2.2±0.4%	20±4%	22±4%
Without grid [89]	−3.50		∼24%	
MCP without grid	−2.0	6.1±0.8%	58.0±3%	58.5±3%

Table 4.3: Intrinsic detection efficiency for MSP under a variety of operating conditions for an electronic threshold of $-25\,mV$. Neutral detection efficiency quoted is average over energy spread that reach the detector.

for those ions reaching the detector surface. These detection efficiencies are in excellent agreement with the results of Ref. [89].

Despite the ×10 difference in detection efficiency between the multi-keV ions and 200 eV neutrals, the gains are nearly identical, regardless of whether a biasing grid was used. The pulse height spectra from August 18, 2000 are shown in Figure 4.6 for the ^{21}Ne data. The higher charge-state ions have smaller gains, most likely because they hit the MSP closer to the center. We obtained similar results with a biasing grid, consistent with the findings of Ref. [89] for MSPs and Ref. [90] for MCPs. We found no clear way to relate $\mathcal{E}_{MSP}$ to the gain. The MSP was replaced by a MCP in the fall of 2000 because of its larger detection efficiency and documented response.

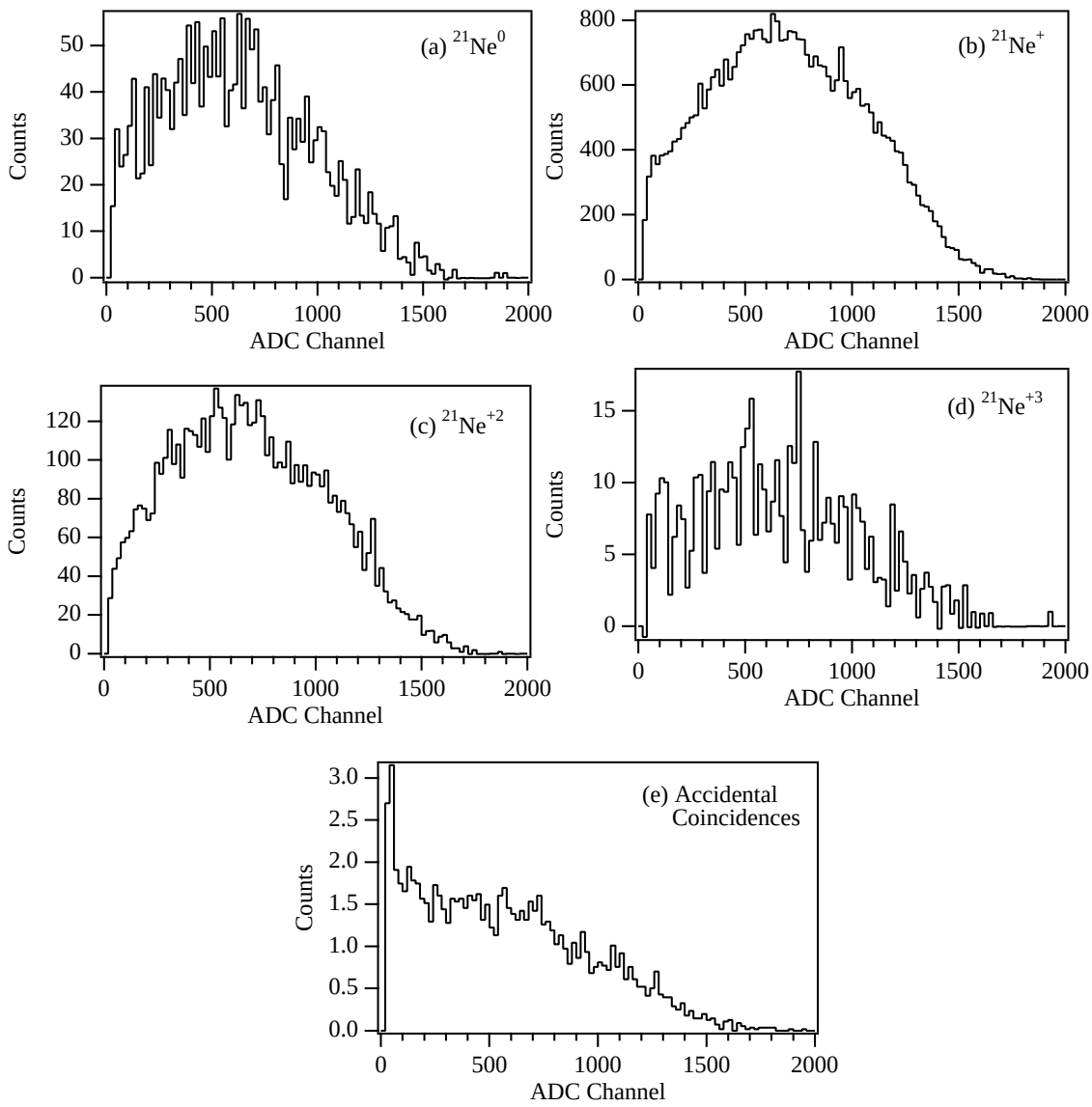

Figure 4.6: Pulse height spectra the MSP operated at $-3.5\,\mathrm{kV}$ without a grid for (a) $^{21}Ne^{0}$, (b) $^{21}Ne^{+}$, (c) $^{21}Ne^{+2}$, (d) $^{21}Ne^{+3}$, and (e) accidental coincidences. The accelerating potential is $6\,\mathrm{kV}$. The pulse heights are similar even though the impact energy varies from $0.2\,\mathrm{keV}$ to $18.2\,\mathrm{keV}$.

4.2.2 Thick Plastic Scintillator β-Detector

For the first seven runs, the β-detector active area was a 10 mm thick, 51 mm diameter cylinder of Bicron 404 fast plastic scintillator. The light output was quoted to be 68% of anthracene and the wavelength of maximum emission is 408 nm. The scintillator was optically coupled to a Hamamatsu R5924 2-Inch, head-on photomultiplier tube [91] capable of stable operation at magnetic fields up to 1 T. The bialkaline photocathode has a typical quantum efficiency of 22% at 390 nm.

The detector was placed as close to the trap to maximize the signal. At 64 mm from the trapped atoms, the detector subtended a solid angle of 4% of 4π. The time-of-flight distribution measured using this β-detector and the MSP is shown in Figure 4.7. The β-detector had a $\approx$10% detection efficiency for γ-rays and a line-of-sight to most of the chamber interior. Scattered β^+s and annihilation radiation lead to long tails on the TOF peaks because the ion recoil can be in any direction. Backscattering was difficult to model accurately and amounted to a correction of $+0.06\pm0.02$ to $a_{\beta\nu}$. The γ-ray events could be rejected by requiring >500 keV deposited in the β-detector. There was no simple way to eliminate contributions from β scattering without the addition of some type of collimation.

4.2.3 Electrode Backgrounds

Decays from untrapped ^{21}Na on the 30 μm thin, aluminum electrode in front of the β-detector resulted in a background at TOFs>1000 ns. These events are clearly visible in the December 2000 background runs shown in Figure 4.8. This background has no effect on the interpretation of the ion peaks, but complicates analysis of the neutrals. The neutral TOF peak is used primarily to determine the trap-to-MCP distance, which is important for determining the $\beta - \nu$ correlation.

The peak at $\approx$1200 ns is due to $^{21}Ne^+$ recoils that emerge from the electrode. A Monte Carlo simulation that assumes the recoils are distributed uniformly over the electode and lose 8 eV in the aluminum accounts for the shape and timing of the earlier background

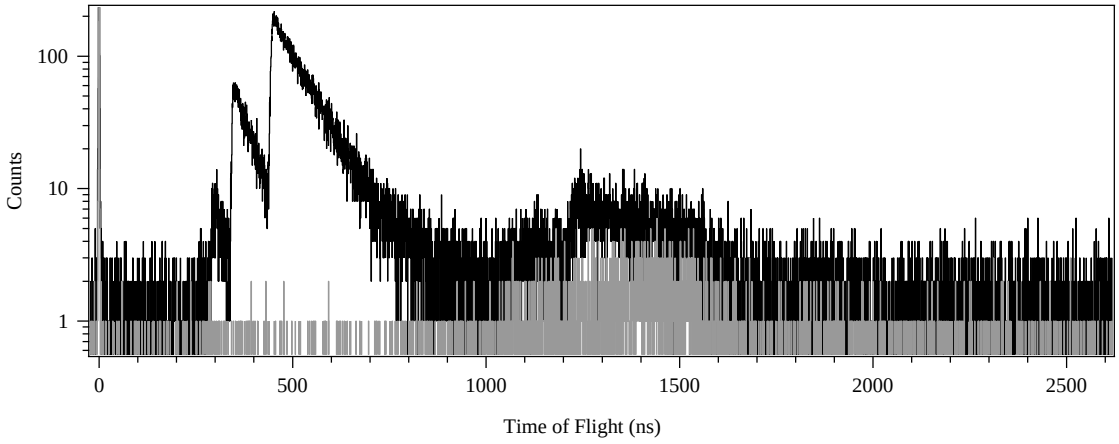

Figure 4.7: Recoil-ion time-of-flight from the August 18, 2000 Run. Data in black was collected with ≈100,000 atoms maintained in trap and data in gray was collected with vertical trapping beams blocked so no atoms were trapped.

peak. Monte Carlo simulations indicate the β^+ and recoil-ion had ≈50% solid angles for the β-detector and MCP, respectively.

The later peak is $^{27}Al^+$ knocked from the electrode with an energy spread of 0–65 eV following ^{21}Na β decay. At ≈2200 ns, there may be evidence of $^{56}Fe^+$ ions knocked out of the stainless steel electrode that holds the aluminum electrode. We would expect this peak to be 10% of the $^{27}Al^+$ peak because of a smaller surface area and β-detector solid angle. No evidence of any ions emerging from the electrode with a charge $>+1$ was found. Similar effects have been observed following the electron capture decay of ^{37}Ar from a surface [92]. During this run, we estimate an average of ∼750 atoms/cm^2 of ^{21}Na covered this electrode. Assuming a uniform coating over the entire chamber, a population of $\sim 1\times10^6$ atoms is maintained on the chamber walls. This is consistent with observed β-detector rates.

As will be discussed in Section 4.5, the electrode in front of the β-detector was replaced with a heavy-metal collimator, thick enough to stop all β^+s from the decay. This eliminated the noise discussed here since ^{21}Na activity on the outer surface is not detected by the β-detector. More importantly, the majority of coincidences from scattered β^+s are

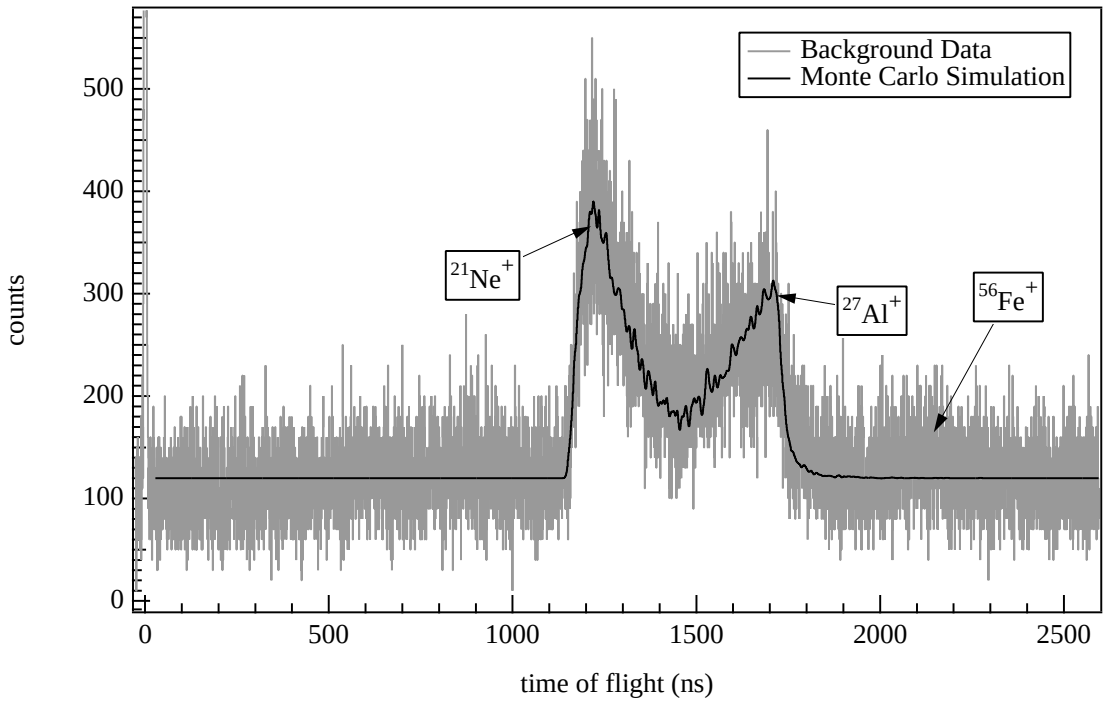

Figure 4.8: Background data from December 9th, 2000. The Monte Carlo simulation describes the data by assuming $^{21}Ne^{+}$ recoils emerge from the aluminum having lost 8 eV of kinetic energy and $^{27}Al^{+}$ is knocked from the electrode with an energy spread of 0–65 eV. At ≈2200 ns, there is evidence of a small peak due to $^{56}Fe^{+}$ ions knocked from the stainless steel portion of the electrode that holds the aluminum in place.

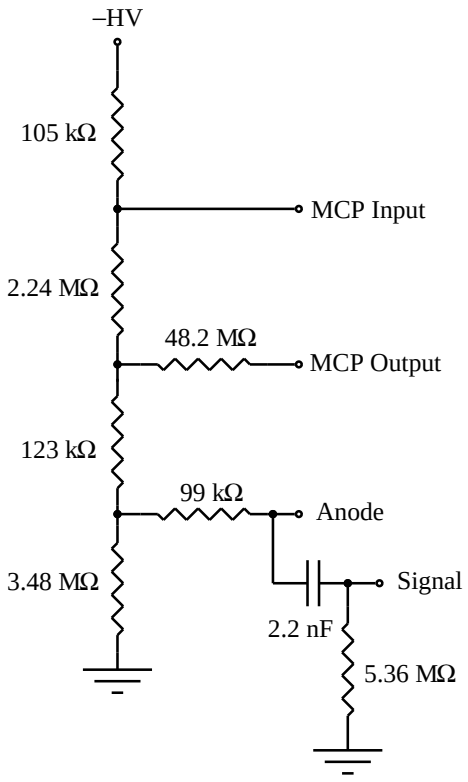

Figure 4.9: The resistive biasing network used for the MCP. The output is capacitively coupled as shown.

eliminated by restricting the line-of-sight of the β-detector.

4.3 Microchannel Plate Detector

A Burle Long-Life, Detection Quality, Chevron MCP with a "Quality Area" of 40 mm in diameter (MCP 40/6/12 D 60:1 MS CsI) [93] replaced the MSP. The channels have a 12° bias angle and a length-to-diameter ratio of 60:1. They are coated with a thin layer of CsI, enhancing detection efficiency for ultraviolet photons from 20 to 200 nm. A metal anode collected the amplified charge. Even with a bias of -2 kV, the largest output pulses are 50 mV. We amplify the signal with an Ortec FTA 420 $\times$200 fast amplifier. The MCP input floated at -5 kV to capture the ions. The voltages were applied with a resistive network and the output was capacitively coupled with the circuit in Figure 4.9.

The MCP detection efficiency, $\mathcal{E}_{MCP}$, must be understood to interpret the TOF distribution. Impact energy, angle, and position are potentially influential. Any rate dependence must be accounted for. On the other hand, the absolute detection efficiency is only important for the charge-state probabilities following β^+ decay. For $\beta - \nu$ correlation measurements, the exact value is unimportant.

During the August 2001 run, the electric field focused >99.5% of $^{21}Ne^+$ (in coincidence with detected β^+) and all higher charge-states onto the 44 mm diameter MCP active area. The active area diameter is 4 mm larger than the "Quality Area" diameter. We checked the detection efficiency outside of the "Quality Area" because this region is not polished as finely for uniform performance. Non-uniformity in $\mathcal{E}_{MCP}$ distorts the TOF spectrum and lead to a systematic error.

We conducted an off-line calibration of the MCP detector using an electron cyclotron resonance ion source (IRIS ECR) [94]. A monoenergetic $^{20}Ne^+$ beam tunable between 10–20 keV was used. Since the MCP output sags at rates higher than 10^3–10^4 Hz/cm^2, the ion current was reduced to femtoamps by defocusing and collimating. The ion beam was defined using a 30 μm thick aluminum collimator with a ≈3 mm diameter opening approximately 10 mm in front of the MCP. Although we did not obtain absolute efficiencies, we measured accurate relative efficiencies needed for interpretting the $\beta - \nu$ correlation data. The rest of this section is devoted to MCP calibrations.

4.3.1 Absolute Detection Efficiency

There are several reported measurements of the absolute detection efficiencies of MCPs as a function of ion species and kinetic energy (see Ref. [95] and references therein). They demonstrate that for ions with energies ≥2 keV, $\mathcal{E}_{MCP}$ shows little variation and approaches the open area ratio of ≈60% regarless of ion species [96] or charge-state [97]. In these studies, few output pulses were below electronic thresholds. In general, absolute detection efficiencies increase to 85% with a negatively biased transmission grid in front of the MCP [98]. In this configuration, secondary electrons that otherwise would escape are

redirected back to the MCP. It is possible for $\mathcal{E}_{MCP}$ to rise above the open area ratio.

For the $\beta - \nu$ correlation measurement, we considered using a grid, but decided against it. Even for the 95% transmission grids, some ions would interact with the grid. The TOFs for ions that strike the grid or approach it with a small impact parameter would be difficult to model with precision, leading to systematic uncertainty.

4.3.2 Positional Dependence

The MCP was attached to an adjustable mount that moved in the plane perpendicular to the test ion beam. By moving the MCP relative to a fixed collimator aperture, we obtained the detector response shown in Figure 4.10. After the August 2001 run, we noticed a crack in the CsI coating and were concerned about $\mathcal{E}_{MCP}$ in that vicinity. Surprisingly, the region near the crack gave the highest average pulse heights. The output decreased towards the edge of the detector, and was 60% smaller outside the "Quality Area" than at the center.

This was expected from analysis of recoil-ion data which had prompted this detailed, position-dependent calibration. We noticed the pulse heights from longer TOF recoil-ion events (which would hit at larger radii) were smaller. Unfortunately, the lack of a one-to-one correspondence between TOF and position did not allow us to make corrections directly from the data. Such corrections would be possible with the position-sensitive detector that will be incorporated in future experiments.

We deduced $\mathcal{E}_{MCP}$ from the peak of the PHD by estimating the fraction of events that fall under the electronic threshold and multiplying by the open area ratio (60%). We modeled the MCP response to multi-keV ions with the function

$$P(x) = \frac{N}{1+A}\left(\frac{1}{\sqrt{2\pi}\sigma_0}e^{-\frac{(x-x_0)^2}{2\sigma_0^2}} + \frac{A}{2}\mathrm{erf}\left(\frac{x-x_0}{\sqrt{2}\sigma_0}\right)\right) \tag{4.1}$$

consisting of a Gaussian distribution with peak x_0 and width σ_0 a step function below the peak with area A. The overall normalization, N, does not effect the resulting detection efficiency. We found empirically that σ_0 is proportional to x_0 and A inversely proportional

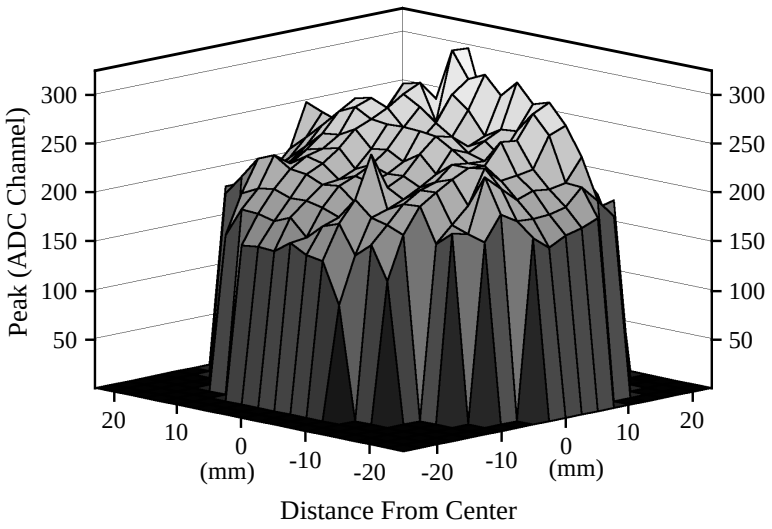

Figure 4.10: Two-dimensional distribution of MCP peak pulse heights for a 10 keV $^{20}Ne^{+}$ ion test beam. At the detector center (edge), 97% (94%) of pulses are larger than electronic threshold. The detection efficiency drops rapidly to zero as the beam moves off the active area.

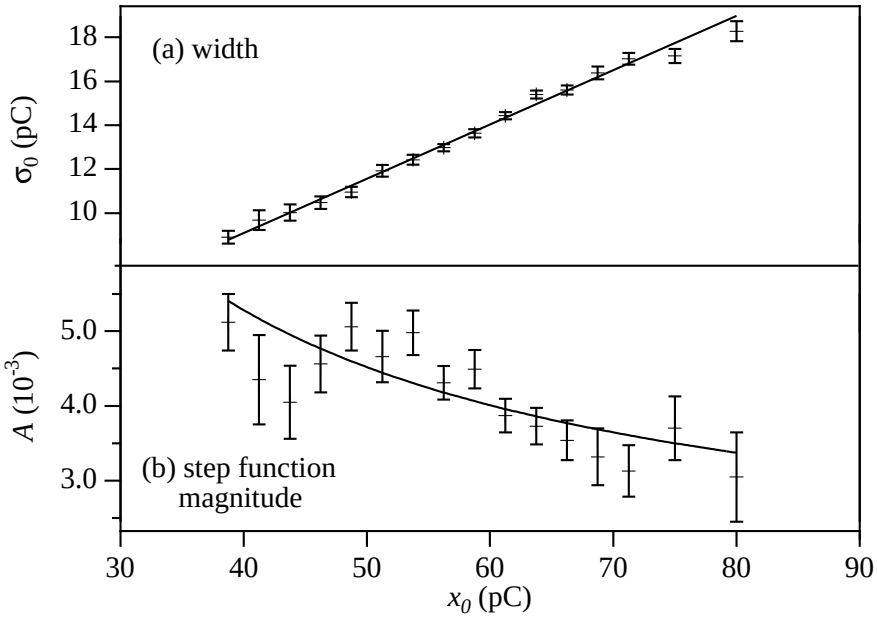

Figure 4.11: Dependence of MCP (a) output width, (b) step function magnitude on peak pulse height.

to x_0 with relationships

$$\begin{aligned} \sigma_0 &= (-0.8 \pm 0.4) + (0.247 \pm 0.007) \times x_0 \\ A &= ((1.5 \pm 0.5) + (153 \pm 26)) \times x_0^{-1}) \times 10^{-3} \end{aligned} \tag{4.2}$$

determined from the data in Figure 4.11. In this model, $\mathcal{E}_{MCP}$ was estimated from x_0. Two sample spectra are shown in Figure 4.12 for ≈2000 Hz of 10 keV $^{20}Ne^{+}$ ions at different regions of the MCP detector. Depending on position, 94 to 97% of the PHD was larger than the 25 mV electronic threshold. These results suggest that at large x_0, $\mathcal{E}_{MCP} \propto x_0$. Unfortunately, the PHD for higher ion charge-states could not be obtained using the IRIS ECR test beam because of poor signal-to-noise. Instead, we used singly charged ions accelerated to twice the energy, since $\mathcal{E}_{MCP}$ is independent of charge-state for identical isotope and energy [97].

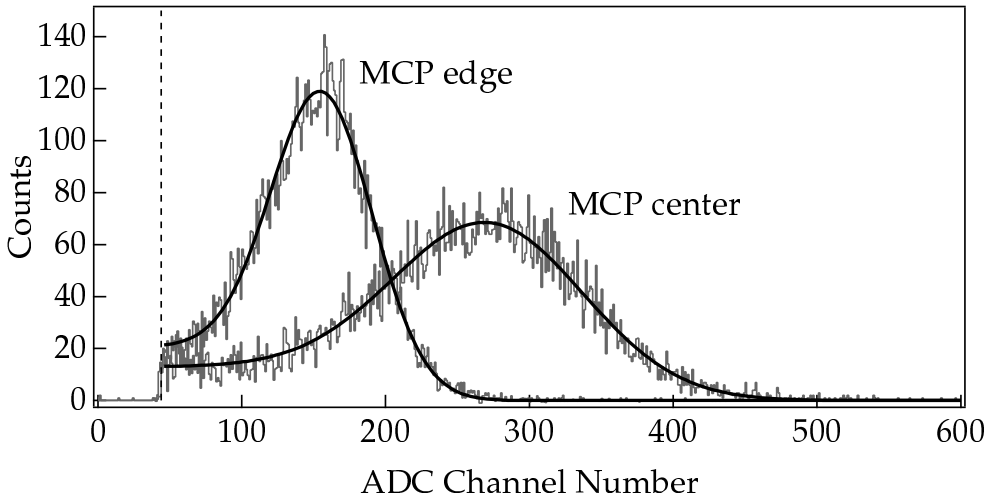

Figure 4.12: Representative MCP pulse height distributions for 10 keV $^{20}Ne^{+}$ ions impacting the center and edge of the active area. The smooth curves are the empirical fit to the function $P(x)$ and the dashed vertical line shows the electronic threshold.

4.3.3 Rate Dependence

The MCP rate dependence was tested by adjusting an upstream collimator to vary the ion current delivered by the IRIS ECR to the MCP. Only at rates above 2000 Hz (for a beam that covered $\sim$5 mm^2) did the gain begin to sag appreciably. Even for traps of 500,000 atoms, ion flux is orders of magnitude smaller. Recoil-ion PHDs indicate the average MCP gain sags by 9$\pm$3% between trap populations of 100,000 and 500,000 atoms, leading to an average decrease in $\mathcal{E}_{MCP}$ of only 0.4%.

Studies have shown that MCP gain is reduced within $\sim$1 mm of a microchannel recovering from electron multiplication [99], and recharge rates can be of order milliseconds [100]. This decrease in gain is believed to arise from the electric field distortion in the region of the active channel [101]. Since the majority of recoil-ions strike near the center of the MCP, we expect the gain to be more severely affected near the center than at the edges. By assuming the gain reduction is proportional to the ion density, we estimate the correction to $a_{\beta\nu}$ is 0.0017$\pm$0.0006 at the largest traps.

Since the MCP voltages in large part define the electric field, any transient voltage changes (of duration $>1\,\mu$s and magnitude $>100\,$V) could impact ion trajectories. We looked for rate dependence in the high voltage at the MCP input and output connections in Figure 4.9 using a Tektronix P6015 HV Probe capable of measuring up to 10 kV at AC. The voltages remained constant to within 1 V, even with rates as high as 10 kHz caused by an ion gauge filament inside the trap chamber. We see no reason to suspect the electric field is affected by MCP voltage changes.

4.3.4 Energy Response

In the data set from August 2001, the recoil $^{21}Ne^{+}$ energy spread is 9.0 keV to 9.3 keV. Assuming $\mathcal{E}_{MCP}$ changes at the same rate from 9.0 to 9.3 keV as it does in previous work with H^{+}, He^{+}, and O^{+} [102] from 3.0 to 5.0 keV, the change in detection efficiency should be 0.2%. However, the detection efficiency changes less at high energies so the difference should be less at 9 keV.

We measured the variation in output with monoenergetic ions of energies between 11.6 and 23.6 keV. The results, in Figure 4.5, must be extrapolated from 11.6 keV to 9.0 keV, but assuming the output changes at about the same rate between 11.6 and 13.6 keV, we expect gain change of 4%. Understanding the precise energy dependence is not necessary because the correction is only 0.0002 ± 0.0001 to $a_{\beta\nu}$.

4.3.5 Angle of Impact

The response of a MCP is known to be dependent strongly on incident angle, but particles with angles smaller than 5° from the normal are detected with nearly constant probability [102]. A Monte Carlo simulation indicates all recoil-ions strike the MCP with angles below 2°, eliminating any angle-dependent variation of $\mathcal{E}_{MCP}$. Nevertheless, $^{21}Ne^{0}$ have incident angles as large as 15°, so the detection efficiency is expected to vary. The $^{21}Ne^{0}$ recoils are not used in the analysis of the $\beta-\nu$ correlation.

4.4 β-Detector

4.4.1 Design of the β-Detector Telescope

Significant improvements in β detection were required to realize a $\approx$1% measurement of the $\beta - \nu$ correlation. We used a β-detector telescope to reject annihilation γ-ray induced signals. The detector is shown in Figure 4.13. A 1 mm thick, Eljen EJ-204 fast plastic scintillator (ΔE) with a radius of 17.72$\pm$0.06 mm greatly reduced the γ-ray detection efficiency, while a 15 mm thick Eljen EJ-204 fast scintillator (E) stops the β^+s. The edge of the ΔE scintillator is beveled at 11° to match the angle of incoming βs from the trap. The effective nuclear charge, $\langle Z \rangle \approx 3.5$, of plastic minimizes β^+ backscatter. A cup-shaped, acrylic light guide transports light from the scintillator to the photomultiplier tube. At 15 mm thick, the E scintillator stops all β^+s from ^{21}Na decay. The 22.5 mm radius of the E scintillator minimizes the effects of angular straggling through the ΔE scintillator. Three layers of reflector paint on the sides of the E scintillator and the entire acrylic light guide increase the diffuse reflection at the surface, increasing the light yield at the PMT. The only dead layer between the two scintillators is a piece of 7.6 μm thick aluminized mylar. The mylar lets <0.01% of the light through, optically isolating the two detectors.

Since the β-detector experiences a magnetic field of $\approx$80 Gauss, the photomultiplier tubes are capable of stable operation in magnetic fields of up to 10,000 Gauss. A Hamamatsu R5924 51 mm diameter head-on PMT was used for the ΔE and a Hamamatsu R5946 38 mm diameter head-on PMT was used for the E detector. Applied voltages of were -1900 V for the ΔE and -1650 V for the E photomultiplier tube were sufficent to discriminate signals from tube noise. These voltages were used during data collection and calibrations.

At 91.9$\pm$1.0 mm from the trap, the β-detector subtends a solid angle of 0.92$\pm$0.02% of 4π. A 12.4 cm diameter stainless steel sleeve with a 0.127 mm thick beryllium window separates the detector from the UHV. The detector is centered inside the sleeve by an acrylic spacer and a 1 mm thick heavy metal ring. The ring opening has a diameter of 17.7 mm and exposes only the ΔE scintillator.

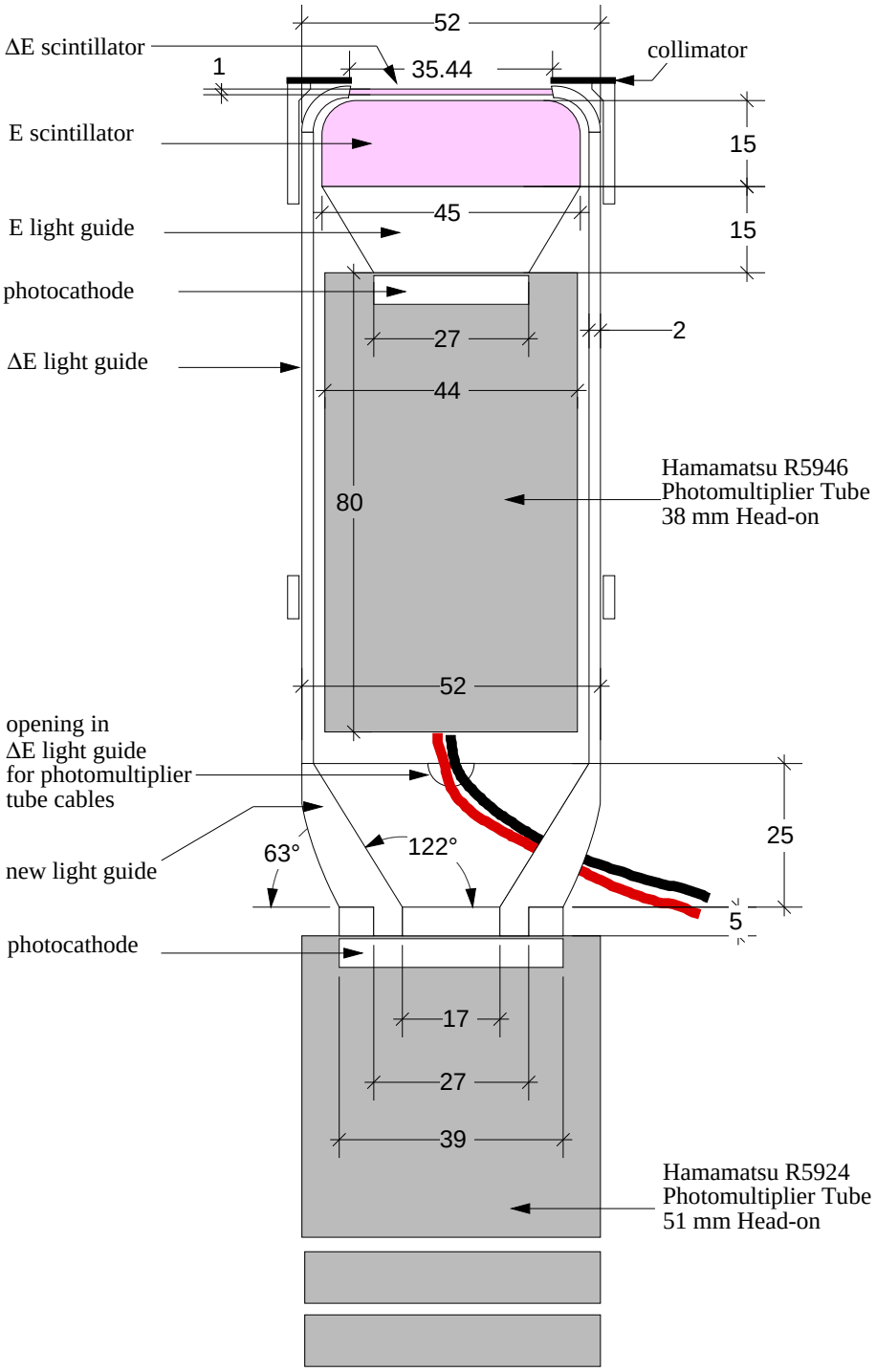

Figure 4.13: Plastic scintillator ΔE-E β-detector.

Unfortunately, a low hanging support bracket for the trapping chamber ion pump prevents direct access to the sleeve for the assembled detector. The detector must be inserted in two parts, optically coupled with optical grease, and mechanically held together. The end of the ΔE light guide fit into a matched slot in the acrylic glued to the front face of the ΔE photomultiplier tube. The tightness of the fit holds the joint together. The off-line calibration of the ΔE detector is compared to the energy deposited in the ΔE scintillator for high energy β^+s from trapped ^{21}Na decay. This is important because, as mentioned earlier, the β-detector is reassembled to collect recoil-ion data. The light collection efficiency in the ΔE detector could depend on the optical connection, but comparisons of minimum-ionizing peaks from ^{21}Na β^+s and ^{207}Bi conversion electrons shows the change is $\lesssim$1%.

The trigger condition considers a hit in either detector to be valid. The electrodes were redesigned to incorporate a conical, heavy metal collimator in front of the β-detector. This collimator restricts the β-detector's field-of-view to a cone defined by the atom trap and MCP, minimizing backscattered coincidences from all surfaces except for the MCP. These backscatter events give rise to a small and calculable correction. The following sections describe the β-detector in more detail.

4.4.2 Calibration

The energy deposited in the detector is determined from the light output of the two scintillators. Each detector was independently calibrated using radioactive sources. The energy loss in the beryllium window was taken into account by a Monte Carlo calculation and is crucial for determining the detection efficiency for the lowest energy β^+s. In the next sections, the determination of the response of the β-detector is described.

In addition to the detector response to β^+, the response to 511 keV annihilation radiation is important. Since few of these γ-rays will deposit energy above the Compton edge at 341 keV, an energy threshold of 400 keV effectively eliminates γ-ray contributions. However, $\approx$13% of the β spectrum is below 400 keV and the energy deposited in the detector is often split between the ΔE and E scintillators. Calibrating each detector and

understanding the energy division to the desired precision for the $\beta - \nu$ correlation measurement is challenging. To mitigate these issues, we accepted events depositing >50 keV. Although this made the measurement prone to γ-ray backgrounds, it was less sensitive to the calibration. The E detector calibration uncertainties had little influence on the final result.

In the ΔE detector, γ-ray interactions necessitate a correction of $\approx$0.01 to the $\beta - \nu$ correlation. By selecting events that deposit energy in the E but not the ΔE detector, $\gamma - ^{21}$Ne coincidences were isolated. Scaling by the relative γ-ray detection efficiencies of the two detectors gives an estimate to the background. At energies below $\sim$400 keV, the energy loss and straggling through the Be window becomes significant. Ion trajectories from decays with low β energy reach the edge of the MCP, where the detection efficiency is smaller.

4.4.3 ΔE Detector

The ΔE detector was calibrated with a 5 μCi ^{113}Sn sealed source. The conversion electrons with energies of 363.8 keV (28.4%), 387.5 keV (5.67%), and 390.9 keV (1.11%) are stopped in the ΔE detector. The spectrum for ^{113}Sn at the center of the detector is shown in Figure 4.14.

After the recoil-ion data was collected and the ΔE light guide redesigned to improve light collection efficiency, we discovered a radial dependence in the ΔE detector output. We calibrated the detector as a function of position using a 0.8 mm thick aluminum plate with a 5 mm diameter hole to limit the area exposed to radiation. The response was measured by keeping the source at a distance of 5.0$\pm$0.2 mm and moving the ΔE detector behind the plate.

At the center of the detector, the conversion between ADC channels and energy, $\mathcal{S}_{\Delta E}$, was 0.493$\pm$0.025 keV/channel, from a Gaussian fit to the high energy side of the peak, taking the conversion electron branching ratios into account. The energy resolution, $\mathcal{R}_{\Delta E}$=(1.86$\pm$0.09)$\times\sqrt{E_{\Delta E}}$ [keV] assuming it is proportional to the square root of the energy, $E_{\Delta E}$, deposited in the ΔE scintillator. The low-energy tail results predominantly from

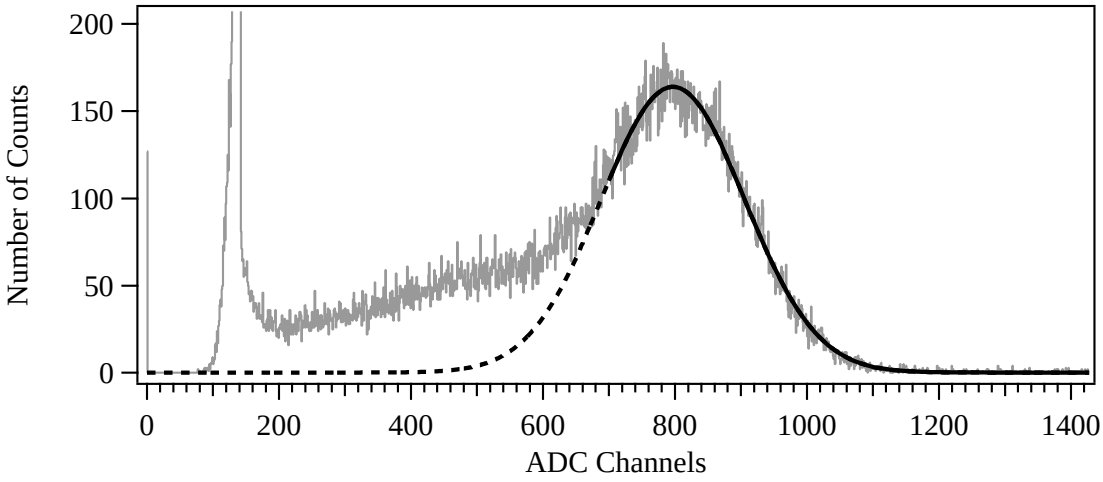

Figure 4.14: Response of the center of the ΔE detector to ^{113}Sn. The peak has been fit for channels >685 given the known conversion electron energies and branching ratios.

Compton scattering of the 391.7 keV γ-ray and scattering of conversion electrons from the environment.

After the August 31, 2001 run, the light guide for the ΔE detector was remade to adiabatically pipe light to the photomultiplier tube. The ^{113}Sn calibrations were done with the altered light guide after the run. The light collection efficiency was 27±4% higher with the altered light guide. The ΔE calibration used to interpret the recoil-ion data (at the detector center) was

$$\begin{aligned} \mathcal{S}_{\Delta E} &= (0.626 \pm 0.038)\,\mathrm{keV/channel} \\ \mathcal{R}_{\Delta E} &= (2.10 \pm 0.11) \times \sqrt{E_{\Delta E}[\mathrm{keV}]}. \end{aligned} \tag{4.3}$$

From the energy resolution we determine the photon collection efficiency. In Eljen EJ-204 fast plastic scintillator, a 380 keV conversion electron should generate 3800 photons of wavelength ≈415 nm. The peak width, σ, is 10% of the peak value, so the number of photoelectrons, N_{pe}, collected is 100 assuming $\sigma = \frac{1}{\sqrt{N_{pe}}}$. The typical cathode quantum efficiency is 23% for the R5924 at 415 nm. We estimate only 12.5% of the scintillation light is collected. However, only 28% can be collected by total internal reflection

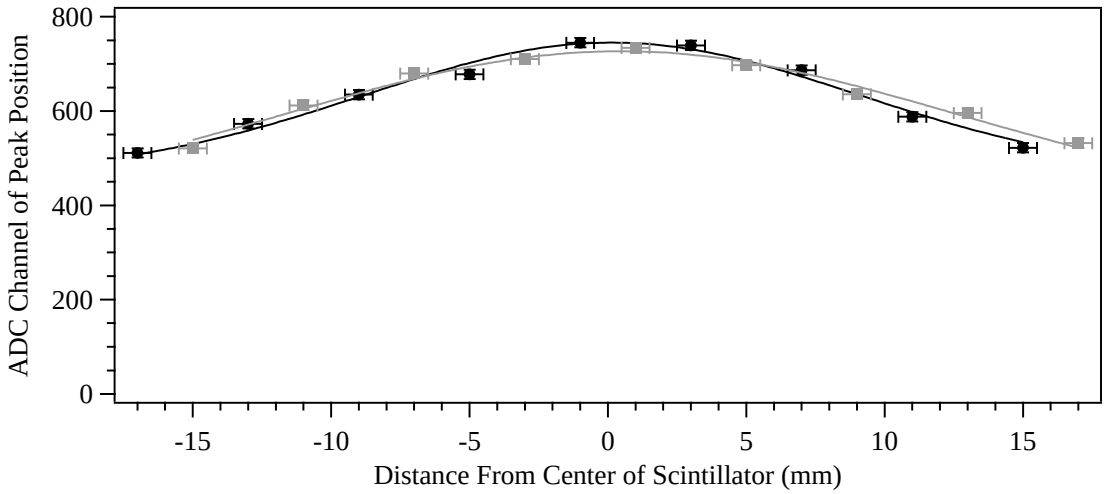

Figure 4.15: Position-dependence of the ΔE signal. The squares and circles represent two perpendicular passes across the face of the detector. The data have been fit with Gaussians to guide the eye.

for acrylic with an index of refraction of 1.49. Therefore, we collect 42% of the light that is totally internally reflected.

The radial dependence of the light output in Figure 4.15 was determined from the peak of the conversion electron line as a function of position. No satisfactory explanation was found for this trend, although it could be from light loss in the acrylic or at the acrylic/air interface. Light generated at the center of the scintillator disk travels straight down the light guide, while light originating from the edge follow a longer, spiral path. The average path-length is substantially less for light from the center of the scintillator. However, this explanation requires the light loss in the acrylic to be comparable to that of quoted for scintillator by the emiT collaboration [103]. Light loss of this magnitude is consistent with collection of only 42% of the totally internally reflected scintillation light. Regardless of the origin of this effect, it must be included in the analysis to interpret the data. Fortunately, a low energy threshold insures that the analysis is insensitive to β energy uncertainties.

The calibration is checked against the energy deposited in the ΔE scintillator for high energy β^+s from trapped ^{21}Na decay. The minimum ionizing peak in the ΔE for

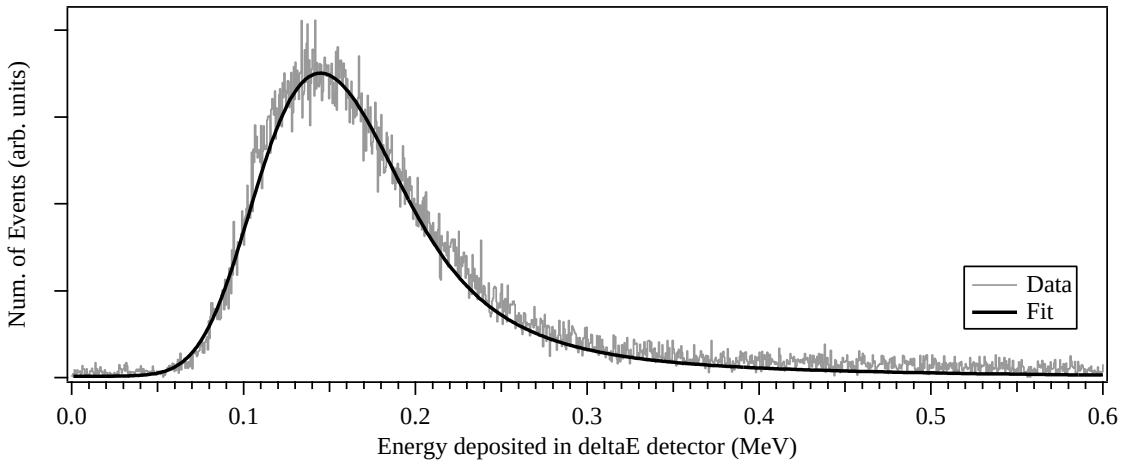

Figure 4.16: Output of ΔE detector when total energy deposited in β-detector is between 950–1050 keV. The predicted response is calculated by applying the off-line calibration to the EGSnrc calculation of energy deposition.

events with total energy 950 keV< E_β <1050 keV is shown in Figure 4.16 along with the expected response calculated using EGSnrc convoluted by the detector response from sealed source calibrations. The width of the minimum ionizing peak is dominated by the radial dependence of the light collection efficiency.

At energies as low as 50 keV, we account for the decrease in specific fluorescence, $\frac{dS}{dx}$ as the specific energy loss, $\frac{dE_\beta}{dx}$ increased. The relationship:

$$\frac{dS}{dx} = \frac{A\frac{dE_\beta}{dx}}{1 + kB\frac{dE_\beta}{dx}} \tag{4.4}$$

is known as Birks' Law [104]. The constant kB accounts for the high density of quenching that occurs when specific energy loss becauses large and A is the proportionality constant between energy and fluorescence. Assuming the experimental value $kB = 0.0066\,\mathrm{g\,MeV^{-2}\,cm^{-2}}$ for plastic scintillator [105], we calculate an 8% decrease in fluorescence for a 50 keV β and the threshold is adjusted accordingly.

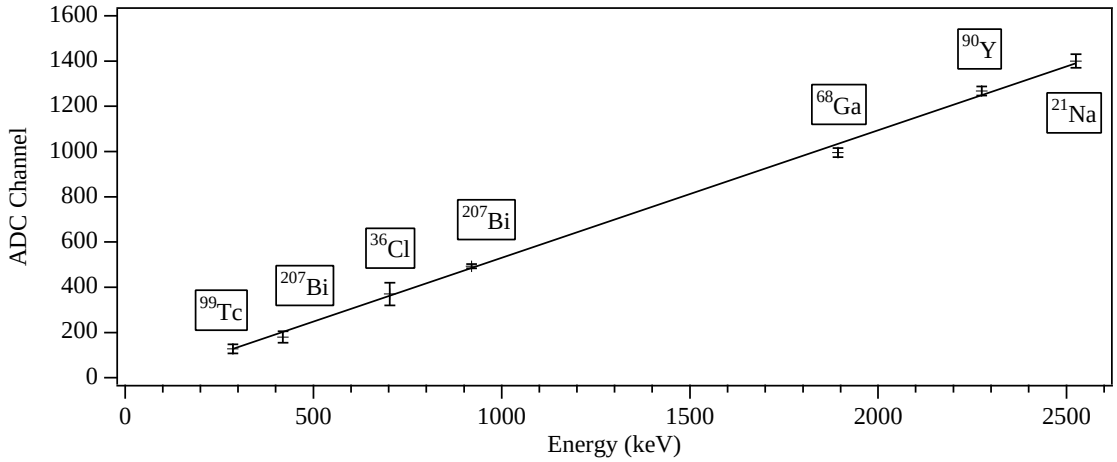

Figure 4.17: E detector response for calibration sources. Notice the agreement between the detector calibration and the E_0 point for ^{21}Na, given the ΔE calibration discussed earlier.

4.4.4 E Detector

The E Detector energy scale, $\mathcal{S}_{\rm E}$, was determined from ^{207}Bi conversion electron peaks and the endpoints of a variety of β emitters. Only the 976 keV conversion electron peak of ^{207}Bi could be obtained with good precision. The 482 keV peak had poor signal-to-noise and endpoint energy measurements are sensitive to detector response. Figure 4.17 shows the result of the calibration, with corrections for energy loss in air and source casings. The full calibration of the detector was checked by the consistency of the β spectrum of from ^{21}Na decays.

The energy resolution, $\mathcal{R}_{\rm E}$, was primarily determined by the higher energy edge of the 1 MeV ^{207}Bi conversion electron line. Since there are few conversion electrons or γ-rays above this energy, the high energy side of the response is primarily from detector resolution. We corrected for the 1048 keV and 1060 keV conversion electron branch contributions.

The E detector calibration was

$$\begin{aligned} \mathcal{S}_{\rm E} &= (1.72 \pm 0.03)\,{\rm keV/channel} \\ \mathcal{R}_{\rm E} &= (1.88 \pm 0.07) \times \sqrt{E_{\rm E}[{\rm keV}]} \end{aligned} \tag{4.5}$$

assuming $\mathcal{R}_{\rm E}$ is proportional to the square root of the energy, $E_{\rm E}$, deposited in the E

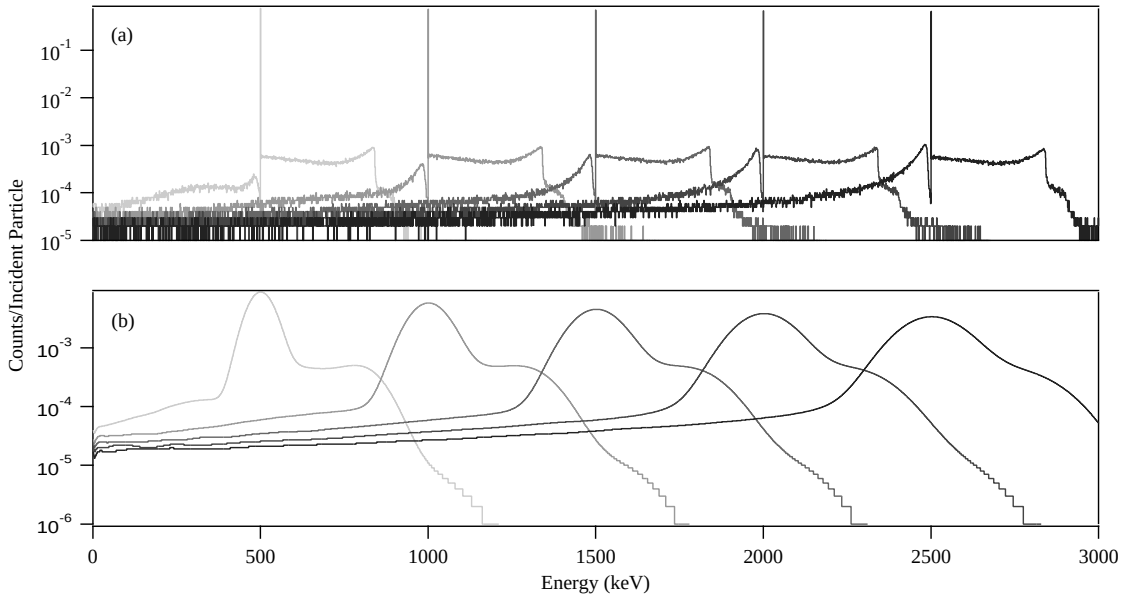

Figure 4.18: Calculated β-detector telescope response to β^+s of energy 500, 1000, 1500, 2000, and 2500 keV. (a) Energy deposition in scintillator and (b) detector response from off-line calibrations discussed in text.

scintillator.

The β-detector resolution function is not just a simple Gaussian expected from photon statistics. Figure 4.18 (a) illustrates ideal detector response for monoenergetic β^+ beams of energy 500, 1000, 1500, 2000, and 2500 keV simulated using EGSnrc. The narrow peaks correspond to full β energy deposition. Compton scattering of annihilation radiation produce Compton contina that extend $\approx$340 keV above the β energy. Backscattering and bremsstrahlung result in the low-energy tails. Figure 4.18 (b) shows the detector response at these same energies after applying the measured, energy-dependent convolution to the detector response in (a).

We verified that the size of the Compton shoulder and low-energy tail predicted by EGSnrc agreed with observed detector response. The detection efficiency for 511 keV γ-rays was measured using a 10 μCi ^{68}Ga source. The source was placed inside a 2 cm cube of acrylic to stop the βs. The energy spectrum shown in Figure 4.19 was compared

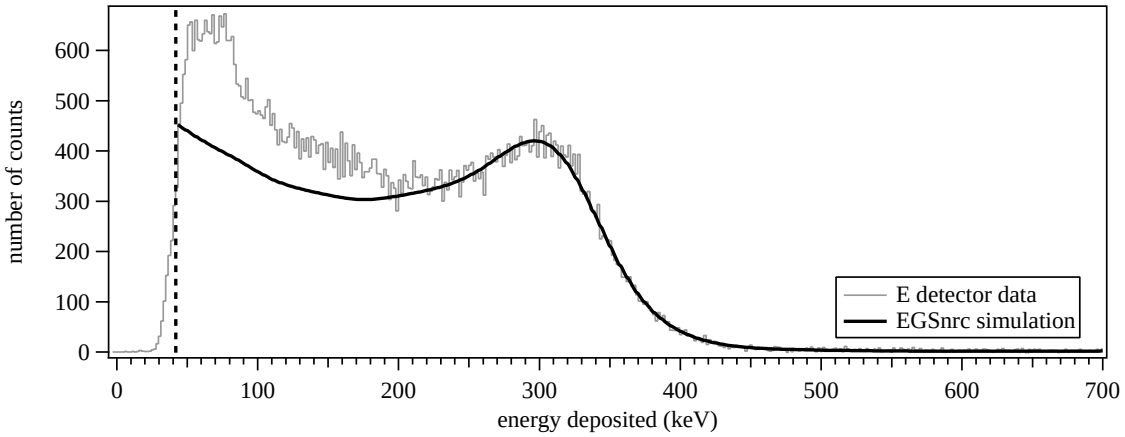

Figure 4.19: E detector response to 511 keV γ-rays from ^{68}Ga source inside acrylic. The Compton edge was used to determine the detection efficiency for annihilation radiation, and the excess at low pulse heights is likely due to scattering in the acrylic or surroundings.

to the EGSnrc predictions and measured detector resolution. A fit to the Compton edge determines the number of counts. We believe the low-energy excess, constituting ≈14% of the total, are from γ-ray scattering within the acrylic. Using EGSnrc, we estimate they should constitute 13% of the total. The measured detection efficiency of annihilation γ-rays is 13.0±1.4%, in agreement with 13.4% calculated using EGSnrc.

In principle, the low-energy tail from backscattering and bremstrahlung can be measured from $^{21}Ne^0$ recoils from the trap. $^{21}Ne^0$ reach the MCP in coincidence with detected β^+s when the recoil momentum, $\vec{p}_r$, is nearly antiparallel to the β^+ momentum, $\vec{p}_\beta$. The neutrino momentum, $\vec{p}_\nu$, is therefore either parallel or antiparallel to $\vec{p}_\beta$. If they are parallel, $\vec{p}_r$ is large regardless of $\vec{p}_\beta$, resulting in short TOFs (which are essentially inversely proportional to $|\vec{p}_r|$). Long TOFs can occur only when $\vec{p}_\nu$ opposes $\vec{p}_\beta$, and $|\vec{p}_\beta| > |\vec{p}_\nu|$. A Monte Carlo simulation (discussed in Chapter 5) of E_β as a function of the $^{21}Ne^0$ TOF is shown in Figure 4.20 for coincident $\beta^+ - ^{21}Ne^0$ events.

For ground-state decays with TOF>2080 ns, we expect E_β >1 MeV. The measured energy distribution for the August 2001 run is shown in Figure 4.21. Events with E_β <1 MeV are attributed to the low-energy tail of the β-detector response, after a 2% correction for

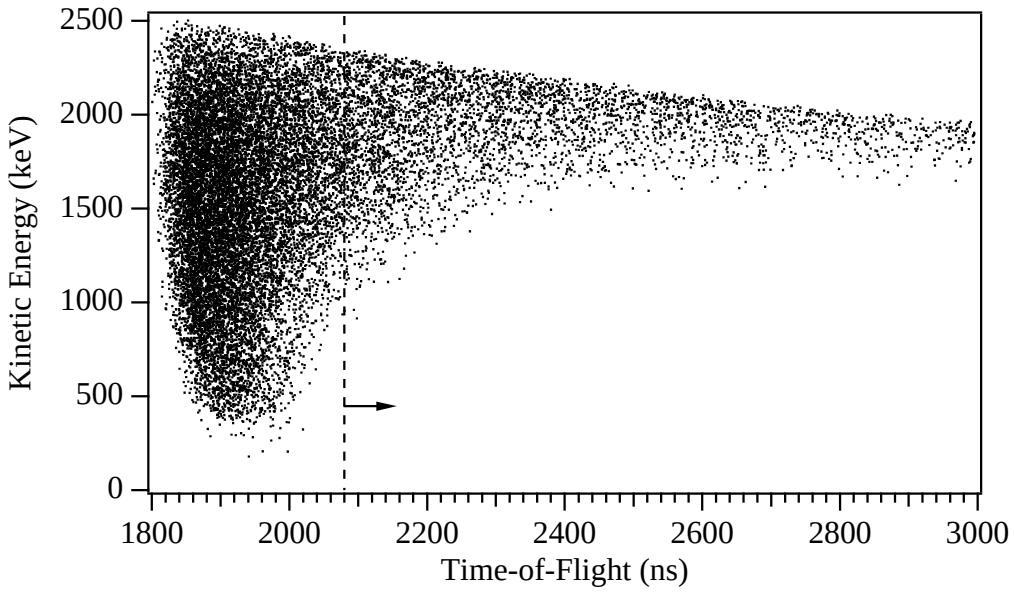

Figure 4.20: Scatter-plot showing E_β vs. TOF for coincident $\beta^+ - {}^{21}\mathrm{Ne}^0$ events calculated with the Monte Carlo discussed in Chapter 5. In the region with TOF>2080 ns, we find E_β >1 MeV.

decays to the excited-state. Unfortunately, the neutral signal-to-noise is poor even with cuts on the MCP pulse height to minimize the background. We find 3.2±2.9% of events in the tail which compares favorably to the EGSnrc prediction of 2.5%, but does not provide a stringent test of the calibration.

4.5 Electrodes

The electrode configuration within the trapping chamber is shown in Figure 4.22.

4.5.1 Collimator

The problems associated with scattered βs mentioned in Section 4.2.2 were reduced by placing a tungsten alloy collimator in front of the β-detector. The tip of the collimator is thin to minimize scattering from the edge. The machinable tungsten alloy HM 3000 (95% W, 3.5% Ni, 1.5% Cu) from Hogen Industries, Inc.$^{\mathrm{TM}}$ with a density of 18.0 g/cm^3 was

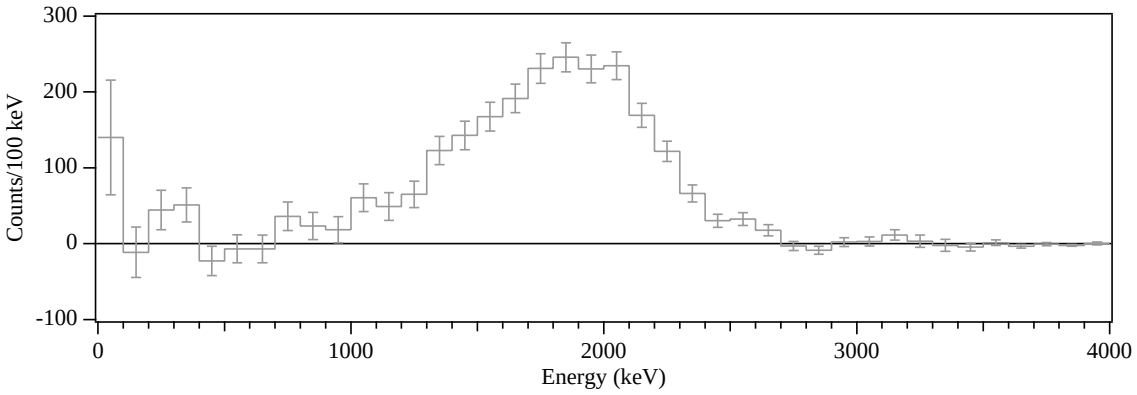

Figure 4.21: β energy spectrum for events with 2080 ns>TOF>2200 ns and MCP pulse heights less than ADC channel 80.

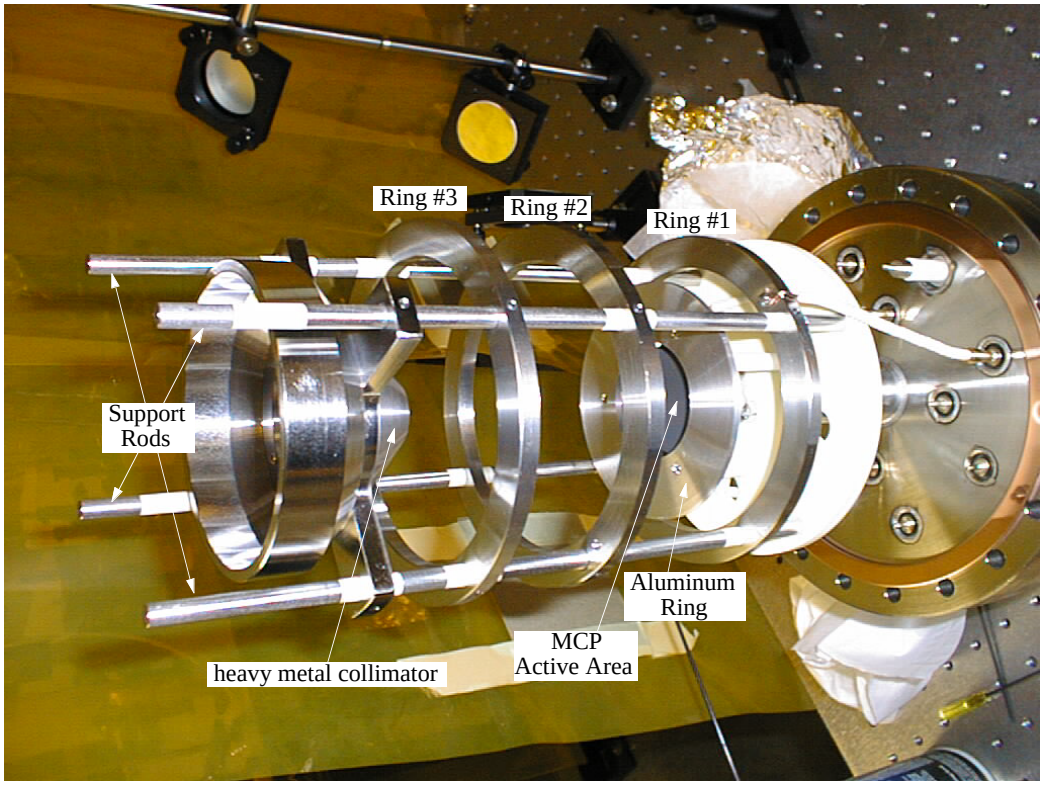

Figure 4.22: Photo of electrodes.

chosen so that 1 mm would stop even the highest energy βs. The alloy is non-magnetic and does not distort the trapping fields. With the addition of the collimator, most scattered events do not reach the detector. Events that backscatter off the MCP and its electrode ring are detected but are few in number. From the trap, the collimator tip solid angle is 0.1% of 4π. Using EGSnrc, we find 4.0% of β^+s that strike the tip subsequently reach the β-detector.

The backgrounds seen in earlier runs from ^{21}Na deposited near the β-detector is absent in background runs. Positrons coming from the outside collimator surface do not reach the β-detector without scattering and ions from the Be window or the inner collimator surface can not reach the MCP. Recoil-ions emerging from the collimator tip have TOFs similar to recoil-ions from the trap. In trapping and background runs, we expect a comparable number of atoms to stick the chamber surfaces. Since the background is flat after accounting for the periodic pulses from the cyclotron, we limit this background by searching for a peak. We find $<0.02\%$ of the $^{21}Ne^+$ events from originate the collimator tip, leading to an uncertainty of <0.0004 in $a_{\beta\nu}$.

4.5.2 Electric Field

A static electric field of $\approx$1 kV/cm guides ^{21}Ne ions to the MCP active area, which is floated to -5.2 kV. Precise knowledge of the electric field is critical — uncertainties in the field strength correlate with the TOF distribution and the $\beta-\nu$ correlation. The electrodes and collimator were designed so the field could be calculated reliably. All components were designed to have simple, symmetric shapes with integer millimeter dimensions. Parts were machined to better than 0.1 mm precision. After assembly, the electrode positions were measured to a precision of <0.2 mm. An aluminum ring 10 mm in front of the MCP allowed the electric field to be unaffected by the MCP leads and screw heads.

The electrode configuration was modified several times. The four support rods that hold the electrodes in place were originally made of alumina. The voltage leads for the electrodes were difficult to model and significantly altered the electric field. The alumina

rods could collect charge, significantly influencing the field. To minimize the dielectric material and eliminate the separate voltage leads, two opposite pairs of stainless steel rods hold the electrodes in place and fix their voltage. The high voltage power supply front panels display the applied voltages with an uncertainty of less than ± 6 V, in agreement with direct measurement using a high voltage probe.

Electrodes were designed to allow the optical access needed to trap atoms. A three-dimensional simulation in SimIon 7.0 of the electrode configuration with sample $^{21}Ne^{+}$ trajectories is shown in Figure 4.23. The collimator provides angular rejection for the β-detector. The conical shape is modeled accurately but uncertainties in its position and voltage dominate the electric field uncertainties because of proximity to the trapped atoms and high voltage. The electric field also eliminates many potential backgrounds. A potential barrier of $\approx$1 kV is insurmountable to recoil-ions originating on the chamber walls. Neutrals from the walls do not cause coincidences because their TOFs fall outside the 3 μs timing window.

4.6 Electronics

The electronics layout is summarized in Figure 4.24. We achieved a timing resolution of $<$1 ns using constant fraction discriminators (CFD) with 25 mV thresholds for the ΔE, E, and MCP detectors. A 50 Ω splitter sent half the charge to the CFD and half to be digitized by 2249W analog-to-digital converters (ADCs). The ΔE and E thresholds were at energies of 10 and 35 keV, respectively.

A trigger from the ΔE or E starts a 3 μs coincidence window. A MCP trigger during this window sends a "start" signal to a LBNL issue 21X9191 P-1 time-to-amplitude converter (TAC). The end of the window is the "stop" signal. The TAC output, Δt, is digitized by an AD413 8K ADC. The TOF is (3 μs$-\Delta t$). Most delay generators are stable only to 0.1% of the delay (3 ns in this application). We used cable delay to define the window duration and achieved 0.25 ns stability. For each coincidence, the Δt's, the pulse heights for the MCP, ΔE, and E detectors, the trap fluorescence, and detector singles rates

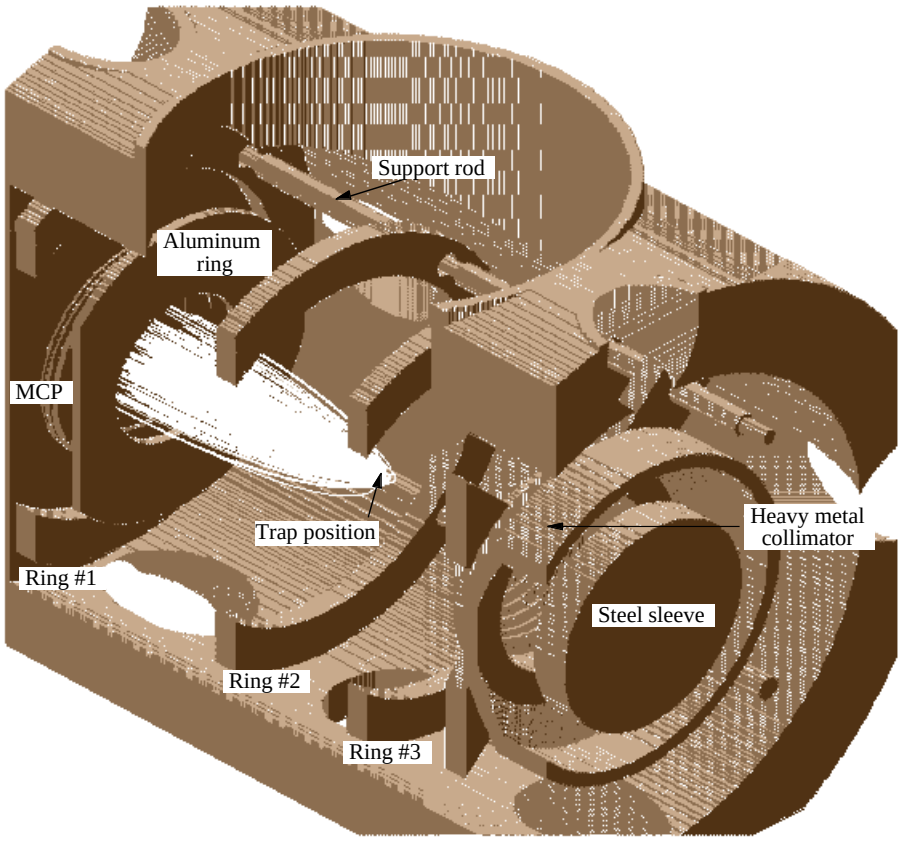

Figure 4.23: A cut-away, three-dimensional view of chamber interior and electrodes. Sample $^{21}Ne^{+}$ trajectories calculated by SimIon 7.0 are shown.

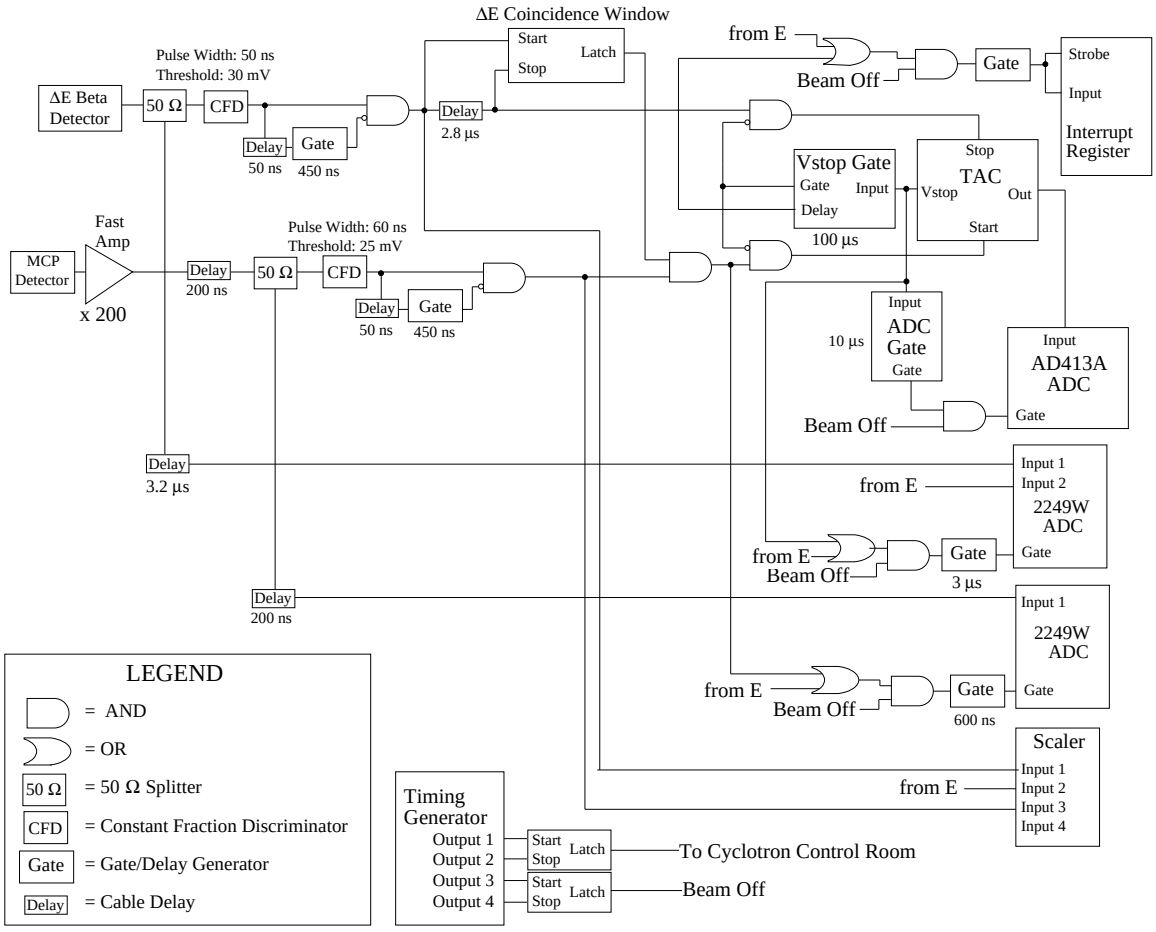

Figure 4.24: Electronics used for $\beta - \nu$ correlation experiment.

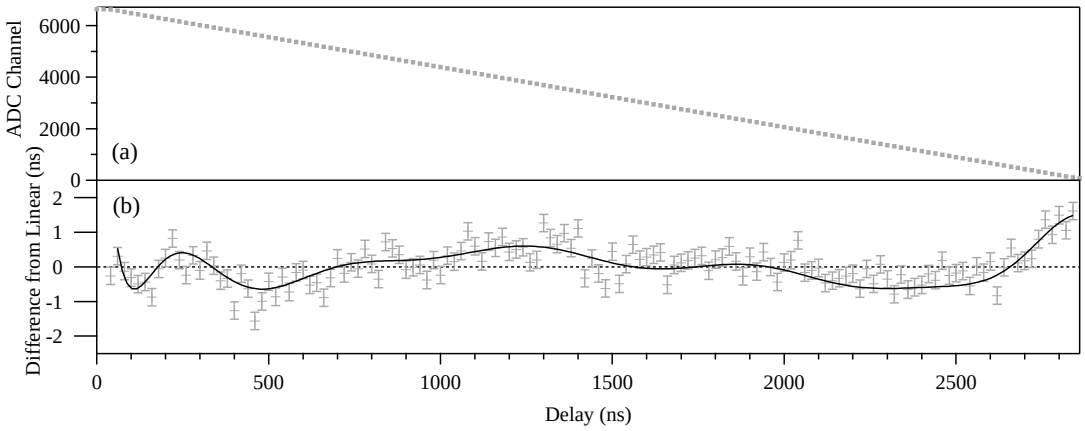

Figure 4.25: Timing calibration using a delayed β-detector signal for the MCP signal. (a) shows the measured ADC channel for each delay, and (b) shows the deviation from a linear fit, with a smooth curve overlaid to guide the eye.

are digitized.

The linearity and scale of the TAC/ADC timing system was measured by substituting a delayed β signal for the MCP signal. We varied the delay in increments of 20 ns over the 3 μs range using a Berkeley Nucleonics Corp. (BNC) Model 7030 Programmable Digital Delay Generator. The slope in Figure 4.25 is 0.42948$\pm$0.00007 ns/channel. The timing offset is determined from backscattered β^+ events in the coincident data and is discussed in Section 7.3. The calibration uncertainty is dominated by the temperature dependence of the delay generator. The room air conditioners maintained the temperature at nearly 73°C during the data runs and calibrations. Figure 4.25 (b) shows the differential non-linearity.

The signal from the PMT that views the trap fluorescence is nearly constant for seconds at a time and was not sent directly into an ADC. Instead, a 74HC4053 analog multiplexer/demultiplexer acted as a rapid switch to pass the signal only when the AD413A ADC received a gate. Using a calibrated laser beam, the PMT response (with a 10.47 kΩ shunt resistor) was 340 V/pW at 589 nm and the ADC response was 1.14 pW/channel.

Chapter 5

Monte Carlo Simulation

The analysis of recoil-ion data relies on a detailed Monte Carlo simulation of the time-of-flight spectra; in particular, the terms proportional to $F_1(E_\beta)$ and $a_{\beta\nu}(E_\beta)$ in Equation 2.13. We call the differential decay rate proportional to these terms Γ_1 and Γ_a, respectively. ^{21}Ne neutrals and ions are generated with recoil momenta determined by the kinematics for β's that hit the scintillator. The electric field through which the recoils propagate is calculated with SimIon 7.0. With this program, we obtain the ion time-of-flight, energy, and position of MCP impact. The measured β-detector and MCP efficiencies establish accepted events. Decays to the excited-state, decays involving emission of hard bremsstrahlung radiation, and coincidences involving β's that scatter off either the inner lip of the collimator or the MCP are included in the simulation. In all, twelve TOF spectra are generated for each charge-state.

5.1 Recoil Kinematics

For each time-of-flight spectrum, the β energy, E_β, is uniformly generated over the range $0 \leq E_\beta \leq E_0$ and $\hat{p}_\beta$ and $\hat{p}_\nu$, corresponding to β and ν unit momentum vectors, are uniformly generated over the surface of the unit sphere. In units of the electron mass, $m_e c^2$, conservation of energy then determines the neutrino energy

$$E_\nu = \frac{E_0 - E_\beta - \frac{E_0^2-1}{2M}}{1 - \frac{E_\beta - |\vec{p}_\beta| \cos\theta_{\beta\nu}}{M}} \tag{5.1}$$

which includes the nuclear recoil of 0–230 eV even though it is smaller than the present 700 eV uncertainty in E_0. We ignore perturbations from electron shake-off (except the small daughter mass change from electron loss). It is rapid (~fs) and results in a negligible momentum perturbation, even from 1 keV shake-off electrons. The recoil energy, E_r, and momentum, $\vec{p}_r$, are then calculated from conservation of momentum. We assume decays occur at rest since thermal velocity (~1 m/s) is dwarfed by the nuclear velocities (~4×10^4 m/s).

We apply the rejection method to generate E_β according to the differential decay rate. We choose random numbers E_{rand} between 1 and E_0 and Γ_{rand} between 0 and Γ_{max}, where Γ_{max} is the maximum value of Γ_1. If Γ_{rand} is less than the absolute value of the phase space factor at E_{rand}, the event is accepted and the sign of the phase space contribution is recorded. Although the phase space contribution is always positive for the isotropic term, the $\beta-\nu$ correlated term has positive and negative contributions. The physical correlation includes the isotropic term and is always positive.

For each charge-state, six pairs of Γ_1 and Γ_a event files are generated. The majority of coincidences are from decays to the ground-state (GS), but we also generate event files for excited-state (ES) decays, hard bremsstrahlung contributions to GS and ES decays, β^+ scattering off the inner lip of the collimator for GS decays, and β^+ backscattering off the MCP face and aluminum ring for GS decays. The fraction of events in each and the correction to $a_{\beta\nu}$ are summarized in Table 5.1.

Each decay is randomly assigned a location according to the measured trap distribution. The CCD camera images indicate a roughly Gaussian distribution with a FWHM of ≈0.80 mm. For each spectrum except the scattered and backscattered spectra, the β is propagated along its momentum vector and saved only if it hits the β-detector. The electric and magnetic fields only significantly influence the flight path of the lowest energy (and essentially undetected) β^+'s. The recoil's initial position, energy, velocity vector, charge-state, and mass are recorded in a format appropriate for SimIon 7.0. A second file stores the β^+ energy, radial position of detector contact, and the sign of the contribution to phase

Description	Symbols	Number of events	Correction	uncertainty
Ground-state decays	Γ_1^{GS}, Γ_a^{GS}	1.0	–	–
Excited-state decays	Γ_1^{ES}, Γ_a^{ES}	0.0529	0.0681	0.0033
GS hard brem. decays	Γ_1^{GSH}, Γ_a^{GSH}	0.02518	0.0041	–
ES hard brem. decays	Γ_1^{ESH}, Γ_a^{ESH}	0.00119	0.0002	–
Collimator scattering	Γ_1^{CS}, Γ_a^{CS}	0.0139	0.0005	0.0002
MCP backscattering	Γ_1^{BS}, Γ_a^{BS}	0.0050	0.0089	0.0028

Table 5.1: Summary of decay files generated by the Monte Carlo simulation. Corrections and uncertainties for hard bremsstrahlung decay includes virtual/soft radiative corrections.

space.

5.1.1 Allowed β Spectrum and Corrections

For GS decays, we apply the rejection method using the allowed spectrum including recoil order ($\delta_{ro}(E_\beta)$), Z-dependent radiative ($\delta_{em}(E_\beta)$), and virtual/soft bremsstrahlung ($\delta_{VS}(E_\beta)$) corrections as described in Chapter 2. The β spectra for Γ_1 and Γ_a are

$$\Gamma_1^{GS} = F(Z,p_\beta)p_\beta E_\beta(E_0 - E_\beta)^2(1 + \delta_{ro}^1(E_\beta) + \delta_{em}^1(E_\beta) + \delta_{VS}^1(E_\beta)) \tag{5.2}$$

and

$$\Gamma_a^{GS} = F(Z,p_e)p_\beta^2(E_0 - E_\beta)^2(1 + \delta_{ro}^a(E_\beta) + \delta_{em}^a(E_\beta) + \delta_{VS}^a(E_\beta)). \tag{5.3}$$

The Fermi function, $F(Z,p_\beta)$, is a cubic spline of the tabulated values in Ref. [106], including the atomic screening corrections.

The Z-independent order-α radiative corrections are broken into two contributions as described in Ref. [65]. The virtual and soft radiative correction, although complicated, are easily be included as a distortion to the allowed spectrum. Hard bremsstrahlung events are generated separately because of the entirely different kinematics associated with the four-body phase space. Integration of the phase space distribution indicates this involves 2.518% of ground-state decays. Both hard and virtual/soft bremsstrahlung must be included to cancel infrared divergences. The corrections for allowed β decay [65] are complicated and are not reproduced here.

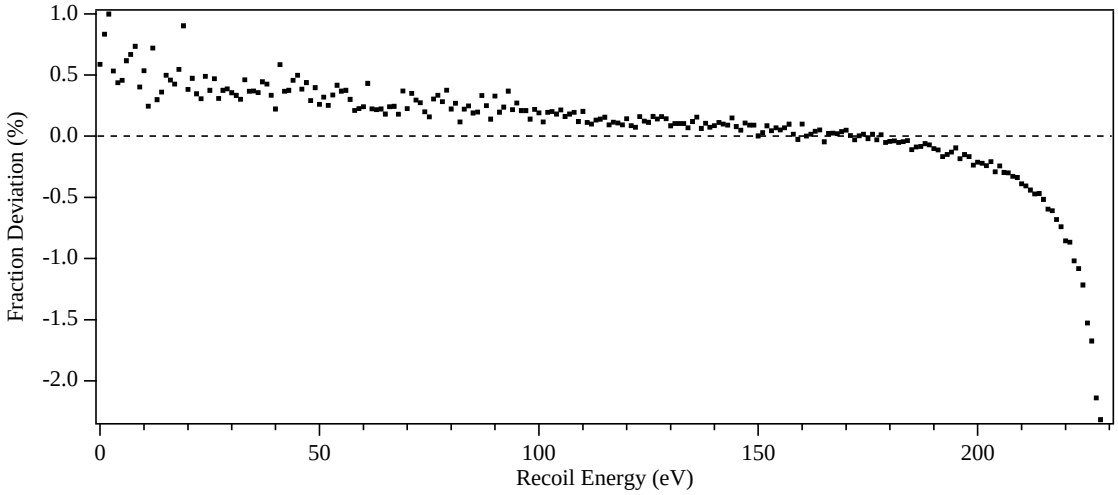

Figure 5.1: Calculated deviation in recoil energy spectrum from Z-independent radiative corrections. We have used 1 eV bins and the scatter of the points is indicative of the statistical uncertainty.

We checked this critical part of the Monte Carlo code in several ways. The ft value calculated with all the above corrections agrees to within 0.02% with the calculation in Ref. [51]. We obtained the same $\beta - \nu$ correlation in Ref. [15] using this code with E_0, M, and $F(Z, p_\beta)$ appropriate for the β^- decay of ^{6}He. The recoil order corrections change the measured $\beta - \nu$ correlation by $\approx$0.0001, as expected, since they are proportional to $E_0 - \frac{1}{2}E_\beta$, which averages to nearly zero over the β spectrum. Radiative corrections were checked by reproducing the results given of Ref. [107] for ^{6}He and ^{32}Ar β decays. The net effect of these radiative corrections is to decrease the number of high-energy recoils and diminish the $\beta - \nu$ correlation. The fractional deviation in the recoil spectrum of ^{21}Na is shown in Figure 5.1. The $\beta - \nu$ correlation is decreased by 0.0041, which is comparable to the corrections for ^{6}He and ^{32}Ar [107].

5.1.2 Excited-State Decays

Separate time-of-flight spectra are generated for the 5.02% pure Gamow-Teller β^+ branch to the excited-state. These β decays have an allowed shape with $E_0 = 2174.6$ keV

and $a_{\beta\nu} = -\frac{1}{3}$. The terms a, b, and c that determine the recoil order corrections are also different. However, the ambiguity in the signs of b and c calculated in Chapter 2 prevent the sign of the recoil order corrections from being determined. We neglect these effects; they are small corrections to an already small decay branch, leading to an uncertainty of <0.0001 in $a_{\beta\nu}$ for ground-state decays. Radiative corrections are included because the magnitude and sign is known.

After computing the nuclear recoil in the same manner as described previously for ground-state decays, additional recoil from the M1 emission of the 350.7 keV γ-ray is included. Since the lifetime of the excited-state is 10 ps, the daughters travel only fractions of a micron before decaying to the ground-state. The β and γ-ray emission is simultaneous in the Monte Carlo simulation. The γ-ray emission is isotropic since the $\beta - \gamma$ correlation for this decay is $<0.01\%$ [58] as was discussed in Chapter 2.

5.1.3 Scattered and Backscattered Events

Events with β^+s that scatter off the collimator tip or backscatter off the MCP are simulated. There are few coincident events from collimator tip scattering because the solid angle from the trap is 10% of that of the β-detector and only $13.9\pm2.1\%$ of β^+s that hit the collimator lip reach the β-detector according to a simple calculation with EGSnrc. We estimate the TOF spectra and find that the correction to $a_{\beta\nu}$ is 0.0005 ± 0.0002.

The collimator limits regions from which a β^+ can single scatter to the β-detector to the MCP detector and the aluminum ring. The "backscattered" spectrum comes from backscatters from the MCP and aluminum ring. The number of events is only 0.5% of the total because solid angles and backscattering off of Si and Al are all small. Since the β momentum is opposite that of ordinary events, these ions have longer TOFs. We simulate these events with a random β momentum at the point of backscattering. If the β makes it through the collimator and into the β-detector, it is saved so the corresponding recoil-daughter can be propagated through the chamber. This results in a correction of 0.0089 ± 0.0028 to the $\beta - \nu$ correlation.

5.2 Electric Field Calculation and Ion Propagation

The electric field is calculated by SimIon 7.0 with a three-dimensional, 0.5 mm grid. Electrode and chamber dimensions are accurate to better than ± 0.25 mm, and often to better than ± 0.10 mm. Figure 5.2 is a view of the SimIon 7.0 simulation. The size of the lattice spacing is limited by the maximum number of lattice points (500,000) allowed in SimIon 7.0. We do not include the entire chamber volume in the simulation since the grounded flange walls extend far from the trapping chamber body. However, the grounded chamber wall asymmetry from the 15.24 cm diameter port leading to the ion pump causes an electric field distortion that must be included. Including the first 25 mm of the 15.24 cm flange, and 12 mm of each 5.08 cm flange allowed us to calculate ion trajectories to sufficient accuracy. In addition, the regions behind the MCP detector and β-detector collimator have negligible influence and are not included. We estimate that including the neglected volume would alter $a_{\beta\nu}$ by $\lesssim 0.001$.

SimIon 7.0 calculates the trajectories for recoil-ions generated from the Monte Carlo. The ^{21}Ne energy, position, and time-of-flight are recorded when material is struck. The magnitude of the electric field is verified by comparing the measured TOF of the recoil-ions from the trap to the TOF predicted by the Monte Carlo simulation. The trap-to-MCP distance is accurately determined by the TOF of $^{21}Ne^{0}$ recoils since the initial recoil velocity is known. The rising edge of the ion TOF peaks agree with the Monte Carlo to an uncertainty of 0.6 ns and the electric field is accurate to 0.2%.

The SimIon simulation is used to optimize the electric field. For uniform detection efficiency, recoil-ions should reach the MCP active area with nearly identical energy and at nearly normal incidence. This is easily accomplished with voltages of less than 6 kV on the electrodes. It is also desirable to separate the TOFs of the slowest $^{21}Ne^{+2}$ and fastest $^{21}Ne^{+}$ recoils so that they may be fit independently. The electric field used in the August 2001 run was calculated from the voltages shown in Table 5.2. These voltages where chosen so that 99.5% of $^{21}Ne^{+}$ (in coincidence with detected β^{+}s) and 100% of all higher charge-state

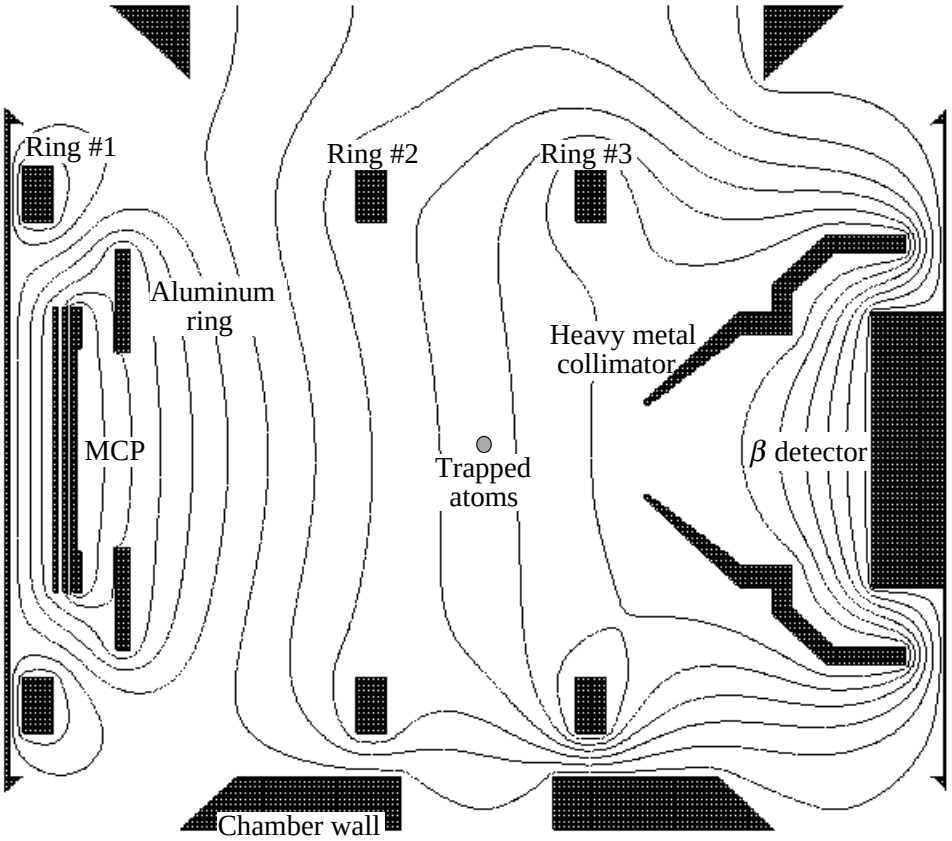

Figure 5.2: Cross-sectional view of electrode geometry. Equipotential lines are drawn with 1 kV separation.

Electrode	Voltage	Uncertainty
MCP V_{in}	-5207.9	6.0
MCP V_{out}	-3263.0	4.0
MCP anode	-3161.5	4.0
Collimator	5992.8	6.0
Ring 3	5992.8	6.0
Ring 2	3024.1	3.0
Ring 1	2000.0	5.0

Table 5.2: Voltages applied to electrodes and MCP during the August 2001 run.

ions were drawn to the MCP active area. In addition, separating the charge-state TOF peaks allows us to fit them independently and the kinematically forbidden TOFs between peaks allows us to check backgrounds. Using a simple program to calculate the end points of neutral recoil trajectories, we conclude only 18.5±0.1% of $^{21}Ne^{0}$ strike the MCP active area.

5.3 Particle Detection

Once the TOF is determined for each event, the detector efficiencies determine which $\beta^{+}-^{21}$Ne pairs are accepted. The MCP calibration discussed in Chapter 4 uncovered a positional sensitive detection efficiency that must be included in the analysis. For the β-detector, both E_{β} and where the detector was struck are important for determining whether an event is detected. We include energy loss from the electric potential and Be window, which are important for small E_{β}.

5.3.1 MCP Detection Efficiency

Only ions that hit the MCP active area are considered. As discussed in Chapter 4, at the accelerated ion energies of >9 keV, the detection efficiency is nearly independent of energy. The spatial detection efficiency is included by taking a bilinear interpolation of the detection efficiencies measured on a 2.5 mm grid during the MCP off-line calibration.

From fits to the PHD, we estimate 3.9±0.6% of $^{21}Ne^{+}$ ions give pulses below the electronic threshold. Therefore, assuming the open area ratio of 60±3% determines the fraction of ions that cause electron cascades, the average $\mathcal{E}_{MCP}$ for $^{21}Ne^{+}$ recoils is 58±3%. Including the spatial dependence of $\mathcal{E}_{MCP}$ gives corrections of -0.0033 ± 0.0008 and $+0.0007\pm0.0006$ for the $\beta-\nu$ correlation coefficient for $^{21}Ne^{+}$ and $^{21}Ne^{+2}$, respectively.

Uncertainties in the detection efficiency for low-energy $^{21}Ne^{0}$ recoils limits the utility of these events for the $\beta-\nu$ correlation. At energies below 2 keV, the detection efficiency is assumed to be proportional to kinetic energy. We also assume a fraction of the neutrals (6±6% based on orbital overlap calculations) are created in atomic metastable states, the most prevalent configurations probably being $1s^2 2s^2 2p^5 3p^1$ and $1s^2 2s^1 2p^6 3s^1$ with excitation energy of 17 and 19 eV, respectively. These recoils are expected to have a ∼10% MCP detection efficiency because of the CsI coating [93]. Therefore, 0.6±0.6% of the neutrals are detected in an energy-independent manner, while an average of 6% are detected with a linear energy dependence. The spatial dependence of the MCP gain has a large impact on the neutral detection efficiency. We assume that the output gain for the neutrals is proprotional to the output gain observed for the ions during the off-line calibration. Since the gain changed by roughly a factor of 2 between the center and edges, we obtain from Equation 6.8 that the detection efficiency changed by a factor of 1.8±0.2.

5.3.2 β Detection Efficiency

A β energy cut is applied to detected events. The only material βs from the trap encounter before reaching the β-detector is the 127 μm Be window that maintains the UHV. For low-energy βs the energy loss is significant and must be taken into account. The electric field retards 5 keV from all β^{+}s.

For β^{+}s passing through the Be window, we use EGSnrc to calculate the probability, $L_i(E_j)$, for a β^{+} of initial energy $E_j = 2.5\times j$ keV to emerge on the other side of the Be window with energy between $2.5\times(i-1)$ and $2.5\times i$ keV, where i and j are integers between 1 and 1010. The results are saved to a file called "beloss.txt" for use in the Monte

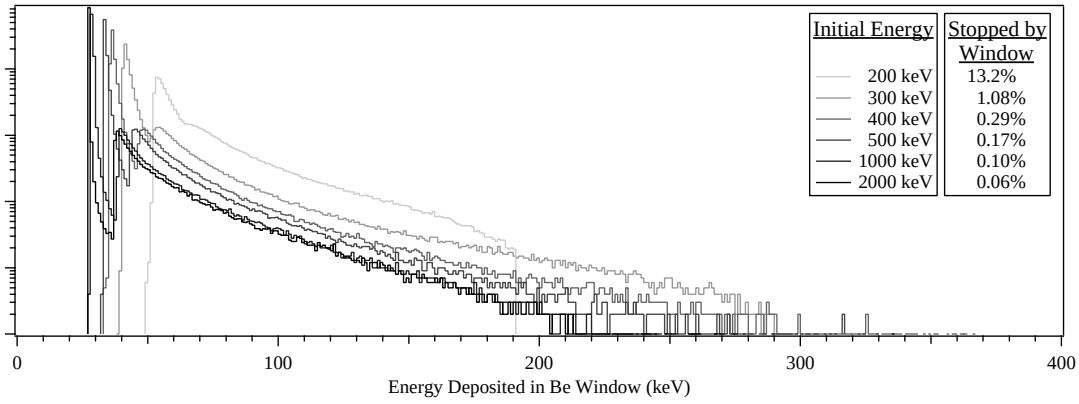

Figure 5.3: Calculated energy loss spectra for β^+s of several initial energies that penetrate the window. Not shown in the graph but listed by the legend are the percent of β^+s that do not penetrate the window, either because they deposit all their energy in the window or they backscatter from its surface.

Carlo simulation. Figure 5.3 shows these energy loss spectra, L_i, at several sample energies. At energies below $\lesssim$150 keV, β^+s cannot penetrate the Be window. Backscattered β^+s are considered to have lost all their energy in the window.

For each E_j, the L_i are normalized such that $\sum_{i=1}^{1010} L_i(E_j) = 1$. To calculate, δE_β, the energy lost by a particular β of energy E_β (a real number between 0 and 2525.4 keV), we first find the smallest integer k such that $k \geq E_\beta/2.5$. We define $\Delta k = k - E_\beta/2.5$. We then generate a random real number $X \in [0,1]$ and determine the smallest integer n, such that $\sum_{i=1}^{n} ((1-\Delta k)L_i(E_k) + \Delta k L_i(E_{k-1}) \equiv L_{max} \geq X$. Setting $\Delta L = L_{max} - x$, the energy loss is then

$$\delta E_\beta = L_{max} - \Delta L(\sum_{i=1}^{n-1}((1-\Delta k)L_i E_k + \Delta k L_i(E_{k+1})). \tag{5.4}$$

Using the full detector calibration, we obtain an acceptance function at the center and edge of the β-detector. As discussed earlier, the light fraction reaching the ΔE photomultiplier tube varies as a function of position as does the probability for additional energy deposited by γ-rays. The fraction of rejected events is plotted as a function of incident β energy in Figure 5.4. We accept 97.3$\pm$0.2% of the spectrum when a β-detector threshold

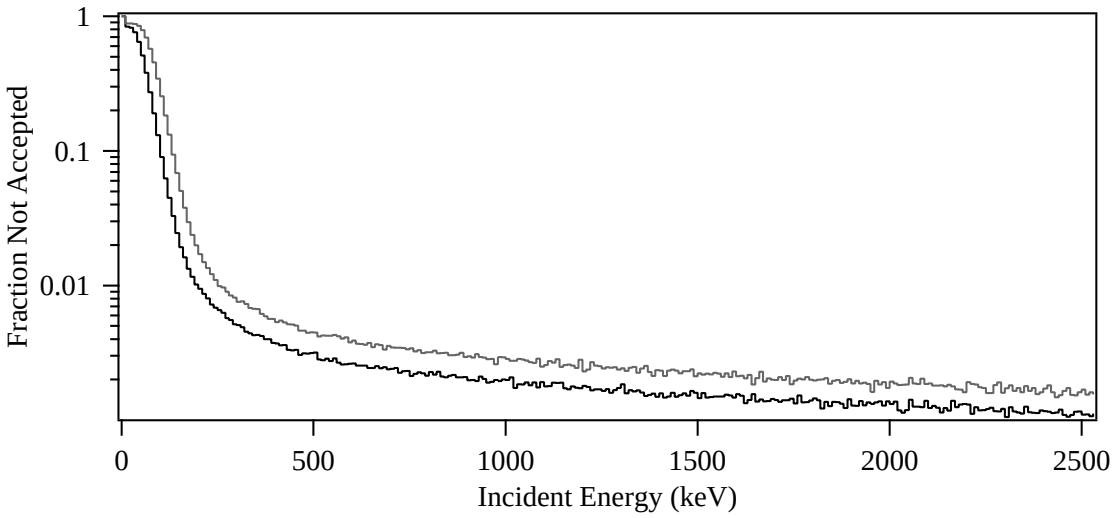

Figure 5.4: Calculated fraction of β^+s of energies between 0 and 2525 keV at the detector center (black) and edge (gray) that are not detected when a β-detector threshold of 50 keV is used.

of 50 keV is used.

5.4 Calculated Time-of-Flight Spectra

Coincident events passing the β-detector cuts and the recoil-ion cuts are accepted. From the number of events passing these cuts, we estimate the coincident detection efficiency to be 0.51±0.03% with an absolute MCP detection efficiency of 60±3%. A Gaussian spread with FWHM of 0.5 ns is added to the TOF, to account for the measured timing resolution of the detection system. In practice, the spatial spread of the trap limits the timing resolution to 7 ns. We histogram the coincident $\beta-^{21}$Ne events. The resulting TOF spectra calculated for each of the $^{21}Ne^+$ spectra in Table 5.1 are shown in Figure 5.5. The total spectrum for all charge-states in the electric field of the August 2001 run are shown in Figure 5.6.

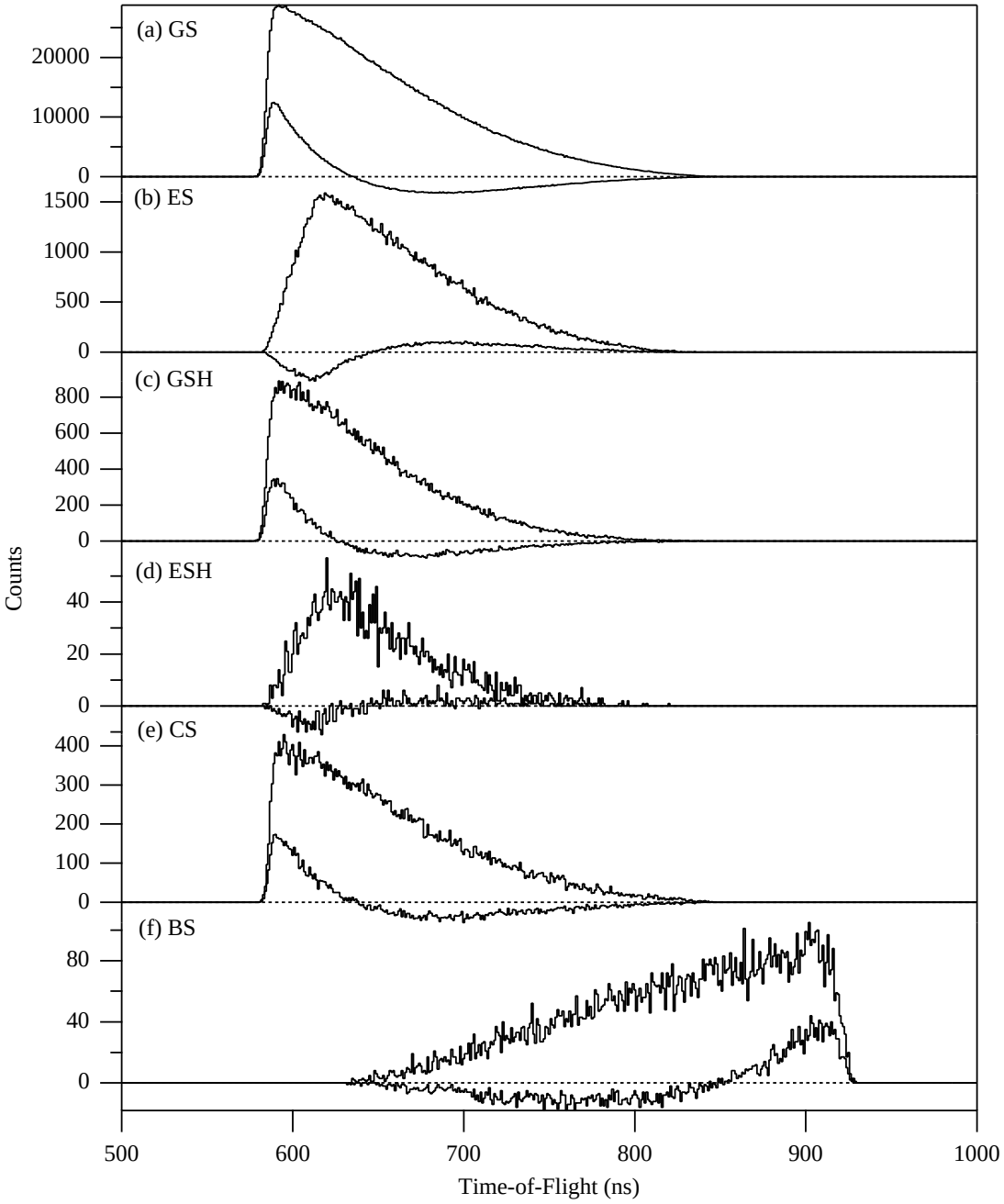

Figure 5.5: Time-of-flight spectra of $^{21}Ne^{+}$ for (a) Γ_1^{GS} and Γ_a^{GS}, (b) Γ_1^{ES} and Γ_a^{ES}, (c) Γ_1^{GSH} and Γ_a^{GSH}, (d) Γ_1^{ESH} and Γ_a^{ESH}, (e) Γ_1^{CS} and Γ_a^{CS}, (f) Γ_1^{BS} and Γ_a^{BS}. The spectra are displayed in 1 ns bins. The total number of events in Γ_1^{GS} is $3{\times}10^6$. Notice the large scale changes for each of the different spectra.

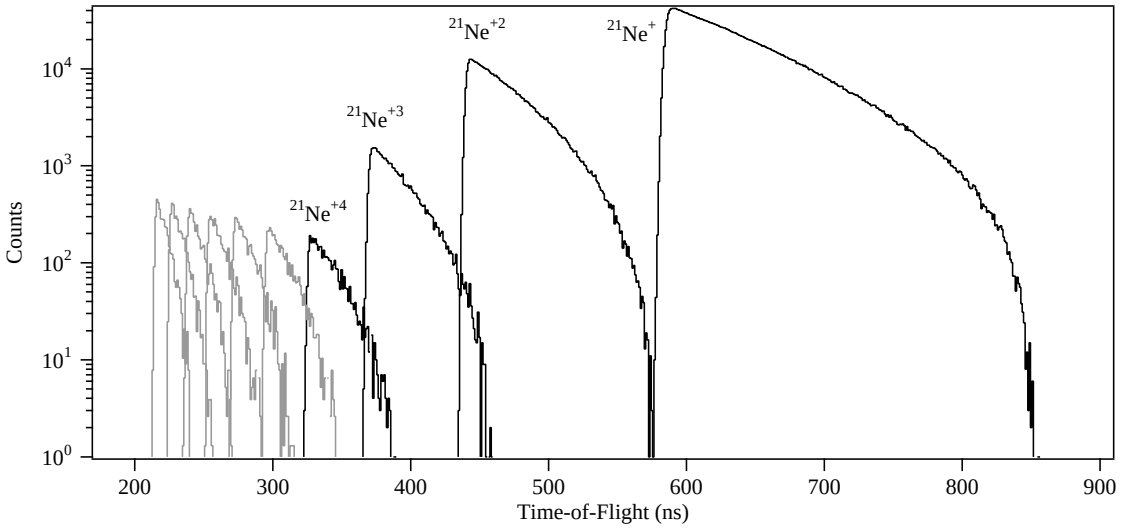

Figure 5.6: Anticipated TOF spectra (assuming no CS or BS). For the charge-states 1–4, ion production is based on experimental results. For higher charge-states (in gray) production is set equal to that of $^{21}Ne^{+4}$. Bin width is 1 ns and the number of events in the $^{21}Ne^{+}$ is $> 3 \times 10^6$.

5.5 Magnetic Field Effects

The magnetic fields used to trap the atoms have little effect on the flight path of β^+s and recoil-ions. These fields are <100 Gauss and practically parallel to the direction of motion. After calculating the magnetic fields resulting from the quadropole coils, the effect on the βs is a radial displacement of <0.06 mm. Similarly, by adding in a suitable magnetic field into SimIon 7.0, the radial displacement of the ions is 0.05 mm and the TOF change is 0.05 ns. These effects are ignorable. The magnetic field is not large enough to guide secondary electrons from the MCP front face back to the detector, avoiding MCP signals delayed by the electron flight time.

5.6 Deadtime Corrections

Since the acquisition detects only the first MCP trigger following any β-detector trigger, a slight bias exists for events with short TOFs. To accurately compare the TOF

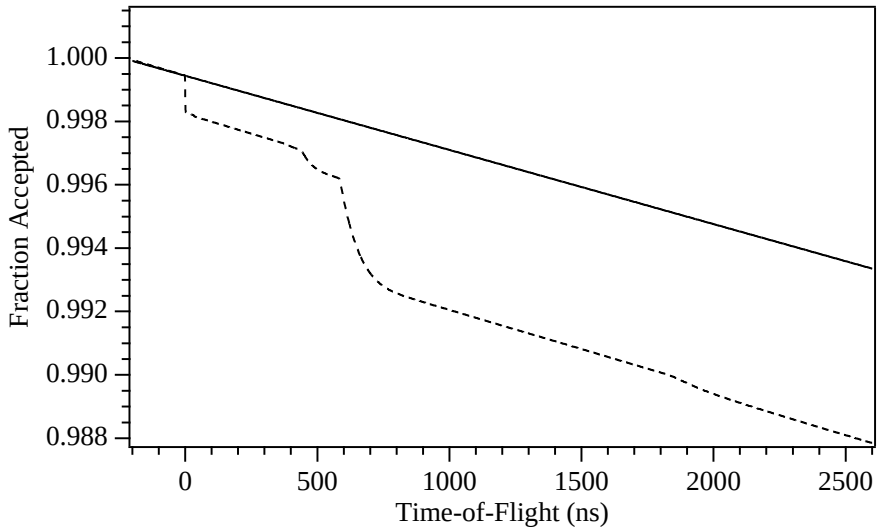

Figure 5.7: Estimated fraction of true (solid line) and accidental (dashed line) coincidences lost as a function of TOF during the August, 2001 run due to deadtime.

spectra calculated by the Monte Carlo to the recoil-ion data, we need to take into account the fraction of lost events at each TOF.

We distinguish the effects of true and accidental coincidences. We estimate the loss of accidental coincidences from the TOF spectrum of the accidental and true coincidences. Since only one MCP trigger can be in true coincidence with each β trigger, the true coincidences are corrected using only the TOF spectrum of accidental coincidences [108]. At rates of 4 kHz in the MCP, there is a 1.2% chance that an accidental coincidence will occur over the entire 3 μs coincidence window. The fraction of lost true and accidental coincidences is shown in Figure 5.7, using the measured TOF spectrum from the August 2001 run. Including these corrections has an appreciable effect only for charge-states +2 and higher.

Chapter 6

Recoil-Ion Charge-State Distribution

In this chapter we address whether or not ionization following β decay is independent of β and nuclear recoil energies. For β^+ emitters, ionization mechanisms are essential since positive daughter ions only form when $\geq$2 orbital electrons are lost. Negative ions, if formed, are often unstable. Ionization affects the statistical precision of the measurement. Ionization dependent on β or recoil-ion energy would alter each charge-state's energy spectrum, leading to an experimental signature similar to a $\beta - \nu$ correlation.

Understanding the ionization state following β decay is interesting in its own right. Charge-state distributions have been measured in a number of noble gas atoms. For β^- emitters, such as ^{6}He [109], ^{23}Ne [110], ^{85}Kr [111], and ^{41}Ar [112], electron shake-off (SO) resulting from parent/daughter orbital mismatch is the dominant process. The charge-state distribution decreases with increasing charge, with 80–90% of daughter ions having a charge +1 and <5% with charge $\geq$3. In addition, inner shell vacancies lead to dramatic ionization from Auger cascades in the electron capture (EC) decay of ^{37}Ar [113, 114], the internal conversion (IC) of ^{131m}Xe [115], and the β^- and IC decay of ^{133}Xe [116].

Until recent experiments with radioactive trapped atoms, there was no data on charge-state production following β^+ emission. The decay of the β-emitter ^{79}Kr is predominantly EC and produces positive ions, neutrals, and negative ions [117]. A simple estimate

equating the net electron loss in β^- and β^+ decay indicates <5% of the daughters should be positive, with yield decreasing with higher charge-state. However, experiments with laser trapped ^{38m}K [22] and ^{21}Na [118] show that the production of positive ions for β^+ emitters can be ≈20%.

We use the relative ^{21}Ne ion abundances to study the dependence of the ionization process on the decay product energies. In the "sudden approximation", electrons are ejected because of orbital mismatch following the sudden change in nuclear charge and ionization is independent of β energy. However, the energy imparted to shake-off electrons (of order the binding energy) reduces the available phase space [119], suppressing low-energy β emission. Ionization in the K-shell has significant β energy dependence, especially in the β^- decays of ^{99}Tc [119] and ^{147}Pm [119, 120] where the binding energy, B_K, and E_0 are comparable. In addition, the direct collision (DC) mechanism, in which the β knocks out an orbital electron, is expected to be important for decays with comparable B_K and E_0. Calculations indicate the DC mechanism can contribute significantly to electron loss at low β energies, even for decays with $B_K/E_0 \ll 1$, and measurements disagree with calculation unless this DC contribution is included. Therefore, even though shake-off from deeply bound K-shells is small, the energy dependence can be significant.

Nuclear recoil has observable ionizing effects for high-energy γ-ray [121], nucleon [121], and α emission [122]. In β decay, recoil ionization is expected to be small in most atoms so far investigated. A noteworthy exception is ^{6}He where E_0 is large and a small nuclear mass leads to recoil energies of up to 1400 eV. Nuclear recoil contributes 3% to the production of ^{6}Li^{+2}, and >50% to the production of ^{6}Li^{+3} [109]. No evidence of recoil ionization was found by comparing the abundances of charge-state +2 through +5 of ^{23}Ne β^- decay [110]. The data are not particularly restrictive and are summarized in Table 6.1.

Ions compared	Ratio at 250 eV	Ratio at 450 eV
$^{23}Na^{+2} : {}^{23}Na^{+}$	0.219±0.006	0.220±0.005
$^{23}Na^{+3} : {}^{23}Na^{+2}$	0.173±0.007	0.167±0.006
$^{23}Na^{+4} : {}^{23}Na^{+2}$	0.029±0.003	0.026±0.002
$^{23}Na^{+5} : {}^{23}Na^{+2}$	0.005±0.001	0.006±0.001

Table 6.1: Energy dependence of ^{23}Na ion production following the β^- decay of ^{23}Ne. Data from Ref. [110].

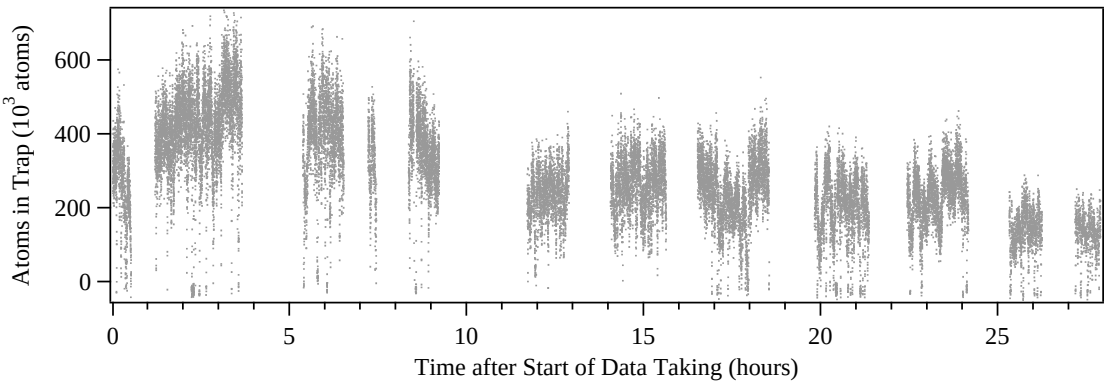

Figure 6.1: Trap population over the 28 hours of recoil-ion data collection on August 30–31, 2001.

6.1 Experimental Results

Over the course of the August 30, 2001 run, the trap contained an average of about 270,000 atoms. The fluorescence vs. time shown in Figure 6.1 indicates a trap population from 100,000 to 500,000 atoms. The gaps are periods when the background was measured. The occasional loss of trap population is due to the laser going out of regulation. Early in the run, the number of trapped atoms increases as the vacuum pressure recovers from the initial outgassing in the target induced by the proton beam. The number of atoms shows a gradual decline as the MgO disks slowly evaporate and ^{21}Na production decreases.

The time-of-flight (TOF) in Figure 6.2 clearly resolves the charge-states. In principle, positive, negative, and neutral charge-states are possible for β^+ decay. The detector

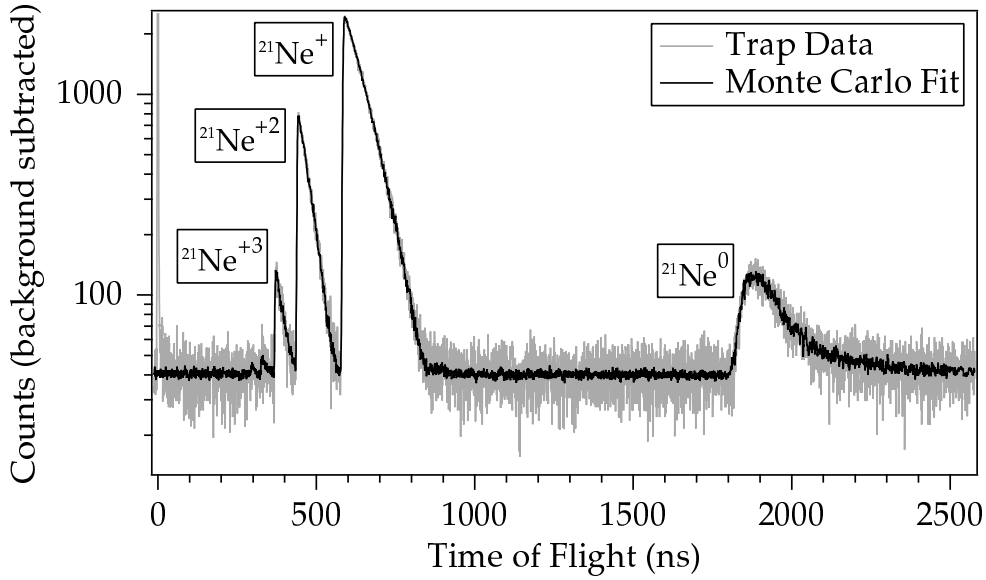

Figure 6.2: Recoil ^{21}Ne time-of-flight spectrum. The inclusion of the experimental $\gamma - ^{21}$Ne coincident TOF spectrum in the fit leads to noise in its background level.

is far more sensitive to positive ions than neutral atoms, and it can detect negative ions with electric fields reversed. As discussed below, we find no evidence for negative ions, and $^{21}Ne^0$, despite being the most prevalent, has the smallest absolute detection efficiency and largest uncertainties. With knowledge of the source activity and the detection efficiency for positive ion and β^+ coincidences, the entire charge-state distribution was reconstructed.

6.1.1 Negative Neon State

If all orbital electrons were retained, $^{21}Ne^-$ is formed. A calculation based on a nonrelativistic fixed-core valence-shell configuration interaction predicts the existence of a metastable Ar^- state, but the metastable Ne^- state is expected to decay to the continuum through an E1 transition [123]. Direct searches found Ar^- with a lifetime of $\sim$350 ns, and conclude that if Ne^- exists its lifetime is $\ll$ 50 ns [124], in agreement with the calculation. Even if Ne^- were metastable with an appreciable lifetime, the probability of remaining negative is small. The calculated metastable $^{21}Ne^-$ configuration ($1s^2 2s^2 2p^5 3p^2$) is not

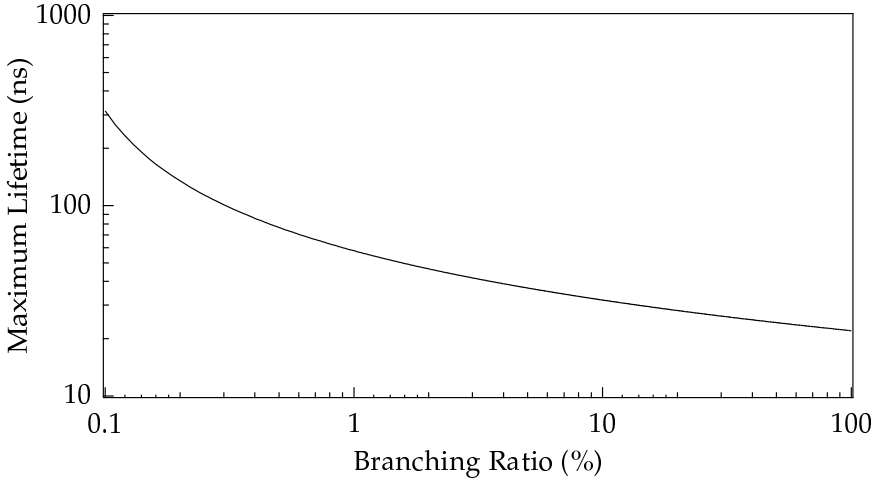

Figure 6.3: Maximum lifetime of $^{21}Ne^{-}$ vs. its β decay branching ratio (68% C.L.), assuming the MCP detection efficiency decreases linearly at energies below 2 keV.

accessible from the ground-state of Na ($1s^2 2s^2 2p^6 3s^1$) because of symmetry. However, due to the $3s \leftrightarrow 3p$ cycling from the trapping lasers, $\approx$30% are in the $1s^2 2s^2 2p^6 3p^1$ configuration. Since the overlap between the Na 2p and Ne 2p state is 97.05%, each 2p electron has less than a 3% chance of being shaken-up to the 3p state. The branching ratio for this configuration should be <5.4%. Moreover, with a lifetime $\ll$ 50 ns, $^{21}Ne^{-}$ would be difficult to distinguish from $^{21}Ne^{0}$. We conducted a direct search by reversing the direction of the electric field, finding no evidence of $\beta^{+} - ^{21}Ne^{-}$ or $\beta^{+} - ^{21}Ne^{0}$ coincidences at shorter TOF than kinematically allowed. The limits as a function of branching ratio are shown in Figure 6.3. We conclude $^{21}Ne^{-}$ is not a significant charge-state.

6.1.2 Positive Charge-States

The branching ratios for the positive charge-states are established from fits to Monte Carlo simulations. The distribution for $\gamma - ^{21}Ne$ coincidences, from events that deposit energy in the E but not the ΔE detector, are also included. The magnitude of this spectrum was scaled by the relative detection efficiency of the ΔE and E to 511 keV γ-rays.

The $^{21}Ne^{+q}$ accelerate to energies of $\approx 9.0 \times q$ [keV], and incident angles of <2°

Ions compared	Production ratio
$^{21}Ne^{+2}:^{21}Ne^{+}$	0.1673±0.0011
$^{21}Ne^{+3}:^{21}Ne^{+}$	0.0143±0.0003
$^{21}Ne^{+4}:^{21}Ne^{+}$	0.0013±0.0003
$^{21}Ne^{+5}:^{21}Ne^{+}$	0.0006±0.0003

Table 6.2: Ratio of production of positive ions relative to $^{21}Ne^{+}$ production. Corrections for MCP detection efficiency and deadtime losses have been taken into account. The ratio for ions with charge $\geq$6 is $\leq$0.0003.

at the MCP. References [102, 125, 126, 127, 128, 129, 130] conclude that above ~2 keV, the detection efficiency approaches the MCP open area ratio of ≈60%, independent of ion species or charge-state. The relative detection efficiency for the positive charge-states was determined by estimating the percentage of MCP pulses below the electronic threshold for a given charge-state using the off-line ion beam calibration. This amounts to a <2% correction. The relative charge-state ratios are given in Table 6.2.

6.1.3 Absolute Charge-State Ratios

The absolute branching ratios are determined from the source strength and detection efficiency for $\beta^{+}-^{21}$Ne coincidences. The neutral branching ratio is then determined by subtraction. The branching ratio, Γ_q, is

$$\Gamma_q = \frac{R_q}{R_T} \tag{6.1}$$

where R_q is the detection rate of ion recoils with charge $+q$ and R_T is

$$R_T = \frac{N \ln 2}{\tau_{1/2}} \Omega_{MCP} \Omega_\beta \mathcal{E}_{MCP} \mathcal{E}_\beta L. \tag{6.2}$$

Here N is the average number of ^{21}Na atoms in the trap (determined by the trap fluorescence as described in Section 3.6), $\tau_{1/2}$ the halflife, Ω_{MCP} and Ω_β the detector solid angles, $\mathcal{E}_{MCP}$ and $\mathcal{E}_\beta$ the detection efficiencies, and L the fraction of detector live time. The deadtime of the DAQ was 650 μs measured with a pulser. At coincident rates of 75 Hz, the

Quantity	Value	uncertainty
N	269,000	29,000
$\tau_{1/2}$[s]	22.48	0.04
Ω_{MCP}	0.996	0.001
Ω_{β}	0.0092	0.0002
$\mathcal{E}_{MCP}$	0.58	0.05
$\mathcal{E}_{\beta}$	0.973	0.001
L	0.95	0.01
R_{+1}[Hz]	7.58	0.01
R_T[Hz]	40.9	5.7
Γ_{+1}	0.186	0.026

Table 6.3: Relavent values and uncertainties in the quantities needed for calculating the charge-state branching ratios.

deadtime is 5%. The quantities used for determining the absolute charge-state distribution are summarized in Table 6.3.

6.1.4 Comparison with ^{23}Ne β^- decay

Figure 6.4 shows a comparison of the daughter charge-state distribution following ^{21}Na β^+ decay with the β^- decay of ^{23}Ne. One might expect the β^+ charge-state distribution to be similar to the β^- distribution shifted by a charge of +2 because of the difference in sign of ΔZ. The branching ratios, however, are remarkably similar when shifted by only one unit of charge. This indicates that an extra electron, most likely the valence electron, is frequently lost in ^{21}Na β^+ decay, leading to positive ions following 22.0±3.1% of decays instead of the expected ≈5%.

6.1.5 Dependence on Decay Product Energy

In neon, 99% of K-shell vacancies lead to subsequent Auger transitions [131], so K-shell ionization contributes significantly to the production of ^{21}Ne^{+2} (≈30%) but not ^{21}Ne^{+} (<0.1%), in the model discussed below. We do not expect ^{21}Ne^{+} ion production should

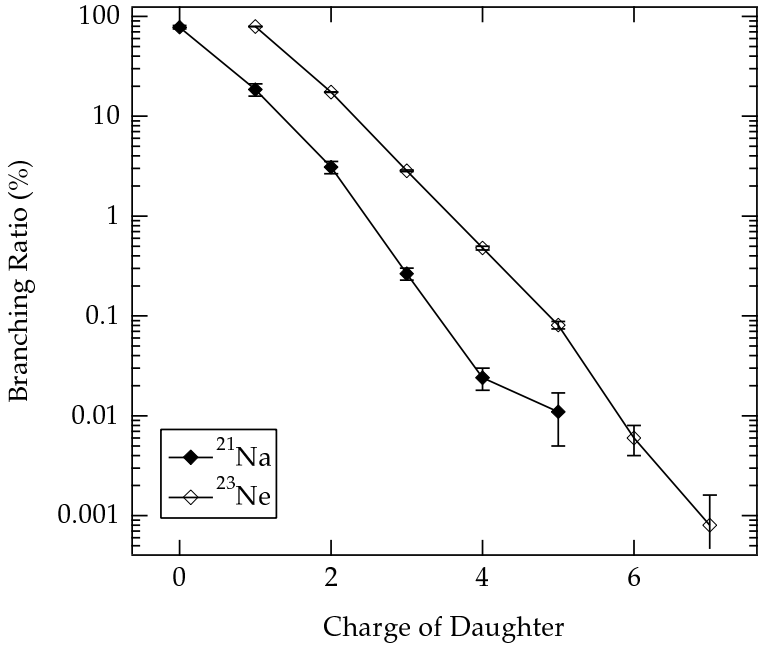

Figure 6.4: Comparison of charge-state distributions following the β^+ decay of ^{21}Na and the β^- decay of ^{23}Ne. Points are connected to guide the eye.

exhibit significant β energy dependence, although higher charge-states may. Although for β decay correlation studies the singly-charged ions provide the bulk of the statistics, consistent results for each charge-state are required for a conclusive result. The ratio of $^{21}Ne^{+2}$ to $^{21}Ne^{+}$ as a function of β energy is sensitive to energy dependence of ionization of the K-shell. The ratio of Q-value to B_K in ^{21}Na is >2500, ensuring the phase space is minimally effected.

We calculate the change in phase space due to K-shell shake-off using non-relativistic hydrogenic wavefunctions. The K-shell ionization probability per β emission of energy E_β, $P_K(E_\beta)$, is expressed as

$$P_K(E_\beta) = \int_{m_e}^{E_0 - B_K - E_\beta} \frac{(E_0 - B_K - E_\beta - E_K)^2}{2\pi^2 (E_0 - E_\beta)^2} p_K E_K |M(E_K)|^2 dE_K \qquad (6.3)$$

where $|M(E_K)|^2$ is the overlap between K-shell electron (of nucleus with charge Z) and continuum state of energy E_K (in the field of a nuclear charge $Z + \Delta Z$) and $p_K = \sqrt{2 m_e E_K}$

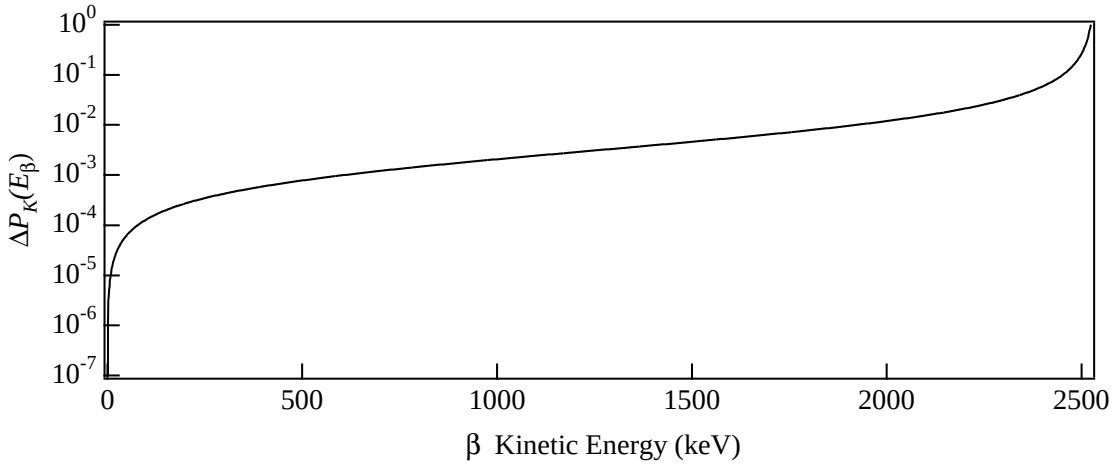

Figure 6.5: Fractional change in K-shell ionization due to E_β.

[119]. In the non-relativistic limit,

$$|M(E_K)|^2 = \frac{2^6 e^{-4n' \tan^{-1}(n)}}{\alpha^2 Z^4 (n^2+1)^4 (1-e^{-2\pi n'})} \tag{6.4}$$

with $n = \frac{p_K}{\alpha Z m_e}$ and $n' = n^{-1}$ [132]. We plot the fractional change in K-shell ionization probability due to E_β, $\Delta P_K(E_\beta) = 1 - \frac{P_K(E_\beta)}{P_K(0)}$, in Figure 6.5, where $P_K(0)$ (the maximum value of $P_K(E_\beta)$) is used for normalization. The small difference from zero at all but the last several keV demonstrates that this is a small effect. Even if all ionization resulted from the K-shell, the effect on the β decay correlations in ^{21}Na would be <0.1% [133].

The ratio of K-shell electrons ejected per decay by direct collisions ($P_K(DC)$) versus shake-off ($P_K(SO)$) for mean β kinetic energy $\overline{E}_\beta$ was first estimated by Feinberg [134]:

$$\frac{P_K(DC)}{P_K(SO)} \approx \frac{B_K}{\overline{E}_\beta}. \tag{6.5}$$

However, recent calculations indicate that the DC mechanism in β^+ decays with endpoint energies of ~1 MeV is 15–20 times larger than this estimate [135, 136]. A comparable enhancement in ^{21}Na would lead to a contribution to K-shell ionization of ≈1%.

In β^+ emitters [137, 138, 139, 140], P_K has been measured over the β energy distribution by detecting K-shell x-rays in coincidence with annihilation γ-rays to discriminate

β^+ from EC decays. We measured the energy dependence of the ion charge-state yields. Any increase in charge-state ratios at low energies in Figure 6.6 could be a signature of direct collisions. Assuming the β energy dependence

$$P_K(DC) \propto \frac{E_\beta^2}{E_\beta^2 - m_e^2} \tag{6.6}$$

predicted by Feinberg [141], the DC mechanism contributes <1.3% to the production of $^{21}Ne^{+2}$ ions, or <4.2% to the ionization of the K-shell, and <4.3% to the production of $^{21}Ne^{+3}$ ions. Calculations indicate that for β decays to the excited-state, internal conversion of the 350 keV γ-ray can be neglected as it leads to additional ionization in $\lesssim$0.007% of excited-state decays [142].

The β^+ energy also gives information about daughter nucleus recoil energy. At intermediate energies the momenta of the β and ν can cancel causing minimal nuclear recoil. The ion ratios in Figure 6.6 are essentially consistent with no recoil ionization, with contributions of 1.3±3.9% and 16±14% respectively. Although these are the first reported limits for β^+ decay, they are not stringent enough for current precision β decay work or to test the predictions of the calculation described below. For this, recoil ionization needs to be measured at the level of $\lesssim$1%.

6.1.6 Trap Population Dependence

We searched for evidence that the number of trapped atoms, which ranged from 100,000 to 500,000, influenced the ionization. The detection rate was proportional to trap population to within the expected ±10% uncertainty. At the highest rates (i.e. largest trap populations), we found the average MCP output (shown in Figure 6.7) decreased by 9±3%, which lead to a 0.4% decrease in $\mathcal{E}_{MCP}$ for ions because the majority of events are above the electronic threshold.

For $^{21}Ne^0$ events, however, the detection efficiency is sensitive to changes in the gain because their pulse height spectrum decreases nearly exponentially above threshold. We assume the pulse height spectrum is described by the function $n(x) = Ne^{-\frac{x}{\sigma_0}}$, where N

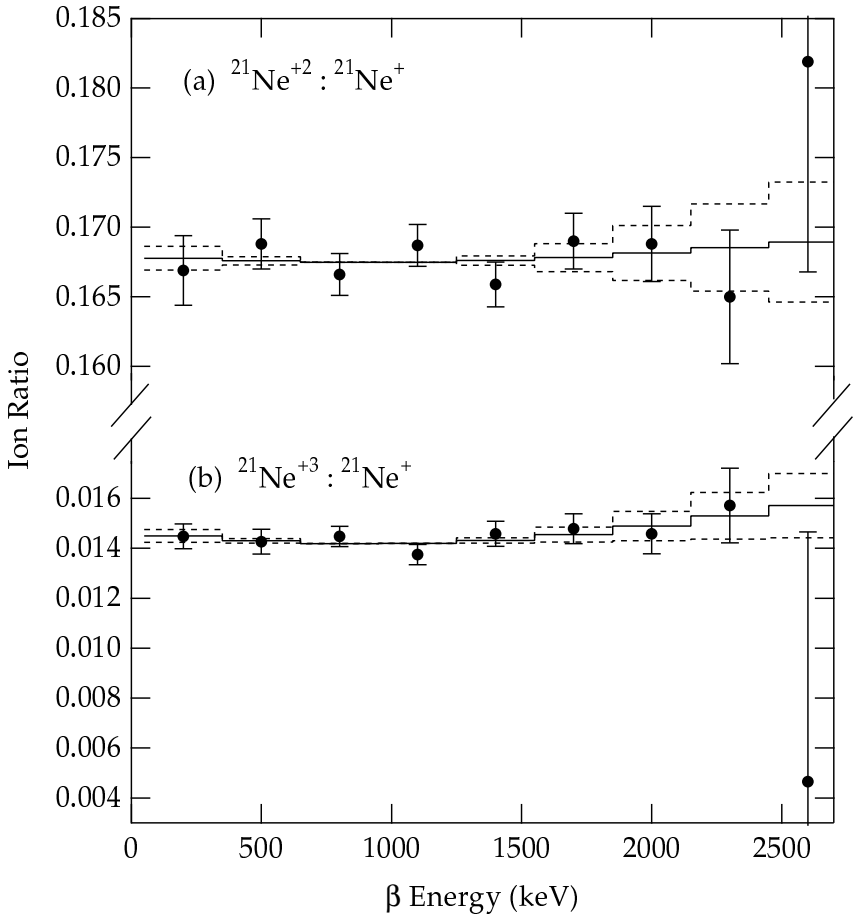

Figure 6.6: Ratio of (a) $^{21}Ne^{+2} : {}^{21}Ne^{+}$ and (b) $^{21}Ne^{+3} : {}^{21}Ne^{+}$ versus total energy deposited in β-detector. Note the scale change between (a) and (b). The energy extends beyond the ^{21}Na endpoint because of interactions between annihilation γ-rays and the scintillator volume. A correction has been applied because the collection efficiency for $^{21}Ne^{+}$ in coincidence with low-energy β^{+}s is less than 100%. A horizontal line would indicate the absence of β and recoil energy influence on ionization. The solid line shows the best fit for recoil ioinization, while the dashed line shows $\pm 1\,\sigma$ fits (for a fixed ratio at 1100 keV). The fits yield 1.3±3.9% and 16±14% for recoil ionization in the ion ratios $^{21}Ne^{+2} : {}^{21}Ne^{+}$ and $^{21}Ne^{+3} : {}^{21}Ne^{+}$, respectively.

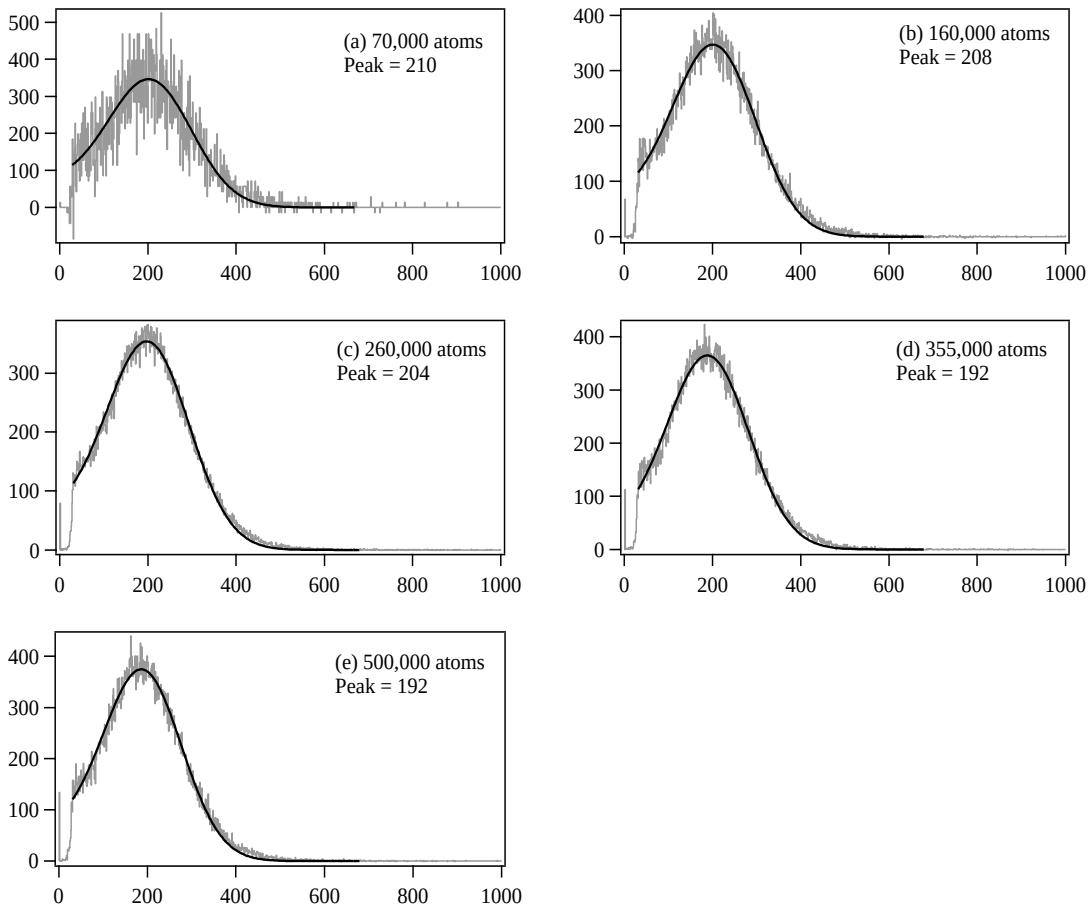

Figure 6.7: MCP pulse height distributions for trap populations of (a) 70,000 (b) 160,000 (c) 260,00 (d) 355,000 and (e) 500,000 atoms. The peak of the distribution decreases by 8% at the largest trap populations.

is the normalization and σ_0 is the decay slope. The number of events above a threshold at x_0 is

$$\int_{x_0}^{\infty} N e^{-\frac{x}{\sigma_0}} dx = N\sigma_0 e^{-\frac{x_0}{\sigma_0}} \tag{6.7}$$

and a fractional change in gain by g leads to a change in the number detected neutrals by

$$\frac{e^{-g\frac{x_0}{\sigma_0}}}{e^{-\frac{x_0}{\sigma_0}}} = e^{(1-g)\frac{x_0}{\sigma_0}}. \tag{6.8}$$

Using the experimentally measured $\sigma_0 = 25 \pm 6$ and $g = 0.91$ between smallest and largest traps, and an electronic threshold at $x_0 = 30$, we find a decrease in neutral detection efficiency of $11\pm4\%$. Comparing this to the ratio of $^{21}Ne^0$ to $^{21}Ne^+$, the detection efficiency change accounts for the decrease in the ratio. After correcting for this effect, the ratio is constant to $-1\pm4\%$.

After correcting for this effect, the charge-state production ratios remain constant regardless of trap population as can be seen in Figure 6.8. Assuming a linear dependence with trap population, we find differences in ion ratios $^{21}Ne^{+2}:{}^{21}Ne^+$, $^{21}Ne^0:{}^{21}Ne^+$, and $^{21}Ne^{+3}:{}^{21}Ne^+$ between smallest and largest traps of $(0.4 \pm 1.5)\%$, $(0.6 \pm 3.0)\%$, and $(2.3 \pm 7.5)\%$, respectively, all consistent with zero. Pulses from the ΔE and E detectors increased by 0.3% and $\approx$1% at the highest rates, due to either pile-up or an increase in output gain. We include this rate-dependence and find that this correction is negligible to both the charge-state distribution and to the $\beta - \nu$ correlation analysis.

6.2 Calculations

The expected charge-state distribution is calculated using the "sudden approximation" as the nuclear charge changes and the nucleus receives a momentum kick from the decay. The overlap between initial and final state orbitals determines the probability the electron will be in that final state orbital. Further ionization results from Auger transitions and accompanying additional shake-off.

The probability of finding an electron (originally in orbital ψ_i of nucleus of charge

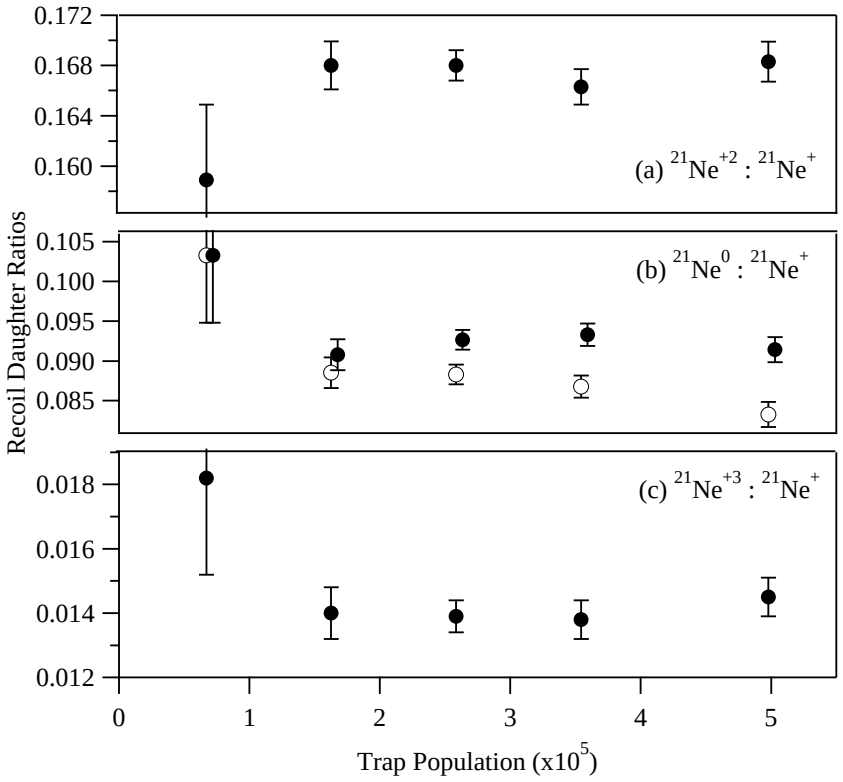

Figure 6.8: Recoil daughter ratios for (a) $^{21}Ne^{+2}:^{21}Ne^{+}$, (b) $^{21}Ne^{0}:^{21}Ne^{+}$, and (c) $^{21}Ne^{+3}:^{21}Ne^{+}$. Note the change in scale for each portion of the Figure. In (b), the white circle represents $^{21}Ne^{0}$ production without correcting for the gain change as a function of rate in the MCP. Applying the correction results in the black circles (which are offset slightly for visual clarity).

Z) in orbital ψ'_f of charge $Z + \Delta Z$ is

$$P_{if}(\vec{k}_r) = |\langle\psi_i|e^{-i\vec{k}_r\cdot\vec{x}}|\psi'_f\rangle|^2 \tag{6.9}$$

where $\hat{k}_r = \frac{\vec{k}_r}{|\vec{k}_r|}$. In the rest frame of the nucleus of mass M, the electrons (of mass m_e) are imparted a momentum of $|\hbar\vec{k}_r| = m_e\sqrt{\frac{2E_r}{M}}$ from a recoil of energy E_r. Usually $\vec{k}_r \cdot \vec{x}$ is assumed to be sufficiently small so that $e^{-i\vec{k}_r\cdot\vec{x}} \approx 1$. However, expanding to first order in $\vec{k}_r \cdot \vec{x}$ gives

$$P_{if}(\vec{k}_r) \approx |\langle\psi_i|\psi'_f\rangle|^2 + |\vec{k}_r|^2|\langle\psi_i|\hat{k}_r \cdot \vec{x}|\psi'_f\rangle|^2. \tag{6.10}$$

The first term is due to orbital mismatch and we use it to calculate the charge-state distribution. The second term is proportional to the recoil nucleus' energy (and is of order $|\vec{k}_r|^2 a_0^2 Z^{\frac{2}{3}} \sim 10^{-3}$ for ^{21}Na) and is used to estimate the magnitude of recoil ionization.

6.2.1 Charge-state distribution

The single electron wavefunctions used for the ground-states of Na and Ne had been calculated using the Roothaan-Hartree-Fock expansion technique [143]. Principle quantum number $n = 3$ orbitals have not been calculated for Ne, so we use $n = 3$ orbitals for Mg to estimate the overlaps with ground-state Na orbitals. As we will find, calculations agree with experimental results only when these overlaps approach zero. In these calculations, electrons not retained in a $n \leq 3$ shell are assumed to go to an autoionizing state or to the continuum and at most one electron in the $n = 3$ shell can be retained — all others are ejected by subsequent Auger transitions. The latter assumption has minimal impact on the results. The initial Ne atomic configuration is generated by determining each electron's final state orbital and limiting each orbital to single occupancy.

Additional ionization can result from rapid ($\lesssim$0.1 ns[144]) Auger processes and associated shake-off. A number of calculations of these vacancy cascades have been performed [145, 131, 146] with results in reasonable agreement with experiment [147]. Combining shake-off and rearrangement ionization determines the charge-state distribution as summarized in Table 6.4. The calculation agrees with data only if all electrons in $n > 2$ shells are

	Including $n=3$		Neglecting $n=3$			Experimetal
Charge	no Auger	Auger [147]	no Auger	Auger [147]	Auger [146]	results
-1	70.18	70.18	0.0	0.0	0.0	0.0
0	22.31	22.31	78.32	78.32	78.32	78.0±3.1
1	6.34	4.74	19.41	17.80	17.99	18.6±2.6
2	1.10	2.02	2.13	3.06	2.98	3.11±0.44
3	0.067	0.60	0.14	0.66	0.60	0.266±0.037
4	0.0023	0.13	0.0056	0.14	0.098	0.024±0.006
5	0.00006	0.022	0.00017	0.023	0.012	0.011±0.006
6	$< 10^{-5}$	0.0030	$< 10^{-5}$	0.0033	0.0014	$\leq$0.010

Table 6.4: Charge-state distribution branching ratios (%), with and without Auger ionization effects. Negative ions would be indistinguishable from neutrals because of the short lifetime.

ejected, although in either case, the production of states with charge $\geq$3 is overestimated. This is not surprising because the Auger ionization probabilities pertain to a single orbital vacancy and are expected to decrease with increasing ionization state.

6.2.2 Recoil ionization

The second term has the form

$$\begin{aligned} P_{if}^{\text{recoil}}(E_r) &= |\vec{k}_r|^2 |\langle \psi_i | \hat{k}_r \cdot \vec{x} | \psi'_f \rangle|^2 \\ &= \frac{2E_r m_e^2}{\hbar^2 M} \left| \sum_n \langle \psi_i | \psi'_n \rangle \langle \psi'_n | \hat{k}_r \cdot \vec{x} | \psi'_f \rangle \right|^2 . \end{aligned} \tag{6.11}$$

Making the approximation $\langle \psi_i | \psi'_n \rangle \approx \delta_{in}$ we find

$$P_{if}^{\text{recoil}}(E_r) \approx \frac{3m_e}{M} \left(\int_{I_P}^{\infty} \frac{df_{osc}}{dE_{if}} E_{if}^{-1} dE_{if} \right) E_r = P_{\text{recoil}}(E_r^{max}) \frac{E_r}{E_r^{max}} \tag{6.12}$$

where $\frac{df_{osc}}{dE_{if}}$ is the differential oscillator strength, E_{if} the energy difference between initial and final states, I_P the ionization potential, and E_r^{max} the maximum recoil energy. This perturbation increases with decreasing binding energy. The percent increase, I_q, in the

production of charge-state q for the highest energy recoils compared to zero energy recoils is

$$I_q = 100 \times P_{if}^{\text{recoil}}(E_r^{max}) \frac{(\Gamma_{q-1} - \Gamma_q)}{\Gamma_q} \tag{6.13}$$

where Γ_q is the branching ratio to ions of charge q.

The calculation is tested against the measured recoil ionization for ^{6}He. Using measured oscillator strengths for Li^+ transitions [148], we obtain $I_{+1} = 0.38\%$. This crude calculation achieves 60% of the experimentally determined value of $0.63 \pm 0.10\%$ [15]. The large nuclear velocities resulting from a decay with a large E_0 and small M enhance the effect.

For ^{21}Na we obtain $I_{+1} \approx 0.6\%$, using measured oscillator strengths for neutral Ne transitions to the continuum [149] and the measured charge-state branching ratios. In general this effect is 4 times larger for singly-charged ions from β^+ decay compared to β^- decay of identical E_0 and M because of smaller branching ratios to positive ions and lower daughter binding energies. Although inconsequential to the charge-state distribution, it is a potentially large systematic effect for β decay correlation experiments currently attaining the 0.01 level and seeking to reach precision of 0.001. An I_{+1} of 1% would lead to a systematic error of $\approx$0.005 in $a_{\beta\nu}$. The results of this calculation for the β^+ unstable nuclei ^{21}Na, ^{38m}K [22], ^{37}K [22], ^{82}Rb [73], and ^{78}Rb [22], (using experimentally determined Ar and Kr oscillator strengths [150]), each of which are currently being trapped for precision β decay studies, are shown in Table 6.5. For one and two electron systems, precise calculations of recoil induced ionization have been performed [121] but no such calculations exist for systems with $\geq$3 electrons. More detailed calculations or precise measurements of recoil ionization will be necessary to interpret the results of future β decay correlation experiments.

Isotope	E_r^{max}(eV)	I_{+1}(%)
^{21}Na	229	0.6
^{38m}K	429	3.1
^{37}K	458	3.4
^{82}Rb	98	1.3
^{78}Rb	103	1.5

Table 6.5: Percent increase in production of singly-charged ions between highest and lowest energy recoils, I_{+1}, for β^+ emitters studied in traps.

6.3 Conclusion

Measurement of the charge-state distribution in ^{21}Na shows $\approx$20% of the decays shake-off $\geq$2 electrons, leading to positive ions, compared with only $\approx$5% of β^- decays in which 2 or more electrons are lost. This is fortuitous for experiments that detect positive daughter ions. At the current level of precision ($\approx$0.01 for the $\beta - \nu$ correlation), the level of independence of the charge-state distribution from the β and recoil-ion energies are sufficient. However, a rough calculation indicates that the influence of the nuclear recoil on the ionization process cannot be ignored for measurements of β correlations using β^+ emitters surpassing the level of 1% and needs to be studied further. For β^- emitters, however, the effect is smaller since all decays result in positive ions. For β^+ decays that yield stable negative ions, such as ^{19}Ne [151], the impact of recoil ionization is uncertain because of the competing effects of a large branching ratio to negative ions and small orbital binding energies. The β energy dependence of ionization is small ($\lesssim$1%) as expected in ^{21}Na but could be significant for decays with low Q-values or high Z.

Chapter 7

Results for the $\beta - \nu$ Correlation

7.1 Trap Distribution and Position

The spatial distribution of atoms in the trap is determined by imaging the fluorescence on a CCD camera with viewing angle indicated in Figure 7.1. Along the y'- and z-axes, the trap distribution is described by a Gaussian with the width approximately equal in each dimension. The distributions in Figure 7.2 show the spatial profiles and Gaussian fits for a trap of 200,000 atoms. The FWHM was 0.80±0.08 mm, regardless of trap population. The camera scale and FWHM resolution of 0.22±0.08 mm were determined off-line by imaging a ruler placed at the chamber center. The $\beta - \nu$ correlation analysis is most sensitive to the distribution along the x-axis, so a single camera with a view along the y'-axis proved sufficient. Uncertainty in the trap dimensions are dominated by variations during the run, and not from assuming the widths are equal in each dimension. Including the slight asymmetry in the trap populations at the wings of the Gaussian causes a change in $a_{\beta\nu} < 0.001$ and was neglected in the analysis.

The trap centroid moved less than 0.1 mm over the 40 hour runs. The TOF of the fastest $^{21}Ne^{0}$ recoils allows a precise measurement of the trap position along the x-axis. We fit the rising edge of the data shown in Figure 7.3 to a Monte Carlo simulation. We were able to determine the timing of the rising edge to ±1 ns which determines the trap-to-MCP distance to be 83.08±0.04 mm (83 mm is the distance from armature center to MCP). This

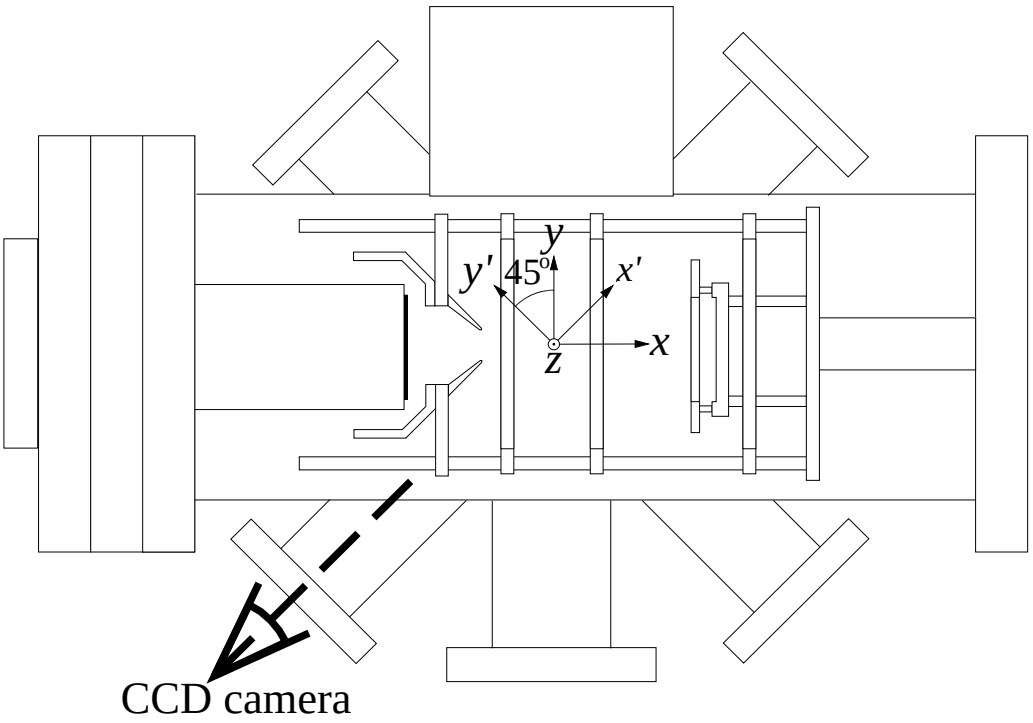

Figure 7.1: CCD camera view of the trap and axes referred to in text. The atomic beam enters the chamber along the $+z$-axis and the trapping laser beams are directed along the y-axis and in the x-z-plane, rotated $\pm 45°$ off the z-axis.

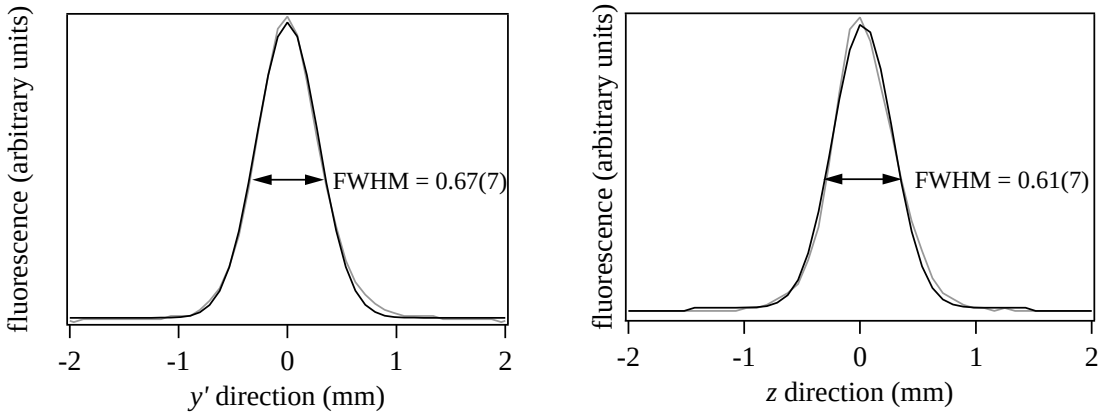

Figure 7.2: Trap density for 200,000 atoms during the August 2001 Run. The gray curves are the measured trap fluorescence and the black curves are the Gaussian fit.

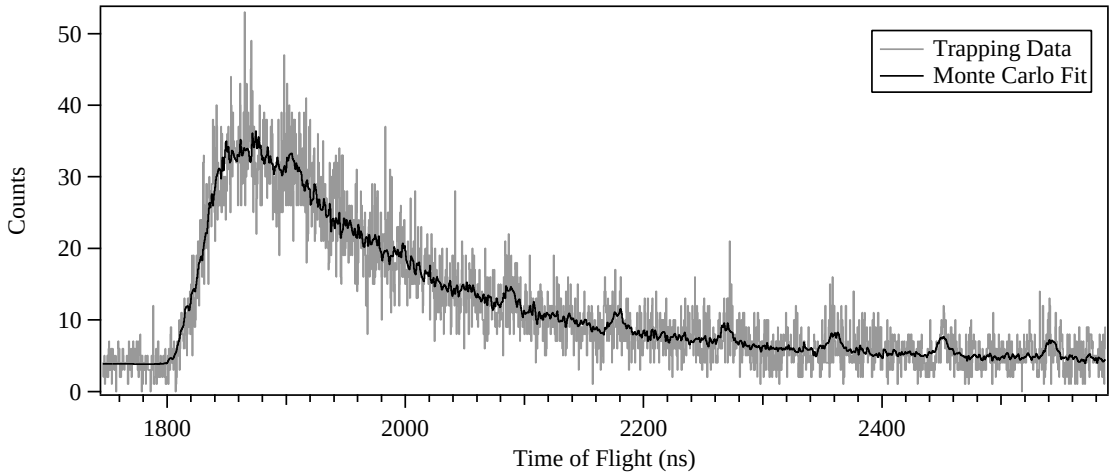

Figure 7.3: Neutral time-of-flight spectrum from the August 2001 Run after making appropriate data cuts ($E_\beta > 1550\,\mathrm{keV}$ and MCP pulse heights < ADC channel 80) to bolster the signal-to-noise. The trap-to-MCP distance was $83.08 \pm 0.04\,\mathrm{mm}$.

result is independent of any assumptions about the trap distribution or MCP detection efficiency. The positions in y'- and z-axes were determined from CCD camera images. The center of the electrode armature in the images was determined off-line by viewing wires that crossed at the chamber center. Wires on the ports help line up the camera during and after off-line calibrations. In conjunction with the trap-to-MCP distance, we find the trap location is $0.5 \pm 0.4\,\mathrm{mm}$ from the electrode armature center.

Past research with MOTs have indicated that it is possible to maintain a diffuse halo of loosely trapped ^{21}Na atoms that surround the trap [152]. A halo density of 10^{-3} that of the trap would not be observable on the CCD camera, but with a radius $10\times$ that of the trap it would contain half the population. By examining the recoil-ion TOF region between the $^{21}Ne^{+}$ and $^{21}Ne^{+2}$ peaks, we infer that <0.5% of the population resides in such a halo. This has no significant effect on the $\beta - \nu$ correlation measurement.

7.2 $^{21}Ne^0$ Data

Although ≈80% of the daughters are $^{21}Ne^0$ and systematic uncertainties associated with the electric field are eliminated for these events, they yield minimal information on the $\beta - \nu$ correlation because of uncertainties in the detection efficiency. Only 18.5±0.1% reach the MCP with energies of <230 eV. For neutrals and ions with kinetic energy $\lesssim$2 keV, $\mathcal{E}_{MCP}$ increases nearly linearly with energy [128, 129, 153, 154, 155]. Neutrals hit the MCP at angles up to 15°, and MCP gain decreases for angles >5° relative to the microchannel axis [102]. In addition, the CsI coating on the MCP should provide nearly uniform detection efficiency for all atomic metastable neutrals, $^{21}Ne^*$, regardless of energy, because of UV photon emission upon impact. We include a small, energy-independent contribution to $\mathcal{E}_{MCP}$ based on expected $^{21}Ne^*$ production.

We determined the intrinsic MCP detection efficiency for $^{21}Ne^0$ to be 6.1±0.8% from their 78.0±3.1% branching ratio, determined earlier by subtracting the ion branching ratios from the total. The detection efficiency is consistent with results in Ref. [155] for $^{16}O^0$. For the $\beta - \nu$ correlation, we assume the energy dependence increases linearly from 0.6% at 0 eV to 7.0% at 230 eV. We include a systematic uncertainty of ±25% (equivalent to neglecting the energy independent term) because neither the $^{21}Ne^*$ production nor their energy dependence was independently verified. We assume the spatial and angular variation in gain is proportional to that of the $^{20}Ne^+$ from the ion beam calibration, causing the relative detection efficiencies to be 55% smaller at the edge than at the center. This effect is large because few neutrals yield pulses above the discriminator threshold. We assume this description is accurate to 25%, giving us a systematic uncertainty of ±0.05. We find $a_{\beta\nu} = 0.51 \pm 0.06(\text{stat}) \pm 0.15(\text{syst})$, which is consistent with the Standard Model. The large systematic uncertainty results primarily from the spatial, angular, and energy dependence in $\mathcal{E}_{MCP}$ [102].

7.3 Electronics and Timing

The timing offset and resolution is accurately determined by the nearly simultaneous triggers from both detectors by βs that backscatter from the MCP into the β-detector. Since the measured FWHM of this peak is only 0.85 ns, the timing resolution of the data acquisition must be <0.85 ns. We include a timing convolution of 0.85 ns to the Monte Carlo simulation, but it is dwarfed by the time-of-flight spread of 7 ns due to the spatial extent of the trap. The backscatter peak has a TOF of -0.6 ns determined by the distance between MCP and β-detectors (after removing the common 0.3 ns β^+ flight-time from trap to β-detector), and is used to set the timing offset. The measured non-linearity of the data acquisition system leads to an uncertainty in $a_{\beta\nu}$ of <0.001. Over the course of the run, the pedestal for the TOF spectrum drifted by 0.5 ns, as indicated by the shift in position of this backscattered peak. This drift was removed and was probably due to temperature fluctuations during the run.

7.4 Backgrounds

7.4.1 TOF Spectrum Of Background Runs

Part of the run was dedicated to determining backgrounds. Conditions were identical to the trapping runs except that the trapping laser beam along the y-axis was blocked so no atoms were trapped. Figure 7.4 shows the TOF spectrum from these background runs. Aside from accidental coincidences which have a nearly uniform TOF distribution, the only structure is the peak from backscattered βs and a set of peaks occuring at 90 ns intervals. These peaks are from the pulsed Cyclotron proton beam and appear in both recoil-ion data and background data since they were both collected with the beam continuously on target. They are described with a periodic Gaussian function and subtracted from the recoil-ion data.

We collected data with the proton beam on target because these background peaks have a negligible impact on the $\beta-\nu$ correlation analysis. If we had pulsed the proton beam

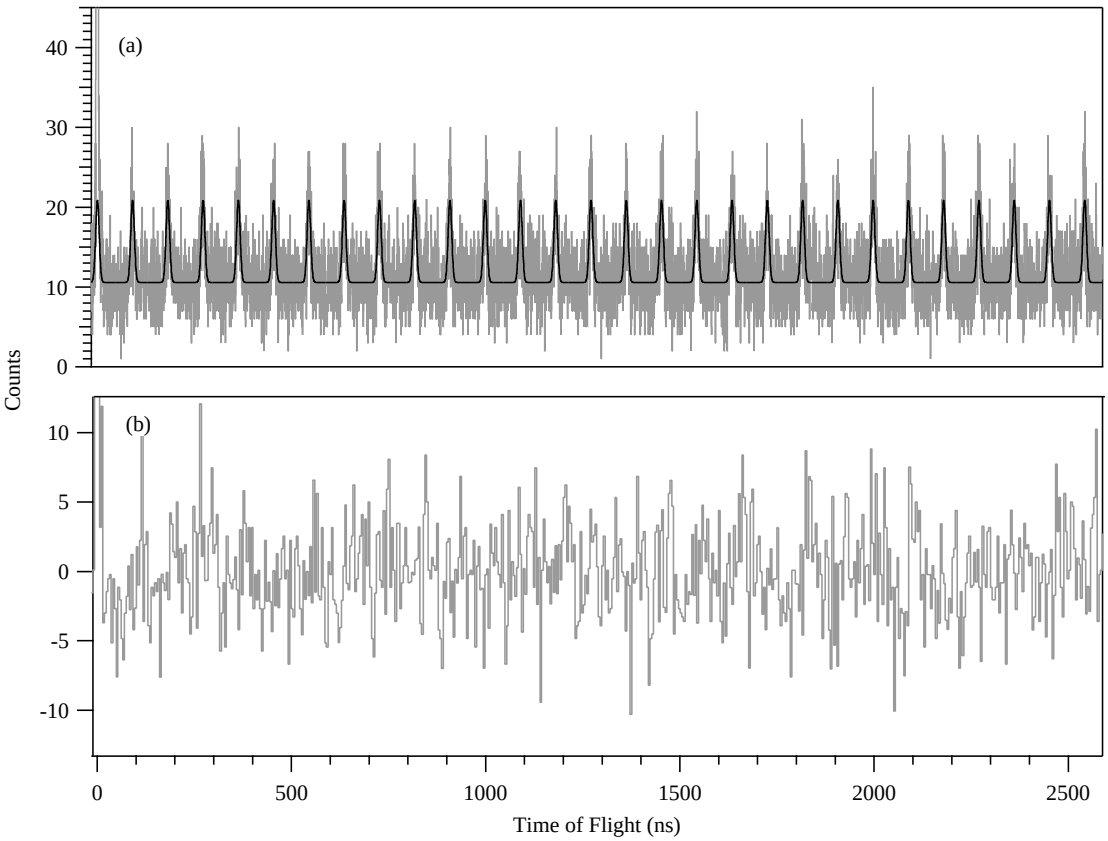

Figure 7.4: Time-of-flight spectrum for (a) the background runs with a periodic Gaussian fit and (b) the background (with bins ten times wider) after subtracting off a flat background and periodic Gaussian fit. The $^{21}Ne^{+}$ recoil-ion peak, binned as in (b) would begin at 590 ns and have a peak height of about 25,000 counts.

and accumulated data only when the beam is off, these peaks would have been eliminated but the statistics would have been reduced by roughly a factor of 3 (a factor of 2 for the duty cycle, and a factor of 1.5 from decreased trap population).

The absence of additional peaks in the TOF distribution indicates that few coincidences result from untrapped activity. In particular, the atomic beam gives rise to no significant number of coincidences nor does activity stuck on electrodes, the collimator, the MCP, or chamber walls. These events would each have characteristic TOF peaks that would fall under the ion peaks.

7.4.2 γ-ray Backgrounds

A correction is made for annihilation γ-rays that deposit energy in the ΔE β-detector. The detection efficiency of the ΔE detector is estimated to be 4.3% of that of the E detector, based solely on the scintillator volumes. The TOF spectrum for these events is difficult to calculate accurately because β^+ from the trap can annihilate anywhere in the chamber. A Monte Carlo simulation was performed assuming each β^+ annihilates on the first surface it encounters and radiates annihilation γ-rays isotropically. These γ-rays propagate without attenuation, and events that intersect the β-detector are accepted. Based on this simple simulation and the detection efficiency of the ΔE for 511 keV γ-rays, we estimate 1.0$\pm$0.5% of the data set results from $\gamma-{}^{21}$Ne coincidences.

We obtain the TOF spectrum for γ-ray coincidences on-line from events that deposit energy in the E detector but not the ΔE detector. We apply the same energy threshold in the E as in the ΔE detector and scale the spectrum by the relative detection efficiency of the ΔE and E detectors to 511 keV γ-rays. This estimate implies γ-rays cause 1% of the ΔE triggered coincidences. The TOF spectrum for these events is shown in Figure 7.5 (a). The periodic noise from the cyclotron beam are subtracted because the timing resolution for E-MCP coincidences (1.75 ns) is larger than that of ΔE-MCP coincidences because of the LeCroy Model 222 gate/delay generator. We fit the region 1150–2500 ns with a periodic Gaussian function and a flat background. Keeping the parameters of the periodic Gaussians

fixed, we allow the flat background level to vary from 10–300 ns and find it is 6% smaller (most likely due to deadtime effects). To subtract the background under the ion peaks, we fix the periodic Gaussians and linearly increase the background from 600–1150 ns. Although this does not properly account for the shape of the background under the ion peaks, in practice, the small change in background level has a negligible effect on the results. Shown in (b) of Figure 7.5 is the time-of-flight spectrum using in the analysis from $\gamma-^{21}$Ne coincidences after removing the accidental coincidences and periodic noise. Figure 7.5 (c) shows the energy deposited inthe E detector is peaked at $\approx$340 keV, as expected for these events. Although the decay of the excited-state, inner bremsstrahlung, and EC to excited-states also trigger the ΔE detector, they are not prevalent enough to be of significance.

The $\gamma-^{21}$Ne spectrum extends beyond kinematically allowed TOFs for β^+-^{21}Ne events since the ion recoil is not as biased toward the MCP. By fitting the magnitude of this contribution for TOF$>$850 ns, we find a contribution of 1.05$\pm$0.23% from these γ-ray induced coincidences, in agreement with expectations. We use this value and uncertainty in the analysis. The measured $\gamma-^{21}$Ne TOF spectrum in Figure 7.5 (b) is included in the fit and causes a correction to $a_{\beta\nu}$ of 0.0085$\pm$0.0018 for the $^{21}Ne^+$ data and 0.0098$\pm$0.0021 for the higher charge-states. The correction is smaller for $^{21}Ne^+$ coincidences because the electric field does not draw all $^{21}Ne^+$ recoils to the MCP active area, but draws all of the higher charge-states.

7.4.3 Pile-Up

We estimate the fraction of β^+-^{21}Ne coincidences in which separate decays deposit energy in the scintillators. Summing the energies allows lower energy β^+s to rise above threshold. This problem is minimized by the low-energy threshold. Figure 7.6 shows the time difference, $\Delta t = t_{\Delta E} - t_E$, for each coincidence where $t_{\Delta E}$ (t_E) is the time between MCP and ΔE (E) detector triggers. We find 98% of the Δt values in the range -20 ns$< \Delta t <$50 ns and estimate 0.05% of the events in this range are the result of pile-up. The range is broad because of non-linearities in the ΔE and E TOF measurements near

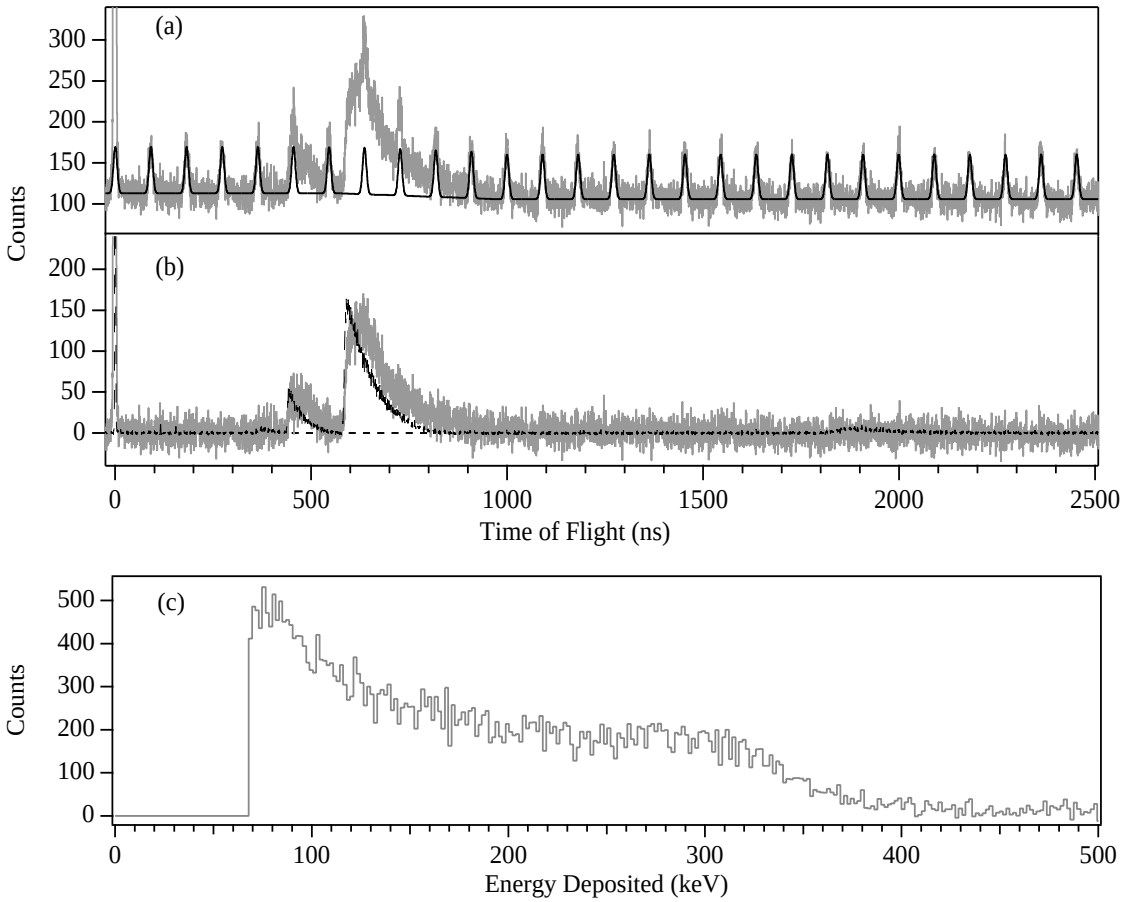

Figure 7.5: Time-of-flight for events that deposit energy in the E detector but not the ΔE detector (in gray) in (a) along with periodic Gaussian from cyclotron proton beam (in black). In (b) these periodic spikes and flat background have been subtracted leaving the time of flight spectrum for $\gamma - ^{21}$Ne events. Overlayed (in dashed black) is coincident $\beta^+ - ^{21}$Ne data rescaled for comparison. In (c), the energy deposited in the E detector for γ-ray events.

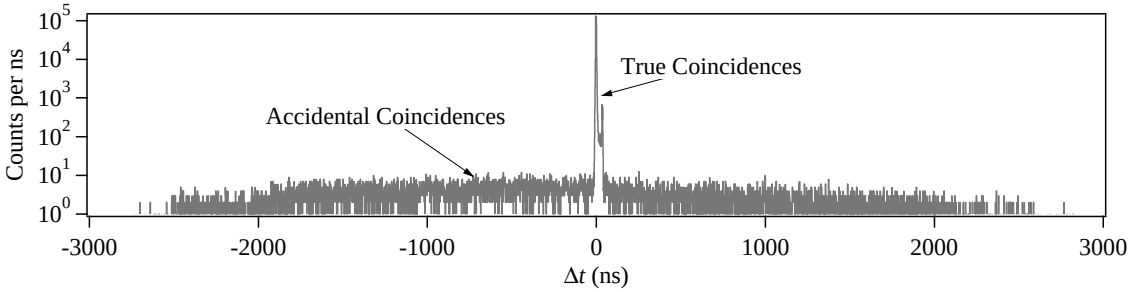

Figure 7.6: Number of events at each Δt.

2600 ns and this part of the spectrum is not used in the $a_{\beta\nu}$ analysis. Outside this Δt range, the β energy is determined solely from the ΔE scintillator signal.

Cross-talk between cables for the ΔE and MCP detectors caused the largest 0.3% of ΔE signals to occasionally trigger the MCP at a few characteristic TOFs: 36, 119, and 157 ns. These events do not fall in the ion TOFs of interest and are removed from the data set by cutting the highest channel in the ΔE spectrum. This cut had a negligible effect upon the ion spectra. The problem was later eliminated by running the cables for the ΔE and MCP detectors in separate cable trays.

7.4.4 Atoms Lost from the Trap

Additional backgrounds can result from ^{21}Na atoms that decay as they escape from the trap. For a trap with a lifetime of 12 s containing 500,000 atoms, a steady-state loss of $\approx$50,000 atoms/s is expected, including 17,000 atoms/s of decays and 35,000 atoms/s escaping from the trap. Atoms emerging at the average trap temperature of $\sim$150 μK take $\sim$150 ms to reach the chamber walls. At steady-state, 5,000 atoms form a diffuse gas within the vacuum chamber. Calculations indicate that for decays from this gas, the average geometric efficiency for the β detetor is 0.033%. We expect at most 0.04% of recoil-ion coincidences to be from atoms lost from the trap.

Similar arguments indicate that coincidences from atoms in the slowed atomic beam are negligible. Decays from the uncooled atoms in the beam have a line-of-sight to

Contributions to double scattering from the collimator	Fractional probability
Ω of chamber with line-of-sight into collimator opening	0.4
Backscatter off stainless steel chamber	0.25
Ω of collimator through collimator hole	0.0025
Backscatter off collimator	0.25
Ω of β-detector	0.20
Resulting double scattering probability	1.25×10^{-5}

Table 7.1: Probability of double scattering involving the interior of the collimator.

the β-detector for only $\lesssim 100\mu$s. Only 3×10^{-6} of the atoms decay in this time period, and these decays can be neglected. For the slowed atoms, about 25% are trapped. With observed loading rates of $\approx$50,000 atoms/s, we expect 200,000 atoms/s in the slowed atomic beam. These atoms spend $\gtrsim$100 ms in view of the β-detector, giving an average population of 20,000 atoms. The β-detector solid angle for these atoms is $< 0.01\%$ of 4π. We expect $<0.5\%$ of the decays originate in the atomic beam, consistent with direct observation.

7.4.5 Multiple Scattering

The backgrounds from β^+ that scatter once before hitting the β-detector are taken into account in the TOF spectra corresponding to backscattering off the MCP and scattering off the lip of the collimator. The collimator restricts the direct line-of-sight from any other surfaces. Events that scatter twice reach the β-detector only if the second surface is the interior of the collimator or the MCP. Table 7.1 and Table 7.2 give a rough estimate ($\pm50\%$) for the size of these backgrounds. The contribution from these events is only 0.14% of the total, leading to a 0.001 ± 0.001 correction to $a_{\beta\nu}$. The contribution from events that scatter more than twice can be neglected.

7.4.6 Stopping of β's in the Collimator

The heavy metal collimator is thick enough to stop all β^+'s from ^{21}Na decay. However, occasionally when a β^+ or annihilation γ-ray interacts with the collimator, an

Contributions to double scattering involving the MCP	Fractional probability
Ω of chamber with line-of-sight to MCP	0.8
Backscatter off stainless steel chamber	0.25
Average Ω of MCP from chamber surfaces	0.01
Backscatter off MCP front face	0.15
Ω of collimator opening	0.003
Resulting double scattering probability	9×10^{-7}

Table 7.2: Probability of double scattering involving the MCP.

Contribution to e^- detection from β^+'s hitting collimator	Fractional probability
Ω of collimator from trap	0.08
Electron released on inner side of collimator	0.001
Average Ω of β-detector	0.15
Resulting detection probability	1.2×10^{-5}

Table 7.3: Probability of detecting low-energy electrons from β's stopped in the collimator.

electron knocked from the inner surface reaches the β-detector. Calculations using EGSnrc indicate that for 1 MeV β^+'s entering the heavy metal collimator, an electron emerges on the other side of the collimator 0.1% of the time. Table 7.3 summarizes the contribution from this type of event. Similarly, γ-rays that enter the collimator have only a 0.1% chance of giving a Compton scattered electron. The contribution is summarized in Table 7.4. Together these events contribute about 0.3% of the events and necessitate a 0.0022 ± 0.0017 correction to $a_{\beta\nu}$.

7.5 Polarization and Alignment of the Trap

Since ^{21}Na has a nuclear spin of 3/2, the nuclei in the trap can have polarization or alignment. The $F = 2$ ground-state is a stretched state, so polarization or alignment of the angular momentum is equal to polarization or alignment of the nuclear spins. We do not expect net a polarization, but the MOT is a complicated system with circularly-polarized

Contribution to e^- detection from γ-rays hitting collimator	Fractional probability
Ω of collimator from chamber surfaces	0.10
Electron released on inner side of collimator	0.001
Average Ω of β-detector	0.15
Resulting detection probability	1.5×10^{-5}

Table 7.4: Probability of a Compton scattered electron reaching the β-detector from interaction with annihilation γ-rays.

light from three pairs of directions sitting an inhomogenous (although small) DC magnetic field. Net alignment is more plausible due to sub-Doppler cooling mechanisms present in a MOT. This is difficult to calculate, and no previous research is available so we analyzed the data for evidence of alignment. We also did an optical rotation experiment to measure the polarization and alignment of a stable ^{23}Na trap.

7.5.1 Polarization

The vacuum and electrode system has near perfect mirror symmetry in each plane that intersects opposite pairs of electrode support rods. The symmetry is broken by the 45° rotation of these rods relative to the vacuum flanges. This symmetry cancels any kinematic effect due to a polarization along the y- or z-axes, leaving the x-axis (see Figure 7.1) as the only polarization direction to be concerned about. In this direction, the β-asymmetry term ($A_\beta = 0.862$) and the ν-asymmetry term (B_ν=0.597) mimic the kinematics of F_1 and $a_{\beta\nu}$ (see Figure 7.7) and even have similar coefficients. This suppresses the effect of a non-zero polarization in this direction and Monte Carlo simulations indicate that a 10% residual polarization results in a shift of 0.0167 in $a_{\beta\nu}$.

The only evidence in the recoil-ion data that can be used to limit the polarization comes from comparing the rate of ion coincidences relative to the number of atoms in the trap. Although this tells us nothing about a net polarization in all traps, it does limit the polarization dependence on trap population. If a polarization were directed into (away from) the β-detector, the count rate per atom would increase (decrease) because of the

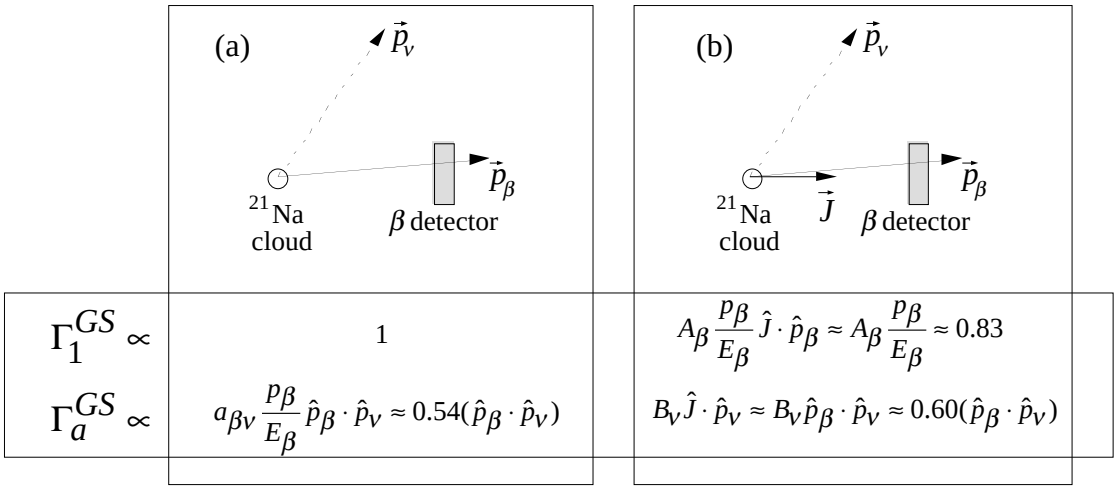

Figure 7.7: Kinematics for $\hat{J}$ directed at the β-detector and similarities to Γ_1^{GS} and Γ_a^{GS} terms.

correlation between $\vec{p}_\beta$ and $\vec{J}$. The number of ions in the $^{21}Ne^+$ peak relative to the trap population is constant to $\pm 20\%$. This indicates the polarization changes less than 25% (and causes a shift in $a_{\beta\nu} < 0.045$) from smallest to largest traps. Unfortunately, this limit is not very restrictive.

7.5.2 Alignment

The tensor alignment term, being quadratic in J, does not get suppressed by symmetry. Sub-Doppler cooling mechanisms are known to contribute in MOTs containing Cs [156] and Rb [157] atoms. One-dimensional descriptions of these cooling mechanisms for counterpropagating σ^+-σ^- polarized beams have been shown to induce large alignments along the direction of the laser beams [158]. For Na, steady-state populations in the hyperfine $F = 2$ ground-state have an alignment of 60% [159]. In the three-dimensional case, the polarization gradients are more complicated and little is known about the cooling mechanism (and therefore alignment). If each orthogonal pair of laser beams were to induce an alignment of the same magnitude, the net alignment of the sample would be zero by symmetry. However, the laser power is not balanced (the beam along the y-axis requires

much less power because of a steeper magnetic field gradient) so it is unclear what kind of alignment to expect.

The kinematic correlation proportional to c_{align} is similar to Γ_a. Monte Carlo simulations indicate that a 10% alignment along the horizontal or vertical beam axis give shifts in $a_{\beta\nu}$ of 0.0156 or 0.0095, respectively. There is no unique signature in the recoil-ion data that would indicate an alignment was present. A weak limit on the population dependence of the alignment is obtained by comparing the counts in the $^{21}Ne^0$ and $^{21}Ne^+$ peaks. The presence of a non-zero alignment alters the correlation between nuclear recoil and β^+ emission, changing the number of neutral recoils that reach the MCP. The data in Figure 6.8 show that the alignment changes by less than 30% over the range of trap populations. A more reliable way to study tensor alignment is to make a direct measurement using an optical rotation technique described below.

7.5.3 Optical Rotation Measurement

We performed an optical rotation measurement to establish the net polarizaton or tensor alignment. Since useful optical rotation signals required $> 2 \times 10^6$ atoms, we trapped stable ^{23}Na using the identical trap configuration. The technique is illustrated schematically in Figure 7.8 (a). A 40 μW probe beam with a 1 mm diameter passed through the trap along the y'-axis of Figure 7.1. The probe beam polarization oscillated from σ^+ to linear to σ^- to linear (perpendicular to the previous linear polarization) at a frequency $\omega = 50$ kHz using a photo-elastic modulator (PEM) and is illustrated in Figure 7.8 (b). After passing through the trapped atoms, the beam was detected with photodiodes and the absorptivity demodulated at 1ω and 2ω using a lock-in amplifier. The optical depth was determined by the DC absorption of the probe beam. The probe beam frequency was swept at 35 MHz/s through the atomic transitions.

The resulting lineshapes for transitions from the $F = 1$ and $F = 2$ hyperfine ground-states are shown in Figure 7.9. These measurements were sensitive to polarizations and alignments in both the ground- and excited-states. Without a magnetic field, a sample

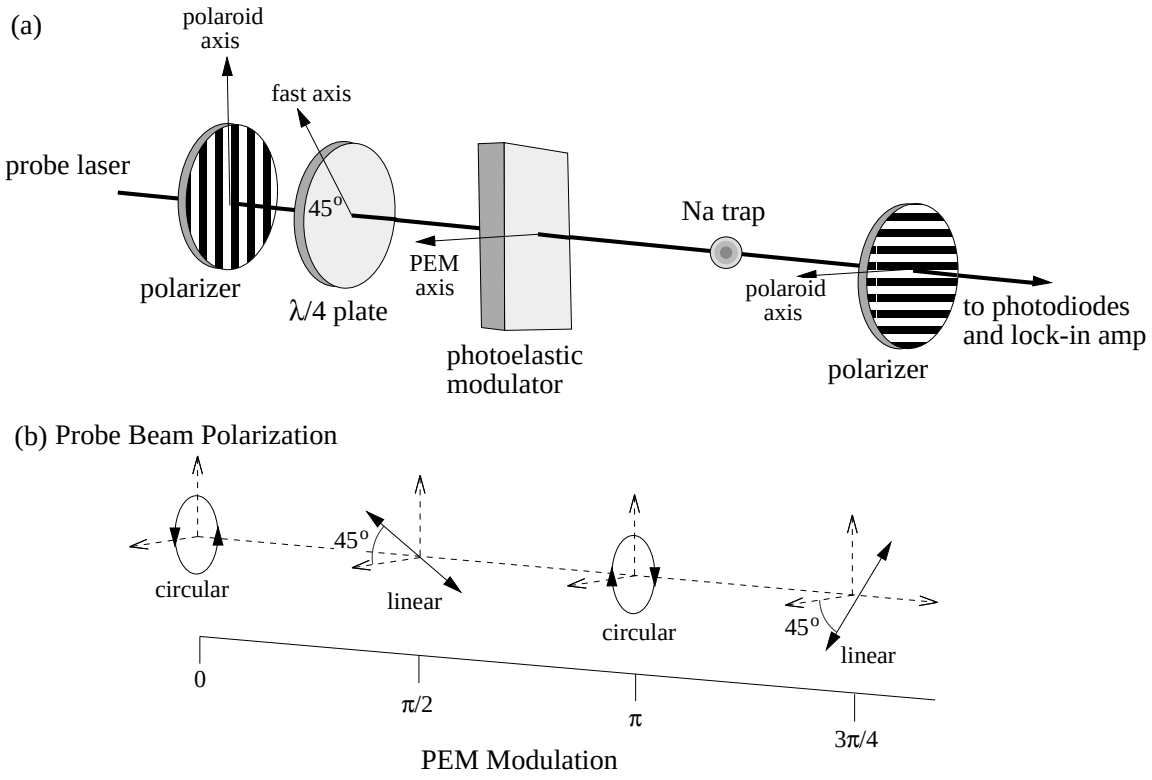

Figure 7.8: (a) Optical rotation schematic and (b) polarization modulation for measuring polarization and alignment in a ^{23}Na trap.

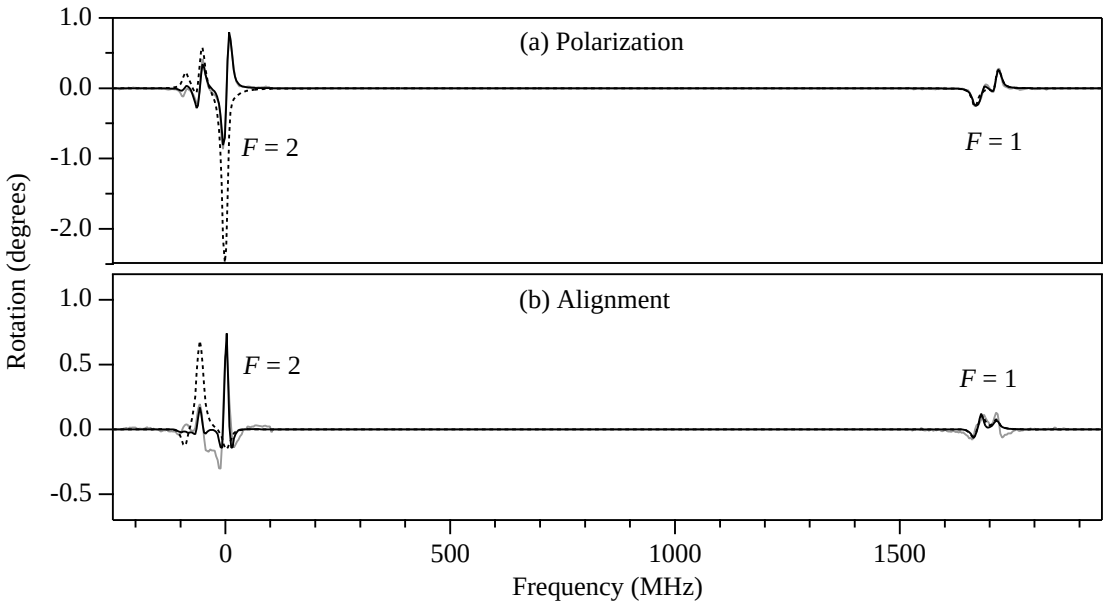

Figure 7.9: Optical rotation signal demodulated at (a) 1ω and (b) 2ω. The frequencies are relative to the $3S_{1/2}(F = 2) \rightarrow 3P_{3/2}(F = 3)$ transition. The gray curve is the data and the black curve is a simultaneous fit to the data in (a) and (b). The dashed lines correspond to the expected signal for (a) a polarization of 1% in the $F = 2$ ground-state and (b) an alignment of 1% in the $F = 2$ ground-state.

with no net polarization or alignment gives no signal. However, for an unpolarized sample in a non-zero magnetic field, the lineshape at 1ω should be antisymmetric because of the Zeeman shift of the different m_F levels. For an unaligned sample, the lineshapes at 2ω should be symmetric, although an alignmented sample can also produce a symmetric lineshape.

We determined the net polarization and tensor alignment of the nuclear spin in samples as small as 10^6 atoms are both <0.2% by comparing the data to lineshapes calculated for different hyperfine sublevel population distributions. These conclusions were independent of electric/magnetic field settings, alignment and power in the trap laser beams, number of atoms in the trap, and portion of the trap probed. The Doppler width of the peaks indicate the temperature of the trapped atoms is $\lesssim 150\,\mu$K.

Charge	Excited branch change (%)	Correction
0	-0.0075	-0.00011
$+1$	-0.006	-0.00008
$+2$	0.14	0.0020
$+3$	0.81	0.011
$+4$	5.7	0.078

Table 7.5: Change of excited-state branching ratio contribution due to internal conversion of the 350 keV γ-ray.

7.6 Ionization Dependences

Since the $\beta - \nu$ correlation is measured only for daughter ^{21}Ne that have lost $\geq$2 electrons, the ionization process could lead to systematic effects. As discussed in Ref. [118], the ratios $^{21}Ne^{+2}:{}^{21}Ne^{+}$ and $^{21}Ne^{+3}:{}^{21}Ne^{+}$ show no indication the β or recoil ion energy influences the ionization process. At β^+ energies $\lesssim$400 keV, 5% of $^{21}Ne^{+}$ miss the MCP active area. The size of this effect implies the MCP active area diameter is 44.08$\pm$0.30 mm, in agreement with the specified 44 mm. A rough calculation indicates that nuclear recoil should increase ionization for the fastest recoils by 0.70$\pm$0.35% [118] and we apply a correction of -0.0033 ± 0.0017 to $a_{\beta\nu}$.

Internal conversion (IC) of the excited-state γ-ray causes the excited-state contribution in each charge-state to deviate from the β decay branching ratio. Using IC coefficients computed as a function of γ-ray energy using relativistic atomic wavefunctions and a finite nuclear radius [142], IC is calculated to contribute a negligible correction to the $^{21}Ne^{+}$ data. Electron loss following inner shell vacancies was incorporated using the results of Ref. [131]. Although the correction increases rapidly with charge-state (see Table 7.5), the majority of the data is in the $^{21}Ne^{+}$ peak.

7.7 Results and Systematic Uncertainties

The Monte Carlo generated fit to the over 600,000 coincident $\beta-^{21}$Ne events is shown in Figure 7.11. The only free parameters in the fit are $a_{\beta\nu}$, the number of ions in each peak, and the magnitude of the flat background. The fit gives

$$a_{\beta\nu} = 0.5243 \pm 0.0066 \pm 0.0049 \pm 0.0041 \tag{7.1}$$

where the first uncertainty is statistical, the second systematic, and the third from the decay properties. The decay property uncertainty is dominated by uncertainty in the excited-state branching ratio, $\mathcal{B}_{ES}$. Table 7.6 is a summary of systematic uncertainties for $^{21}Ne^{+}$. Results for the charge-states 0–4 is shown in Table 7.7.

The consistency of the recoil-ion data with previous measurements of $\mathcal{B}_{ES}$, was checked by setting $\mathcal{B}_{ES}$ as free parameters along with the ground-state $a_{\beta\nu}$. The excited-state $\beta-\nu$ correlation coefficient, $a_{\beta\nu}^{ES}$, was also measured by fixing $\mathcal{B}_{ES}$ and allowing both $\beta-\nu$ correlation coefficients to vary. The results,

$$\mathcal{B}_{ES} = 4.3 \pm 1.6\% \qquad \text{and} \qquad a_{\beta\nu}^{ES} = -0.17 \pm 0.27 \tag{7.2}$$

(quoted with only statistical uncertainties), are consistent with the measured branching ratio and prediction of $a_{\beta\nu}^{ES} = -1/3$. Agreement of the ground-state decay $\beta-\nu$ correlation with the Standard Model occurs at $\mathcal{B}_{ES} = 6.3\%$. Although the currently accepted value is $\mathcal{B}_{ES} = 5.02 \pm 0.13\%$ [160], Figure 7.10 shows there are large disagreements between measurements [38, 39, 40, 41, 42]. A possible cause for these disagreements is the presence of β^{+}-emitting contaminants which would lower the measured branching ratio and explain the discrepencies. We believe it is important to accurately determine $\mathcal{B}_{ES}$ before making conclusions about the Standard Model.

Results given for fits in which the Fierz interference term, b_{Fierz}, and the weak magnetism term, b, are free parameters are summarized in Table 7.8. The induced tensor term, d, does not give any energy dependence to F_1 or $a_{\beta\nu}$ so limits can only be obtained by comparing the measured $a_{\beta\nu}$ with the Standard Model prediction. We find $d \lesssim 190$.

Source	Correction	Uncertainty
Recoil order corrections	-0.0001	
Z-dependent radiative corrections	-0.0010	
Z-independent radiative corrections	$+0.0041$	
Recoil ionization	-0.0034	0.0017
Polarization and alignment		0.0006
Physics total	-0.00024	0.0018
Annihilation γ-rays	$+0.0085$	0.0018
Backscattered β^+s	$+0.0017$	0.0008
Collimator tip scattering	$+0.0011$	0.0008
Multiple scattering	$+0.0011$	0.0011
Background level		0.0003
Decays from collimator tip		0.0004
Background total	$+0.0124$	0.0025
Event timing		0.0003
Electric field		0.0016
Trap-to-MCP distance		0.0011
Trap location		0.0015
Trap radius		0.0010
Deadtime		0.0001
Simulation total		0.0027
Be window energy loss		0.0015
β-detector position		0.0017
β energy threshold		0.0007
β-detector total		0.0024
$\mathcal{E}_{MCP}$ energy dependence	-0.0005	0.0002
$\mathcal{E}_{MCP}$ position dependence	-0.0034	0.0011
MCP diameter		0.0011
MCP uncertainty total	-0.0038	0.0016
TOTAL	$+0.0083$	0.0049

Table 7.6: Corrections and systematic uncertainties.

Charge	$a_{\beta\nu}$
0	$0.51 \pm 0.06 \pm 0.15$
+1	$0.5243 \pm 0.0066 \pm 0.0064$
+2	$0.5207 \pm 0.0118 \pm 0.0076$
+3	$0.5644 \pm 0.0643 \pm 0.0242$

Table 7.7: $\beta - \nu$ correlation coefficient for the charge-states 0–3. The first uncertainty is statistical (renormalized by χ) and the second is systematic.

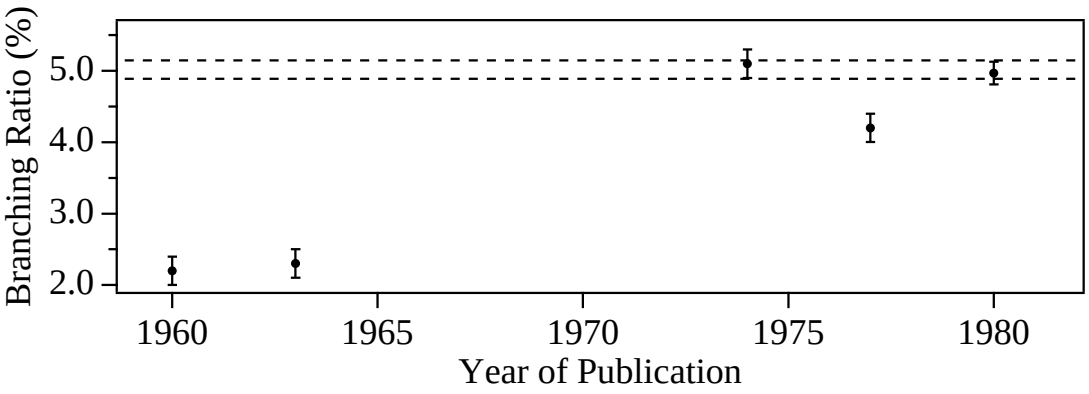

Figure 7.10: Measurements of the excited-state branching ratio.

Fixed	$a_{\beta\nu}$	b_{Fierz}	b
b_{Fierz}, b	0.5243±0.0066	0.0	82.63
b	0.5250±0.0214	−0.005±0.027	82.63
b_{Fierz}	0.5234±0.0112	0.0	59±25
none	0.5462±0.0345	0.053±0.073	105±64

Table 7.8: Results for combinations of fitting variables. Only data in the $^{21}Ne^{+}$ peak is used. Uncertainties shown are statistical only.

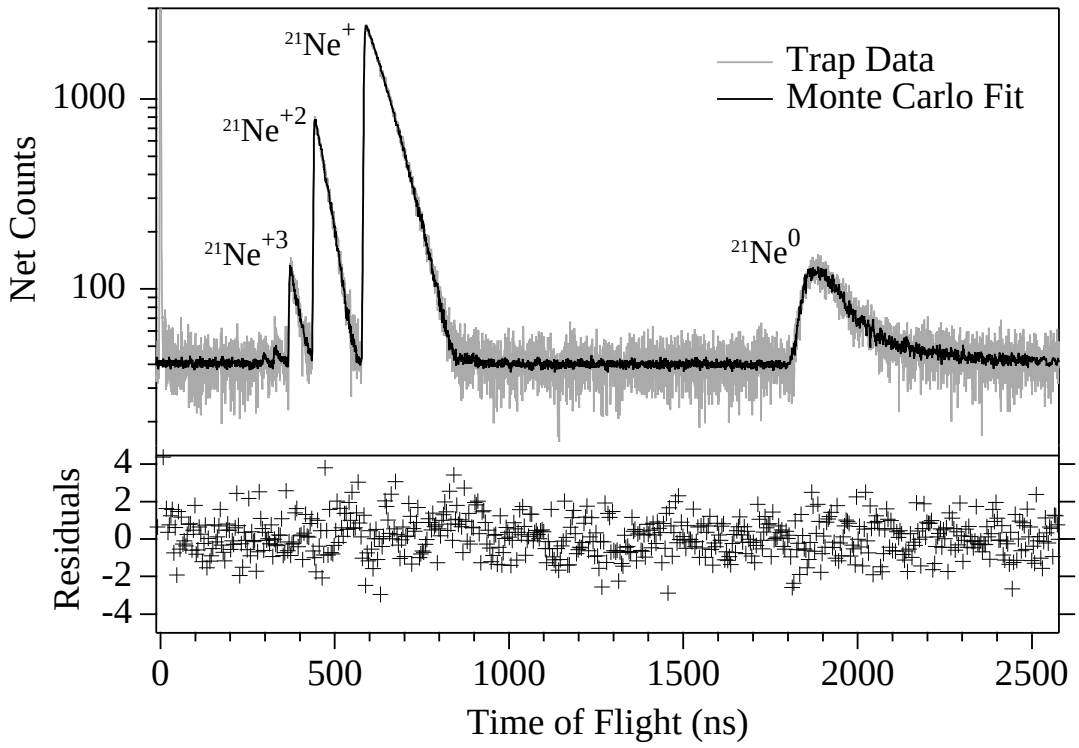

Figure 7.11: TOF spectra fit with the Monte Carlo simulation, with bin width 0.43 ns. Residuals are shown with 4.3 ns bins for clarity.

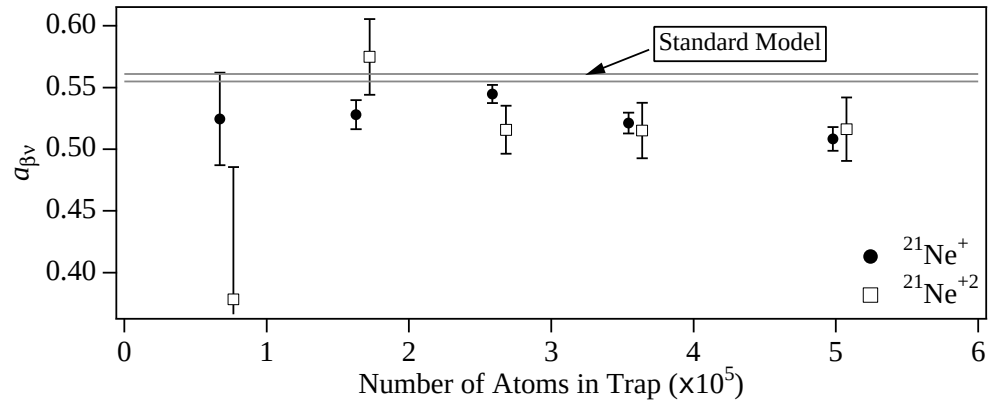

Figure 7.12: $a_{\beta\nu}$ at different trap populations. The $^{21}Ne^{+2}$ data have been slightly offset for clarity.

7.8 Population Dependence?

Figure 7.12 shows $a_{\beta\nu}$ for $^{21}Ne^{+}$ and $^{21}Ne^{+2}$ as a function of the number of trapped atoms. For the $^{21}Ne^{+}$ data, the slope is in 2.3 σ disagreement with zero. For a horizontal line, $\chi^2 = 2.3$ per degree-of-freedom, and statistical uncertainties have been readjusted by this χ to account for the spread in the results. We find no reason justifying an extrapolation of the measured $\beta - \nu$ coefficients to zero trap population and do not make any claims about the significance of doing so. However, the extrapolation gives $a_{\beta\nu} = 0.55 \pm 0.02$ (only statistical uncertainty), in reasonable agreement with the Standard Model.

Although a number effects could decrease the $\beta - \nu$ correlation as the trap population increases, none account for the size of the observed correlation. The CCD camera indicates the trap position is stable to 0.1 mm over the entire run, and the rising edge of the ion peaks do not change by more than 0.1 ns, regardless of trap population. The development of a significant polarization distribution within the trap would lead to TOF shifts of the peak of order nanoseconds due to the directional correlation between $\vec{p}_e$ and the nuclear spin.

For a typical Gaussian population distribution with a FWHM of 0.80 mm, the TOF spectra receive a timing convolution with a FWHM of 7 ns. This softens the otherwise

Effect	Size	Uncertainty
Trap volume	0.0000	0.0018
Trap position	0.0000	0.0004
MCP threshold	0.0010	0.0003
β-detector threshold	0.0011	0.0004
γ-ray correction	0.0008	0.0004
Deadtime	0.0004	0.0002
Scattering cross-sections	0.0000	0.0000
Net polarization or alignment	0.0000	0.0008
Polarization gradient	0.0000	0.0011
Electric field	0.0000	0.0011
Loss rate from trap	0.0000	0.0003
Total	0.0033	0.0026

Table 7.9: Systematic effects that scale with trap population.

sharp rising edge at the shortest TOFs of the ion peaks. The convolution is too small to significantly affect the distribution at longer TOFs. When the entire TOF distribution is fit, typical trap dimension uncertainties of ± 0.1 mm lead to uncertainties of ≈ 0.01 in $a_{\beta\nu}$. However, excluding the first 15 ns of each ion peak reduces the uncertainty to <0.002. Since this is a significant reduction in systematic uncertainty for a minimal sacrifice in statistics, the analysis excludes the first 15 ns of each ion peak.

At the highest rates, the average β-detector pulse height output increased by $\approx 1.5\%$ and the MCP output decreased by $9 \pm 3\%$, leading to minimal change in detector efficiencies and $a_{\beta\nu}$. The detection efficiency for ^{21}Na atoms escaping from the trap is negligible. Scattering cross sections for recoil-ions or β's emerging from the cloud of trapped atoms are expected to be $< 10^{-13}\,\mathrm{cm}^2$, several orders of magnitude too small to influence $a_{\beta\nu}$. Charge exchange would create $^{21}\mathrm{Na}^+$ essentially at rest, giving a narrow TOF peak at 728 ns that is not seen. These effects and their uncertainties are summarized in Table 7.9.

Chapter 8

Conclusions and Future Work

In this dissertation we have demonstrated the utility of trapped radioactive atoms for precision β decay measurements. The efficiency of the magneto-optical trap was improved so that we could trap 0.01% of the ^{21}Na atoms created from bombardment of MgO disk targets by a 25 MeV proton beam. Using 2 μA of beam current, we were able to collect up to 800,000 atoms, or 0.67 μCi of activity, in the trap. A precise measurement of the charge-state distribution [118] and β decay correlation coefficients $a_{\beta\nu}$ and b_{Fierz} [161] were completed. The result, $a_{\beta\nu} = 0.5243 \pm 0.0092$ is in 3.6 σ disagreement with the Standard Model and warrants further study. We suspect measurements of the β decay branching ratio to the excited-state, if not in error, at least have underestimated uncertainties. The branching ratio is rather poorly known (best measurements have 3% relative uncertainty), with large disagreements between measurements.

8.1 ^{21}Na β Decay Branching Ratio

We plan to make a definitive measurement of this branching ratio with a fractional uncertainty of $\approx$1% using ISAC at TRIUMF. This should reduce the systematic uncertainty on the $\beta - \nu$ correltion to <0.001. Using a pure (contaminants <0.1%) beam of ^{21}Na accelerated to 1.5 MeV/nucleon, we will bombard a thin plastic scintillator and count atoms individually to precisely characterize the source strength. A calibrated high purity Ge

detector subtending a solid angle of about 0.1% of 4π will count excited-state γ-rays at 350 keV. With a beam intensity of 1×10^5 ions/s, we should be able to obtain a statistical uncertainty of 0.5% in $\approx$4 hours. We expect to avoid the 511 keV background in the Ge detector by careful design of the source and shielding, so that β^+s annihilate in areas either shielded from or far from the Ge detector. These measures are required to minimize the Compton edge from 511 keV γ-rays, which is near the energy of interest. The Ge detector will be characterized with sources and the critical calibration will be accomplished using the 356 keV γ-ray from a ^{133}Ba source with calibrated absolute activity.

8.2 Position-Sensitive MCP

We plan to measure the ion position along with the time-of-flight using a position-sensitive Z-stack MCP with an output gain of $> 10^7$. The position is determined by the charge division at four corners of a resistive anode, and spatial resolution of $\approx$1 mm should be achievable. The spatial distribution of recoils should allow a discrimination of backgrounds. The position of the trapped atoms in the y-z plane of Figure 7.1 could be accurately determined by the peak of the ion spatial distribution. The increased gain should reduce MCP detection efficiency uncertainties.

8.3 Shake-Off Electron Detection

One major difficulty with measuring the $\beta - \nu$ correlation using the technique described in this dissertation is the detection of the β^+s. The solid angle subtended by the β-detector is $\approx$1% so the coincident detection efficiency was only 0.1%. Unfortunately, the solid angle must be this small to allow sufficient suppression of backscattered β^+s by the collimator. In addition, the β spectrum extends down to zero energy, so part of the spectrum will always be below threshold. While a low-energy threshold limits the uncertainties associated with the β-detector calibration, it never completely removes them. The problems associated with backscattering and annihilation radiation also make β^+ energy

determination and the discrimination of backgrounds challenging.

For these reasons we have decided to test the merits of another coincident detection scheme. By replacing the β-detector with a MCP (which we will refer to as the eMCP), we will detect shake-off electrons in coincidence with recoil-ions. The electric field will guide all ions into one MCP and the majority of shake-off electrons into the eMCP. Since we expect the eMCP detection efficiencies for keV-energy electrons to be 20–70% [162, 163, 93, 164], the coincident detection efficiency should be $\approx$5%. This is nearly two orders of magnitude higher than when detecting β^+s. In addition, the entire spectrum is detected (including electron capture decays), eliminating uncertainties associated with the detection of β^+s. The coincident detection of recoiling ion and electrons with MCPs following electron capture decays has already been successfully demonstrated [165, 18].

The detection of shake-off electrons will lead to a different set of systematic effects and backgrounds. Shake-off electron detection does not restrict the recoil direction like with coincident β^+ detection, making it more difficult to collect all $^{21}Ne^+$ ions to the MCP. The electric fields required to draw all recoil-ions into the MCP active area are approximately twice as large when the β^+ is not detected. Electrode voltages of $\pm$10 kV are required in our current chamber geometry. In addition, the larger transverse momentum results in ion trajectories that hit the MCP at angles up to 5°. The TOF spread for each charge-state is larger, making it more difficult to separate the different peaks. To provide such large electric fields, the electrodes in front of each MCP were brought in as close to the trap as possible, resulting in the geometry shown in Figure 8.1. Equipotential lines are shown separated by 1 kV for voltages ranging from +10 kV on the eMCP to −10 kV on the PSMCP.

Ions and electrons emerging from electrode surfaces can lead to significant backgrounds. We need to be concerned with $e^- - ^{21}Ne^+$ coincidences from these electrodes. On the electrode by the eMCP, only recoil-ions from the tip can reach the PSMCP. If this is a problem, the eMCP can be biased 1 kV lower than its associated collimator so the shake-off electrons are energetically forbidden from reaching the eMCP. It is more difficult to ensure that no shake-off electron originating from the collimator in front of the PSMCP will be

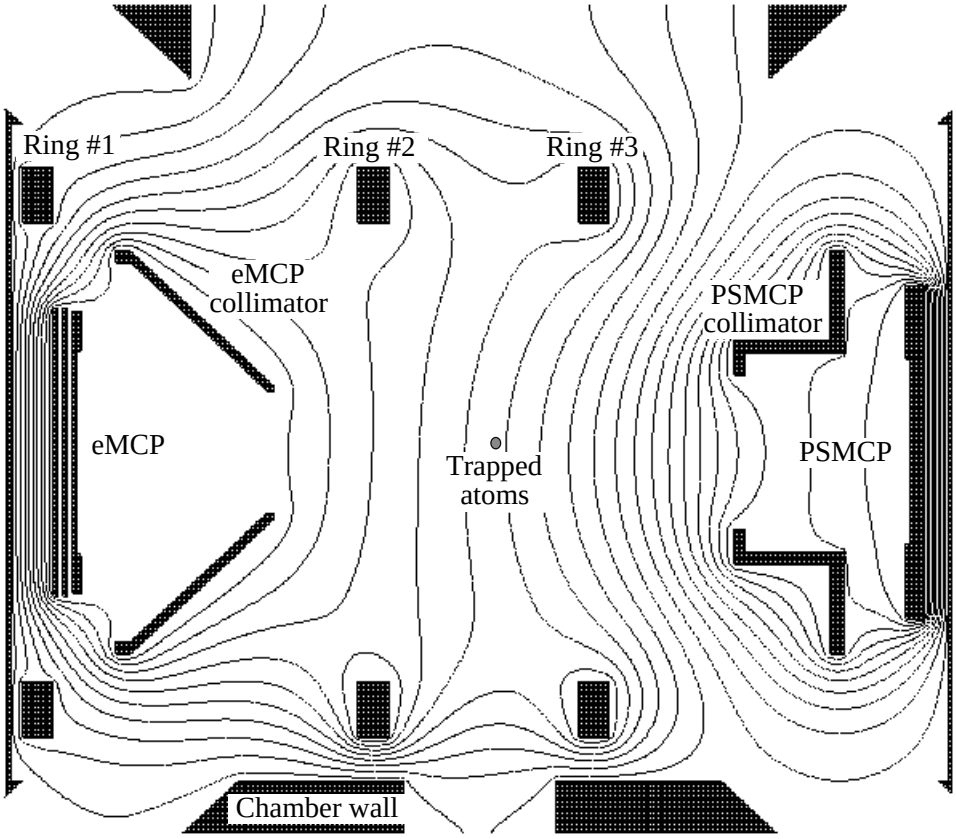

Figure 8.1: Cross-sectional view of electrodes to be used for coincident $e^- - {}^{21}Ne$ detection. Equipotential lines with 1 kV spacing are also shown for the voltages used to generate preliminary time-of-flight spectra.

detected because the energy spectrum of the shake-off electrons is not well understood. However, with the electrode geometry in Figure 8.1, very few electrons of energy <200 eV reach the eMCP.

Additional backgrounds can arise from the eMCP detecting β^+s or γ-rays. During off-line tests with radioactive sources, we estimated the MCP detection efficiency is $\lesssim$1% for these types of radiation. When combined with the small solid angle of the detector, these backgrounds should be small. Another background would result from any electron liberated when a β^+ or γ-ray strikes an electrode. These electrons could be drawn into the eMCP by the electric field. The conical shape of the eMCP collimator should help limit the number of such events. We will need to measure and understand different backgrounds when detecting shake-off electrons.

The backgrounds can be studied separately. Negatively biasing the eMCP relative to its collimator, we can exclude electrons below selected energies. The ion trajectories do not depend on the voltage at the eMCP. Since electrons from the trap will have an energy $\gtrsim$3 keV smaller than electrons that emerge from the electrodes and 5 keV larger than those that emerge from the chamber walls, they should be easy to sort according to energy. Of course, we hope these backgrounds are small enough that no correction needs to be made, but even if they are appreciable, they can be isolated and properly taken into account.

A Monte Carlo simulation of the TOF spectra for recoil-ions from an unpolarized trap is shown in Figure 8.2. The shake-off electron TOF is only 3 ns and varies by less than 0.5 ns for energies less than 100 eV. Compared with the 7 ns spread in TOFs from the trap dimensions, this time spread is inconsequential. Since the $\beta - \nu$ correlation favors large nuclear recoils, it causes more events to be detected at extremal TOFs and fewer at intermediate TOFs. However, the TOF distribution is measured for all recoil angles and energy so the contribution from the $\beta - \nu$ correlation is suppressed. For ^{21}Na, the $\beta - \nu$ correlation causes a shift in 11% of the spectrum. Although smaller than the 21% change in the spectrum when β^+ are detected in coincidence, it is enough for a precision measurement.

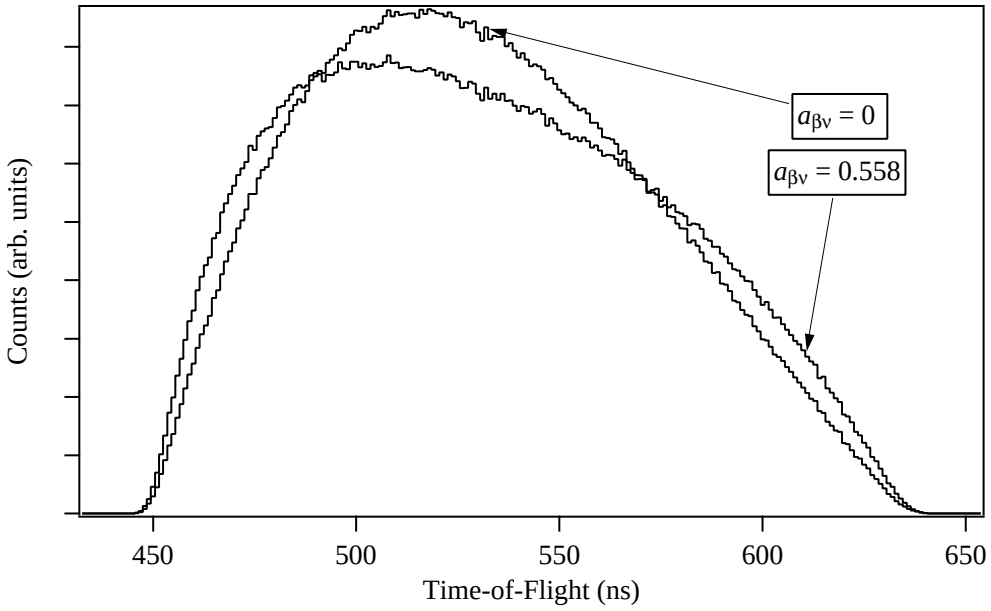

Figure 8.2: An example of a TOF spectra for ground-state decays from an unpolarized trap assuming $a_{\beta\nu} = 0$ and $a_{\beta\nu} = 0.558$.

8.4 Polarized Trap

With polarized ^{21}Na atoms, the correlation coefficients A_β, B_ν, c_{align}, and D_{TRV} defined in Equation 2.13 as well as several other correlations defined in Ref. [36] can be measured. A polarized sample of ^{21}Na has been produced by optical pumping with polarizations of 62% [166]. The results of a measurement of the ratio of longitudinal β^+ polarization emitted parallel and anti-parallel to the nuclear spin were consistent with the Standard Model, but not particularly competitive with other tests [167].

We are working on loading atoms from the MOT into a spin-polarized far-off-resonance trap (FORT). Corwin et al. [168] reported loading 37% of the Rb atoms originally held in a MOT into a spin-polarized FORT and have extensively characterized its loading properties [169]. They used the following technique. After first loading atoms into a MOT, the FORT laser is turned on and the MOT laser's power and detunings are altered to aid in cooling and loading the FORT. To efficiently load Rb atoms into a circularly-polarized

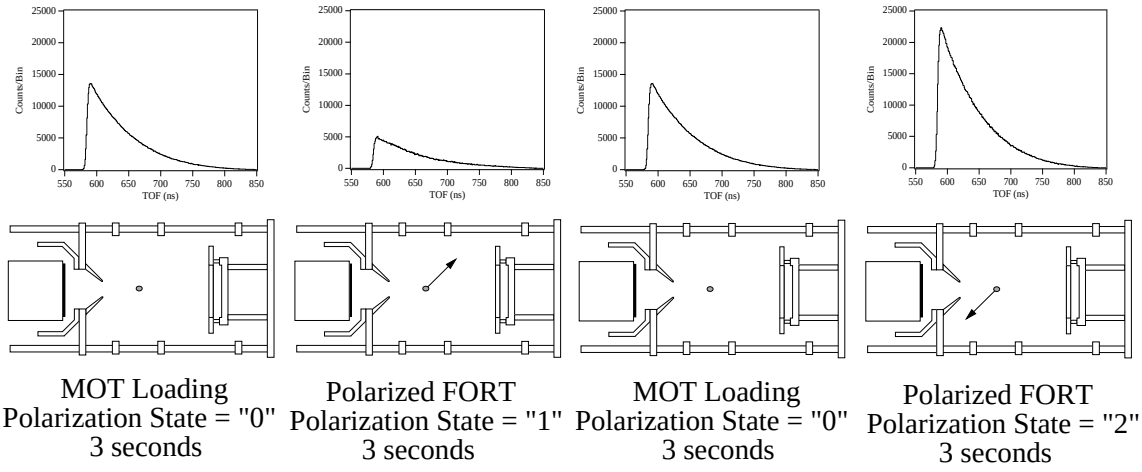

Figure 8.3: Potential duty cycle for correlation measurements by $\beta^+ - ^{21}$Ne coincidences. Calculated TOF spectra (for $^{21}Ne^+(3/2^+)$) assuming equal source strength in each step of the cycle.

FORT, the researchers first loaded them into a linear FORT and rapidly changed the laser polarization of the FORT beam to circular. They investigated the properties of their FORT and found it had a lifetime of $\approx$10 s and a polarization of 98$\pm$1%.

Optical access in the existing trapping chamber restricts the FORT laser to propagate along the x'-axis of Figure 7.1. If we acceive nearly 100% polarization (which for spin 3/2 is nearly 100% alignment also) along the x' and $-x'$ directions, several decay correlations can be measured. By detecting $\beta^+ - ^{21}$Ne coincidences, we could measure all six decay correlations in Equation 2.13 in the same experiment. A possible duty cycle and anticipated TOF spectra are illustrated in Figure 8.3. By taking the difference between recoil-ion data with polarization states "1" and "2", we could measure A_β and B_ν. During state "0", the loading phase of the MOT, data identical to that of this dissertation would be collected, allowing $a_{\beta\nu}$ and b_{Fierz} to be measured. By comparing the TOFs from state "0" and the average of states "1" and "2", we could determine c_{align}. A position-sensitive MCP would be crucial for this measurement, as the TOF spectra would be complemented by the distribution of ion impacts at the MCP. Any asymmetry of ion recoils along the z-axis that follows the nuclear polarization would indicate a non-zero D_{TRV}.

The appeal of measuring all these coefficients in the same experiment with one data set is compelling. One difficulty would be attaining the necessary statistical precision. For a measurement of these coefficients to a statistical precision of 0.01 would require detecting 100,000 coincidences from a polarized sample. We will assume a duty cycle that consists of 3 s of collecting atoms in the MOT followed by holding them for 3 s in a FORT. Currently we load an average of 300,000 atoms into the MOT, which takes 20 s to fill. Therefore, we expect after 3 s, the MOT will collect 150,000 atoms of which 35% can be loaded into a FORT. The average population for a FORT with a lifetime of 3 s would be about half of the initial population. The average number of spin-polarized atoms maintained in the trap (after accounting for the 50% duty cycle) would be only 13,000 atoms. The rate of $\beta^+ - ^{21}$Ne coincidences would be decreased by a factor of 25 relative to the rates achieved without a polarized sample. Optimistically, we could hope to get only 20,000 coincidences during a run.

The detection of shake-off electrons increases the coincident rate by up to two orders of magnitude, at a cost giving up information on the β energy and direction of emission. The nuclear recoil tends to be anti-parallel to the nuclear spin because both the β^+ and ν are preferentially emitted along the spin direction. The TOFs for states "1" and "2" look different, even without using the β^+ to trigger the acquisition. In the absence of backgrounds, we calculate the TOF spectra shown in Figure 8.4. This method allows a measurememt of a linear combination of A_β and B_ν (but not A_β and B_ν separately) as well as c_{align} with a statistical precision of 0.006 in a single run.

Since the electronics and detection schemes required for either technique are similar, we are currently pursuing both avenues. We expect future developments such as how efficiently we can load a spin-polarized trap and how much background contaminates coincidences with shake-off electrons to make one choice more appealing than the other.

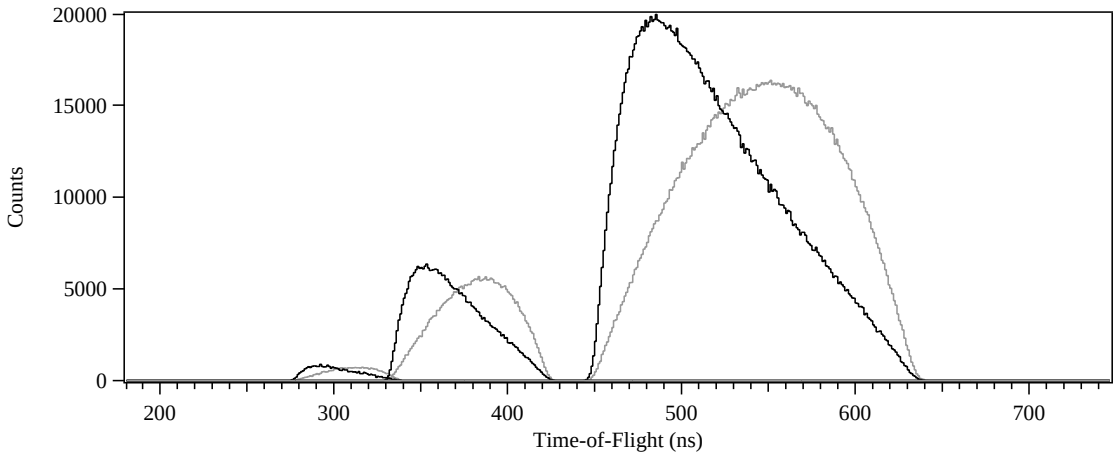

Figure 8.4: Monte Carlo simulations of $e^- - ^{21}Ne$ coincidences for polarization states "1" (gray) and "2" (black). The electric field draws all ions to the PSMCP and separates the charge-state TOFs.

Appendix A

Summary of $\beta - \nu$ Correlation Measurements

In the 1950's and 1960's, $\beta - \nu$ correlation measurements were crucial for determining the $V - A$ structure of the weak interaction. Most experiments studied noble gases so that the perturbing effects of source scattering and molecular bonding could be avoided. Atom trapping techniques should allow precise measurement of β decay properties in many other isotopes. The goal of modern $\beta - \nu$ correlation experiments is to place limits on scalar and tensor admixtures, and to study recoil order effects. All reported measurements of $\beta - \nu$ correlations are summarized in Table A.1.

Isotope	Technique	$a_{\beta\nu}$	Reference
n	β^-−p coincidence	0.089±0.108	[170]
n	p energy spectrum	−0.099±0.011	[171]
n	p energy spectrum	−0.1017±0.0051	[67]
^{6}He	β^-−^{6}Li$^+$ coincidence	0.36±0.11	[172, 173]
^{6}He	^{6}Li$^+$ energy spectrum	−0.39±0.05	[13]
^{6}He	β^-−^{6}Li$^+$ coincidence	−0.353±0.053	[14]
^{6}He	^{6}Li$^+$ energy spectrum	−0.3343±0.0030	[15]
^{8}Li	$\beta^- - \alpha$ coincidence	–	[174]
^{11}Be	$\beta - \gamma$ Doppler shift	–	[175]
^{14}O	$\beta^+ - \gamma$ Doppler shift	–	[66]
^{18}Ne	$\beta^+ - \gamma$ Doppler shift	1.06±0.10	[68]
^{19}Ne	β^+−^{19}F$^-$ coincidence	−0.8±0.4	[176]
^{19}Ne	^{19}F$^-$ energy spectrum	−0.21±0.08	[151]
^{19}Ne	β^+−^{19}F$^-$ coincidence	−0.15±0.20	[17]
^{19}Ne	β^+−^{19}F$^-$ coincidence	0.14±0.13	[177]
^{19}Ne	^{19}F$^-$ energy spectrum	0.00±0.08	[13]
^{23}Ne	$\beta^- - \gamma$ coincidence	–	[178]
^{23}Ne	^{23}Na$^+$ energy spectrum	−0.37±0.04	[13]
^{23}Ne	^{23}Na$^+$ energy spectrum	−0.33±0.03	[16]
^{20}Na	$\beta^+ - \alpha$ coincidence	–	[179, 180]
^{21}Na	β^+−^{21}Ne ion coincidence	0.5243±0.0092	this work
^{32}Ar	β^+-delayed p spectrum	1.00±0.04	[181]
^{32}Ar	β^+-delayed p spectrum	0.9989±0.0065	[69]
^{33}Ar	β^+-delayed p spectrum	1.02±0.02	[181]
^{33}Ar	β^+-delayed p spectrum	0.944±0.004	[70]
^{35}Ar	^{35}Cl$^-$ energy spectrum	0.9±0.3	[182]
^{35}Ar	^{35}Cl$^-$ energy spectrum	0.70±0.17	[182]
^{35}Ar	^{35}Cl$^-$ energy spectrum	0.97±0.14	[13]
^{37}K	β^+−^{37}Ar ion coincidence	–	[22]
^{38m}K	β^+−^{38}Ar ion coincidence	–	[22]

Table A.1: Compilation of all $\beta - \nu$ correlation measurements. If the authors do not report a value for $a_{\beta\nu}$, no result is listed. Errors are quoted at 1σ.

Bibliography

[1] F. Reines and J. C. L. Cowan *Science*, vol. 124, p. 103, 1956.

[2] T. D. Lee and C. N. Yang *Phys. Rev.*, vol. 104, p. 254, 1956.

[3] C. S. Wu *et al. Phys. Rev.*, vol. 105, p. 1413, 1957.

[4] R. L. Garwin, L. M. Lederman, and M. Weinrich *Phys. Rev.*, vol. 105, p. 1415, 1957.

[5] J. I. Friedman and V. L. Telegdi *Phys. Rev.*, vol. 105, p. 1681, 1957.

[6] M. T. Bungy *et al. Phys. Rev.*, vol. 110, p. 1214, 1958.

[7] T. Fazzini *et al. Phys. Rev. Letts.*, vol. 1, p. 247, 1958.

[8] G. Impeduglia *et al. Phys. Rev. Letts.*, vol. 1, p. 249, 1958.

[9] J. H. Christenson, J. W. Cronin, V. L. Fitch, and R. Turlay *Phys. Rev. Lett.*, vol. 13, p. 138, 1964.

[10] B. Aubert *et al. Phys. Rev. Lett.*, vol. 87, p. 091801, 2001.

[11] K. Abe *et al. Phys. Rev. Lett.*, vol. 87, p. 091802, 2001.

[12] I. S. Towner and J. C. Hardy *J. Phys. G*, vol. 29, p. 197, 2003.

[13] J. S. Allen, R. L. Burman, W. B. Herrmannsfeldt, P. Stahelin, and T. H. Braid *Phys. Rev.*, vol. 116, p. 134, 1959.

[14] B. W. Ridley *Nucl. Phys.*, vol. 25, p. 483, 1961.

[15] C. H. Johnson, F. Pleasonton, and T. A. Carlson *Phys. Rev.*, vol. 132, p. 1149, 1963.

[16] T. A. Carlson *Phys. Rev.*, vol. 132, p. 2239, 1963.

[17] W. P. Alford and D. R. Hamilton *Phys. Rev.*, vol. 105, p. 673, 1957.

[18] M. M. Hindi *et al. Phys. Rev. C*, vol. 58, p. 2512, 1998.

[19] M. Trinczek *et al. Phys. Rev. Lett.*, vol. 90, p. 012501, 2003.

[20] P. Delahaye *et al. Hyperfine Interactions*, vol. 132, p. 479, 2001.

[21] D. Beck *et al. Nucl. Phys. A*, vol. 701, p. 369, 2002.

[22] A. Gorelov *et al. Hyperfine Interactions*, vol. 127, p. 373, 2000.

[23] E. D. Commins, *Weak Interactions.* San Francisco: McGraw-Hill, Inc., 1973.

[24] M. Morita, *Beta Decay and Muon Capture.* Reading, MA: W. A. Benjamin, Inc., 1973.

[25] C. S. Wu and S. A. Moszkowski, *Beta Decay.* New York: John Wiley & Sons, Inc., 1966.

[26] S. Weinberg *Phys. Rev.*, vol. 112, p. 1375, 1958.

[27] P. Langacker *Phys. Rev. D*, vol. 14, p. 2340, 1976.

[28] H. Stremnitzer *Phys. Rev. D*, vol. 10, p. 1327, 1974.

[29] D. H. Wilkinson *Eur. Phys. J. A*, vol. 7, p. 307, 2000.

[30] L. Grenacs *Ann. Rev. Nucl. Part. Sci.*, vol. 35, p. 455, 1985.

[31] F. P. Calaprice *Phys. Rev. C*, vol. 12, p. 2016, 1975.

[32] D. E. Groom *et al. Eur. Phys. J. C*, vol. 15, p. 1, 2000.

[33] H. Abele *et al. Phys. Lett. B*, vol. 407, p. 212, 1997.

[34] H. Abele *et al. Phys. Rev. Lett.*, vol. 88, p. 211801, 2002.

[35] D. H. Wilkinson *Nucl. Instrum. and Meth. Phys. Res. A*, vol. 290, p. 509, 1989.

[36] J. D. Jackson, S. B. Treiman, and J. H. W. Wyld 1957.

[37] G. Azuelos and J. E. Kitching *Phys. Rev. C*, vol. 12, p. 563, 1975.

[38] J. W. L. Talbert and M. G. Stewart *Phys. Rev.*, vol. 119, p. 272, 1960.

[39] S. E. Arnell and E. Wernbom *Arkiv för Fysik*, vol. 25, p. 389, 1963.

[40] D. E. Alburger *Phys. Rev. C*, vol. 9, p. 991, 1974.

[41] G. Azuelos, J. E. Kitching, and K. Ramavataram *Phys. Rev. C*, vol. 15, p. 1847, 1977.

[42] H. S. Wilson, R. W. Kavanagh, and F. M. Mann *Phys. Rev. C*, vol. 22, p. 1696, 1980.

[43] R. Wallace and J. J. A. Welch *Phys. Rev.*, vol. 117, p. 1297, 1960.

[44] G. Audi and A. H. Wapstra *Nucl. Phys. A*, vol. 595, p. 409, 1995.

[45] S. E. Arnell, J. Dubois, and O. Almen *Nucl. Phys.*, vol. 6, p. 196, 1958.

[46] E. Browne, R. B. Firestone, and V. S. Shirley, eds., *Table of Radioactive Isotopes*. New York: John Wiley & Sons, Inc., 1986.

[47] P. M. Rowe *et al. J. Phys. G*, vol. 4, p. 431, 1978.

[48] I. S. Towner, J. C. Hardy, and M. Harvey *Nucl. Phys. A*, vol. 284, p. 269, 1977.

[49] W. E. Ormand and B. A. Brown *Phys. Rev. C*, vol. 52, p. 2455, 1995.

[50] J. C. Hardy and I. S. Towner *Eur. Phys. J. A*, vol. 15, p. 223, 2002.

[51] O. Naviliat-Cuncic, T. A. Girard, J. Deutsch, and N. Severijns *J. Phys. G*, vol. 17, p. 919, 1991.

[52] J. C. Brodine *Phys. Rev. D*, vol. 1, p. 100, 1970.

[53] D. H. Wilkinson *Nucl. Instrum. and Meth. Phys. Res. A*, vol. 275, p. 378, 1989.

[54] D. H. Wilkinson *Nucl. Instrum. and Meth. Phys. Res. A*, vol. 335, p. 305, 1993.

[55] D. H. Wilkinson *Nucl. Instrum. and Meth. Phys. Res. A*, vol. 365, p. 203, 1995.

[56] D. H. Wilkinson *Nucl. Instrum. and Meth. Phys. Res. A*, vol. 365, p. 497, 1995.

[57] D. H. Wilkinson *Nucl. Instrum. and Meth. Phys. Res. A*, vol. 401, p. 275, 1997.

[58] B. R. Holstein *Rev. Mod. Phys.*, vol. 46, p. 789, 1974.

[59] B. R. Holstein and S. B. Treiman *Phys. Rev. C*, vol. 3, p. 1921, 1971.

[60] O. Ames, E. A. Phillips, and S. S. Glickstein *Phys. Rev.*, vol. 137, p. B1157, 1965.

[61] P. Raghavan *At. Nucl. Data Tables*, vol. 42, p. 189, 1989.

[62] B. R. Holstein, W. Shanahan, and S. B. Treiman 1972.

[63] B. R. Holstein *Phys. Rev. C*, vol. 9, p. 1742, 1974.

[64] A. Sirlin *Phys. Rev.*, vol. 164, p. 1767, 1967.

[65] F. Glück *Comp. Phys. Comm.*, vol. 101, p. 223, 1997.

[66] For an example of the delicateness of the observable see V. Vorobel et al. Eur. Phys. J. A, 16:139, 2003.

[67] C. Stratowa, R. Dobrozemsky, and P. Weinzierl *Phys. Rev. D*, vol. 18, p. 3970, 1978.

[68] V. Egorov *et al. Nucl. Phys. A*, vol. 621, p. 745, 1997.

[69] E. G. Adelberger *et al. Phys. Rev. Lett.*, vol. 83, p. 1299, 1999.

[70] A. García *et al. Hyperfince Interactions*, vol. 129, p. 237, 2000.

[71] By assuming $a_{\beta\nu} = -1/3$, the recoil-ion spectrum determines the ^{23}Ne branching ratio to ground- and first excited-state to be 67±1% and 32±1%, respectively.

[72] O. Zimmer, J. Byrne, M. G. D. van der Grinten, W. Heil, and F. Glück *Nucl. Instrum. and Meth. in Phys. Res. A*, vol. 440, p. 548, 2000.

[73] S. G. Crane *et al. Phys. Rev. Lett.*, vol. 86, p. 2967, 2001.

[74] D. J. Vieira (vieira@lanl.gov), (private communication).

[75] J. E. Simsarian *et al. Phys. Rev. Letts.*, vol. 76, p. 3522, 1996.

[76] G. D. Sprouse *et al. Nucl. Instrum. and Meth. in Phys. Res. B*, vol. 126, p. 370, 1997.

[77] Z.-T. Lu (lu@anl.gov), (private communication).

[78] With a halflife of 26 d, ^{82}Sr is a convenient off-line parent source of ^{82}Rb ($t_{1/2} = 75$ s).

[79] Z.-T. Lu *et al. Phys. Rev. Lett.*, vol. 72, p. 3791, 1994.

[80] M. Rowe *et al. Phys. Rev.*, vol. 59, p. 1869, 1999.

[81] M. A. Rowe. PhD thesis, Department of Physics, University of California, Berkeley, 1999.

[82] R. J. Napolitano, S. C. Zilio, and V. S. Bagnato *Optics Comm.*, vol. 80, p. 110, 1990.

[83] The maximum magnetic field setting and velocity distribution had previously been incorrectly calculated. Those results have been recalculated for comparisons to present results.

[84] T. Barrett, S. Dapore-Schwartz, M. Ray, and G. Lafyatis *Phys. Rev. Lett.*, vol. 67, p. 3483, 1991.

[85] S. Miranda *et al. Phys. Rev. A*, vol. 59, p. 882, 1999.

[86] http://www.el-mul.co.il.

[87] R. Naaman and Z. Vager *Rev. Sci. Instrum.*, vol. 67, p. 3332, 1996.

[88] L. B. C. Worth, J. S. Lapington, and M. W. Trow *Nucl. Instrum. and Meth. Phys. Res. A*, vol. 392, p. 364, 1997.

[89] S. J. Sijbrandij and M. K. Miller *Ultramicroscopy*, vol. 79, p. 265, 1999.

[90] S. J. Sijbrandij *et al. J. de Phys. IV, C5*, vol. 6, p. 297, 1996.

[91] http:usa.hamamatsu.com.

[92] L. Zhu *et al. J. Vac. Sci. Technol. A*, vol. 12, p. 2037, 1994.

[93] Burle Technologies, Inc., *Long-Life*$^{\text{TM}}$ *Microchannel Plates*, 1999.

[94] Proceedings of the 1999 Particle Accelerator Conference (Cat. No.99CH36366). IEEE, vol. 3, (New York, NY), 1999.

[95] G. W. Fraser *Int. J. of Mass Spect.*, vol. 215, p. 13, 2002.

[96] H. C. Straub *et al. Rev. Sci. Instrum.*, vol. 70, p. 4238, 1999.

[97] S. Yagi *et al. Nucl. Instrum. and Meth. B*, vol. 183, p. 476, 2001.

[98] B. Deconihout, P. Gerard, M. Bouet, and A. Bostel *Allied Surface Science*, vol. 94/95, p. 422, 1996.

[99] M. L. Edgar, J. S. Lapington, and A. Smith *Rev. Sci. Instrum.*, vol. 63, p. 816, 1992.

[100] G. W. Fraser, M. T. Pain, J. E. Lees, and J. F. Pearson *Nucl. Instrum. and Meth. A*, vol. 306, p. 247, 1991.

[101] L. Giudicotti, M. Bassan, R. Pasqualotto, and A. Sardella *Rev. Sci. Instrum.*, vol. 65, p. 247, 1994.

[102] R. S. Gao *et al. Rev. Sci. Instrum.*, vol. 55, p. 1756, 1984.

[103] L. J. Lising. PhD thesis, Department of Physics, University of California, Berkeley, 1999.

[104] *The Theory and Practice of Scintillation Counting.* New York: Pergamon, 1964.

[105] R. L. Craun and D. L. Smith *Nucl. Instrum. and Meth.*, vol. 80, p. 239, 1970.

[106] H. Behrens and J. Jänecke, *Numerical Tables for Beta-Decay and Electron Capture.* New York: Springer-Verlag, 1969.

[107] F. Glück *Nucl. Phys. A*, vol. 628, p. 493, 1998.

[108] T. Luhmann *Rev. Sci. Instrum.*, vol. 68, p. 2347, 1997.

[109] T. A. Carlson, F. Pleasonton, and C. H. Johnson *Phys. Rev.*, vol. 129, p. 2220, 1963.

[110] T. A. Carlson *Phys. Rev.*, vol. 130, p. 2361, 1963.

[111] A. H. Snell and F. Pleasonton *Phys. Rev.*, vol. 107, p. 740, 1957.

[112] T. A. Carlson *Phys. Rev.*, vol. 131, p. 676, 1963.

[113] O. Kofoed-Hansen *Phys. Rev.*, vol. 96, p. 1045, 1954.

[114] A. H. Snell and F. Pleasonton *Phys. Rev.*, vol. 100, p. 1396, 1955.

[115] F. Pleasonton and A. H. Snell *Proc. Roy. Soc. (London) A*, vol. 241, p. 141, 1957.

[116] A. H. Snell and F. Pleasonton *Phys. Rev.*, vol. 111, p. 1338, 1958.

[117] A. H. Snell, F. Pleasonton, and J. L. Need *Phys. Rev.*, vol. 116, p. 1548, 1959.

[118] N. D. Scielzo, S. J. Freedman, B. K. Fujikawa, and P. A. Vetter. to be published.

[119] P. Stephas and B. Crasemann *Phys. Rev.*, vol. 164, p. 1509, 1967.

[120] Y. Isozumi, T. Mukoyama, and S. Shimizu *Phys. Rev. Lett.*, vol. 29, p. 298, 1972.

[121] L. Wauters *et al. J. Phys. B*, vol. 30, p. 4569, 1997.

[122] T. Mukoyama and S. Ito *Phys. Lett. A*, vol. 131, p. 182, 1988.

[123] C. F. Bunge, M. Galan, R. Jauregui, and A. V. Bunge *Nucl. Instrum. and Meth. Phys. Res.*, vol. 202, p. 299, 1982.

[124] Y. K. Bae, J. R. Peterson, A. S. Schlachter, and J. W. Stearns *Phys. Rev. Lett.*, vol. 54, p. 789, 1985.

[125] T. Sakurai and T. Hashizume *Rev. Sci. Instrum.*, vol. 57, p. 236, 1986.

[126] A. Muller, N. Djuric, G. H. Dunn, and D. S. Belic *Rev. Sci. Instrum.*, vol. 57, p. 349, 1986.

[127] A. Bader *et al. Meas. Sci. Technol.*, vol. 6, p. 959, 1995.

[128] B. Brehm, J. Grosser, T. Ruscheinski, and M. Zimmer *Meas. Sci. Technol.*, vol. 6, p. 953, 1995.

[129] J. Oberheide, P. Wilhelms, and M. Zimmer *Meas. Sci. Technol.*, vol. 8, p. 351, 1997.

[130] H. C. Straub *et al. Rev. Sci. Instrum.*, vol. 70, p. 4238, 1999.

[131] A. G. Kochur, V. L. Sukorukov, A. I. Dudenko, and P. V. Demekhin *J. Phys. B*, vol. 28, p. 387, 1995.

[132] J. S. Levinger *Phys. Rev.*, vol. 90, p. 11, 1953.

[133] Z. Chen, W. R. Johnson, and L. Spruch *Phys. Rev. C*, vol. 40, p. 1376, 1989.

[134] E. L. Feinberg *J. Phys. (USSR)*, vol. 4, p. 423, 1941.

[135] R. L. Intemann *Phys. Rev. A*, vol. 28, p. 1288, 1983.

[136] I. S. Batkin, K. A. Bushahma, T. A. Churakova, and S. L. Demakov *J. Phys. G*, vol. 18, p. 1995, 1992.

[137] S. K. Nha, G. Schupp, and H. J. Nagy *Phys. Rev. C*, vol. 27, p. 1276, 1985.

[138] R. D. Scott *J. Phys. G*, vol. 9, p. 303, 1983.

[139] R. D. Scott *J. Phys. G*, vol. 6, p. 1427, 1980.

[140] G. Schupp and M. S. Freedman *Phys. Rev. C*, vol. 21, p. 348, 1980.

[141] E. L. Feinberg *Soviet J. of Nucl. Phys.*, vol. 1, p. 438, 1965.

[142] I. M. Band, M. B. Trzhaskovskaya, and M. A. Listengarten *At. Data and Nucl. Data Tables*, vol. 18, p. 433, 1976.

[143] E. Clementi and C. Roetti *At. Data and Nucl. Data Tables*, vol. 14, p. 177, 1974.

[144] K. R. Karim and L. Logan *Physica Scripta*, vol. 58, p. 574, 1998.

[145] G. Omar and Y. Hahn *Z. Phys. D*, vol. 25, p. 31, 1992.

[146] A. El-Shemi, Y. Lofty, and G. Zschornack *J. Phys. B*, vol. 30, p. 237, 1997.

[147] T. A. Carlson, W. E. Hunt, and M. O. . Krause *Phys. Rev.*, vol. 151, p. 41, 1966.

[148] E. Hollauer and M. A. C. Nascimento *Phys. Rev. A*, vol. 42, p. 6608, 1990.

[149] W. F. Chan, G. Cooper, X. Guo, and C. E. Brion *Phys. Rev. A*, vol. 45, p. 1420, 1992.

[150] W. F. Chan *et al. Phys. Rev. A*, vol. 46, p. 149, 1992.

[151] D. R. Maxson, J. S. Allen, and W. K. Jentschke *Phys. Rev.*, vol. 97, p. 109, 1955.

[152] C. G. Townsend *et al. Phys. Rev. A*, vol. 52, p. 1423, 1995.

[153] B. L. Peko and T. M. Stephen *Nucl. Instrum. and Meth. Phys. Res. B*, vol. 171, p. 597, 2000.

[154] M. Barat, J. C. Brenot, J. A. Fayeton, and Y. J. Picard *Rev. Sci. Instrum.*, vol. 71, p. 2050, 2000.

[155] T. M. Stephen and B. L. Peko *Rev. Sci. Instrum.*, vol. 71, p. 1355, 2000.

[156] A. M. Steane and C. J. Foot *Europhys. Lett.*, vol. 14, p. 231, 1991.

[157] C. D. Wallace *et al. J. Opt. Soc. Am. B*, vol. 11, p. 703, 1994.

[158] J. Dalibard and C. Cohen-Tannoudji *J. Opt. Soc. Am. B*, vol. 6, p. 2023, 1989.

[159] P. J. Ungar, D. S. Weiss, E. Riis, and S. Chu *J. Opt. Soc. Am. B*, vol. 6, p. 2058, 1989.

[160] P. M. Endt *Nucl. Phys. A*, vol. 521, p. 1, 1990.

[161] N. D. Scielzo, S. J. Freedman, B. K. Fujikawa, and P. A. Vetter. to be published.

[162] R. E. Kennerly *Rev. Sci. Instrum.*, vol. 48, p. 1682, 1976.

[163] R. W. W. van Resandt *J. Phys. E*, vol. 13, p. 1162, 1980.

[164] P. V. Schmidt *et al. Nucl. Instrum. and Meth. Phys. Res. A*, vol. 376, p. 139, 1996.

[165] M. M. Hindi *et al. Phys. Rev. A*, vol. 53, p. R3716, 1996.

[166] P. A. Voytas, J. E. Schewe, P. A. Quin, and L. W. Anderson *Nucl. Instr. and Meth. in Phys. Res. A*, vol. 374, p. 7, 1996.

[167] J. E. Schewe, P. A. Voytas, and P. A. Quin *Nucl. Instr. and Meth. in Phys. Res. A*, vol. 390, p. 274, 1997.

[168] K. L. Corwin, S. J. M. Kuppens, D. Cho, and C. E. Weiman *Phys. Rev. Lett.*, vol. 83, p. 1311, 1999.

[169] S. J. M. Kuppens *et al. Phys. Rev. A*, vol. 62, p. 013406, 2000.

[170] J. M. Robson *Phys. Rev.*, vol. 100, p. 933, 1955.

[171] R. Dobrozemsky *et al. Phys. Rev. D*, vol. 11, p. 510, 1975.

[172] B. M. Rustad and S. L. Ruby *Phys. Rev.*, vol. 89, p. 880, 1953.

[173] B. M. Rustad and S. L. Ruby *Phys. Rev.*, vol. 97, p. 991, 1955.

[174] C. A. Barnes *et al. Phys. Rev. Lett.*, vol. 1, p. 328, 1958.

[175] E. K. Warburton, D. E. Alburger, and D. H. Wilkinson *Phys. Rev. C*, vol. 26, p. 1186, 1982.

[176] W. P. Alford and D. R. Hamilton *Phys. Rev.*, vol. 95, p. 1351, 1954.

[177] M. L. Good and E. J. Lauer *Phys. Rev.*, vol. 105, p. 213, 1957.

[178] N. E. Booth *et al. Nucl. Phys.*, vol. 11, p. 341, 1959.

[179] E. T. H. Clifford *et al. Phys. Rev. Lett.*, vol. 50, p. 23, 1983.

[180] E. T. H. Clifford *et al. Nucl. Phys. A*, vol. 493, p. 293, 1989.

[181] D. Schardt and K. Riisager *Z. Phys. A*, vol. 345, p. 265, 1993.

[182] W. B. Herrmannsfeldt, D. R. Maxson, P. Stähelin, and J. S. Allen *Phys. Rev.*, p. 641, 1957.